UNIVERSIDADE ESTADUAL DE CAMPINAS
Faculdade de Engenharia Mecânica

Ana Carolina Azevedo Vasconcelos

An Impedance-Matrix Coupling Scheme for Arbitrarily-Shaped Structures Supported by Pile Groups

Método de Acoplamento de Matrizes de Impedância para Estruturas Estaqueadas

CAMPINAS
2019

Ana Carolina Azevedo Vasconcelos

An Impedance-Matrix Coupling Scheme for Arbitrarily-Shaped Structures Supported by Pile Groups

Método de Acoplamento de Matrizes de Impedância para Estruturas Estaqueadas

Dissertation presented to the School of Mechanical Engineering of the University of Campinas in partial fulfillment of the requirements for the degree of Master in Mechanical Engineering, in the area of Solid Mechanics and Mechanical Design.

Dissertação apresentada à Faculdade de Engenharia Mecânica da Universidade Estadual de Campinas como parte dos requisitos exigidos para a obtenção do título de Mestra em Engenharia Mecânica na área de Mecânica dos Sólidos e Projeto Mecânico

Orientador: Prof. Dr. Josué Labaki Silva

ESTE EXEMPLAR CORRESPONDE À VERSÃO FINAL DA DISSERTAÇÃO DEFENDIDA PELA ALUNA ANA CAROLINA AZEVEDO VASCONCELOS, E ORIENTADO PELO PROF. DR. JOSUÉ LABAKI SILVA.

.....
ASSINATURA DO ORIENTADOR

CAMPINAS
2019

Ficha catalográfica
Universidade Estadual de Campinas
Biblioteca da Área de Engenharia e Arquitetura
Luciana Pietrosanto Milla - CRB 8/8129

V441i

Vasconcelos, Ana Carolina Azevedo, 1995-
An impedance-matrix coupling scheme for arbitrarily-shaped structures supported by pile groups / Ana Carolina Azevedo Vasconcelos. – Campinas, SP : [s.n.], 2019.

Orientador: Josué Labaki Silva.
Dissertação (mestrado) – Universidade Estadual de Campinas, Faculdade de Engenharia Mecânica.

1. Interação solo-estrutura. 2. Fundações (Engenharia). 3. Dinâmica do solo. I. Silva, Josué Labaki. II. Universidade Estadual de Campinas. Faculdade de Engenharia Mecânica. III. Título.

Informações para Biblioteca Digital

Título em outro idioma: Método de acoplamento de matrizes de impedância para estruturas estaqueadas
Palavras-chave em inglês:
Soil-structure interaction
Foundations (Engineering)
Soil dynamics
Área de concentração: Mecânica dos Sólidos e Projeto Mecânico
Titulação: Mestra em Engenharia Mecânica
Banca examinadora:
Josué Labaki Silva [Orientador]
Pérsio Leister de Almeida Barros
William Martins Vicente
Data de defesa: 18-07-2019
Programa de Pós-Graduação: Engenharia Mecânica

Identificação e informações acadêmicas do(a) aluno(a)
- ORCID do autor: https://orcid.org/0000-0001-7624-8449
- Currículo Lattes do autor: http://lattes.cnpq.br/9951249526205379

UNIVERSIDADE ESTADUAL DE CAMPINAS

FACULDADE DE ENGENHARIA MECÂNICA

COMISSÃO DE PÓS-GRADUAÇÃO EM ENGENHARIA MECÂNICA

DEPARTAMENTO DE SISTEMAS INTEGRADOS

DISSERTAÇÃO DE MESTRADO ACADÊMICO

An Impedance-Matrix Coupling Scheme for Arbitrarily-Shaped Structures Supported by Pile Groups

Método de Acoplamento de Matrizes de Impedância para Estruturas Estaqueadas

Autora: Ana Carolina Azevedo Vasconcelos
Orientador: Prof. Dr. Josué Labaki Silva

A Banca Examinadora composta pelos membros abaixo aprovou esta Dissertação:

Prof. Dr. Josué Labaki Silva, President
Departamento de Sistemas Integrados, FEM, Unicamp

Prof. Dr. Pérsio Leister de Almeida Barros
Departamento de Geotecnia e Transportes, FEC, Unicamp

Prof. Dr. William Martins Vicente
Faculdade de Engenharia Agrícola, Unicamp

A Ata da defesa com as respectivas assinaturas dos membros encontra-se no processo de vida acadêmica do aluno.

Campinas, 18 de Julho de 2019.

Acknowledgments

I wish to thank my M.Sc. advisor, Prof. Josué Labaki, for his patience and enormous dedication during these two years. He is one of the few professors I've ever met who really cares about the development of his students.

I would like to thank Prof. Pérsio Barros from FEC/Unicamp and Prof. Amir Kaynia from Norwegian University of Science and Technology, through whom we have obtained the code that computes the piles model based on the impedance matrix method, which originated this work.

I am very grateful to my undergraduate research advisor, Prof. Simone Hoefel, for giving me the opportunity to study at Unicamp and to know new horizons. Also, my special thanks to the Computational Mechanics Lab (LaMeC) for building my knowledge foundation.

I would like to express my gratitude to my friends Iago, Emanuel, Andrés, Lucas, Esteban and Marcelo for contributing in this research and for providing special moments that I will never forget.

My deepest gratitude to my lovely family, especially my parents, my brother and my Aunt "Baby" who always cared about my education. Without them, I could have never lived these incredible moments.

This research could not be complete without the financial support of the National Council for Scientific and Technological Development - CNPq, through grant 137111/2017-7.

A man with nothing to FEAR is a man with nothing to LOVE.

The Joker

Ocean pulls me close
and whispers in my ear
the destiny I've chose
all becoming clear

Trent Reznor

The show must go on
I'll face it with a grin
I'm never giving in
On with the show

Queen

Resumo

Modelos numéricos de um grupo de estacas conectadas por estruturas flexíveis são componentes fundamentais para muitas análises de interação dinâmica solo-estrutura. Para a representação do grupo de estacas instalado no solo, muitos trabalhos consideram soluções discretas com o intuito de reduzir a complexidade do modelo. Já outros propõem formulações mais rigorosas que tratam a matriz de rigidez da camada de solo de forma exata, como é o caso do método da matriz de rigidez ou impedância (MMR). Embora este método resulte em um alto custo computacional, não há um limite para a espessura das camadas e para o valor da frequência, diferentemente das soluções discretas, nas quais certos critérios devem ser satisfeitos para garantir a convergência do resultado. Neste trabalho, o MMR é empregado para a análise dinâmica de grupos de estaca de grande escala instalados em um solo estratificado viscoelástico sujeito a cargas externas. Para modelar as estacas as equações de viga são utilizadas, enquanto que funções de Green para um meio estratificado são aplicadas para representar o campo de deslocamento devido às cargas associadas com as trações na interface estaca-solo, as quais são utilizadas na definição da matriz de flexibilidade do solo. Os termos desta matriz são integrais impróprias que requerem um esquema apropriado para avaliação numérica e, tipicamente, resultam em um alto custo computacional. Dois tipos de condições de acoplamento para grupos de estaca podem ser incorporados nesta matriz. Isto permite que as análises considerem a condição de acoplamento com menor custo computacional, sem perda da consistência física do modelo. Para a estrutura flexível suportada pelo grupo de estacas, um elemento finito linear e viscoelástico de 8 nós é considerado. O acoplamento entre os dois sistemas é obtido pelas equações de equilíbrio e de compatibilidade cinemática. Ferramentas computacionais modernas empregadas na presente implementação permitem não apenas que um grupo grande de estacas seja modelado, mas também um número quase arbitrário de camadas de solo e frequências de excitação, que ampliam consideravelmente as capacidades de modelagem desta formulação.

Palavras-chave: Interação solo-estrutura; Estruturas estaqueadas; Dinâmica do solo.

Abstract

Numerical models of pile groups connected by flexible structures are fundamental components of many dynamic soil-structure interaction analyses. For the representation of the pile group embedded in a soil, most works consider discrete solutions for both systems in order to reduce the complexity of the model. Others propose more rigorous formulations that treat the stiffness matrix of the layer exactly, such as the Stiffness or Impedance Matrix Method (SMM). Although this method resulting in a higher computational cost, there is no limitation to the thickness of the layers and to the frequency value, differently from discrete solutions, in which certain criteria must be satisfied in order to ensure the convergence of results. In this research, the SMM is used for dynamic analysis of large-scale pile groups embedded in a viscoelastic layered soil under external loading. Beam equations are used for modeling the piles, whereas Green's functions for layered media are applied to represent the displacement field due to the loads associated with pile-soil interface tractions, which is used to define the flexibility matrix of the soil. The terms of this matrix are improper integrals that require an appropriate scheme of numerical evaluation and, typically, resulting in a high computational cost. Two kinds of coupling conditions for embedded pile groups can be incorporated into this matrix, which enables analyses to consider the coupling condition with the lowest computational cost, without loss of physical consistency of the model. For the flexible structure supported by the pile group, a linear viscoelastic 8-noded hexahedral finite element is considered. The coupling between the two systems is obtained by kinematic compatibility and equilibrium equations. Modern computing tools incorporated into the present implementation enable not only massively large pile groups to be modeled, but a nearly arbitrary number of soil layers and excitation frequencies to be considered, which extend the modeling capabilities of the formulation considerably.

Keywords: Soil-structure interaction; Piled structures; Soil dynamics.

List of Figures

1.1 Stage of the construction of the Sirius facilities - large group of piles. 19
2.1 Pile group in a layered semi-infinite soil medium 25
2.2 Traction distribution on the j^{th} pile of the group 25
2.3 Forces on the single pile 28
2.4 Forces on the free field 29
2.5 Layered soil medium 36
2.6 Type of loads in pile-soil interface 46
2.7 Pile group in a multilayered media 51
2.8 Scheme of assemble of flexibility matrix of soil 53
2.9 Scheme of assemble of flexibility matrix of soil for a group of four piles 54
2.10 Integrand representation of $Re[u_{r1}^{u_1,f_1}]$ (Equation (2.106)). 55
2.11 Beam in steady-state lateral vibration. 56
2.12 Beam in steady-state axial vibration. 58
2.13 Fixed-end beam subjected to a lateral point load P. 59
2.14 Fixed-end beam subjected to a axial point load P. 60
2.15 Nodal forces at a segment i of a pile j. 63
2.16 Validation using a 2×2 pile grid. 65
2.17 Impedance of a 2×2 pile grid connected by a rigid cap. 65
3.1 8-noded hexahedral finite element in the (a) physical and (b) natural domain 66
3.2 Physical problem and free-body diagram of a fixed-end bar 67
3.3 Interface B of the fixed-end bar 68
3.4 Scheme of discretization of a piled structure 69
3.5 Interface and external loads and displacements 70
3.6 2×2 pile group connected by an elastic surface block 71
3.7 Stiffness and damping of the structure-foundation system for different elasticity moduli of the surface block 71
4.1 Pile grids used in this section, with (a) $N = 25$ and (b) $N = 36$ piles 72
4.2 Vertical displacement of pile (2) within a 5×5 pile grid. 73
4.3 Vertical displacements of pile (2) and pile (3) within a 6×6 pile grid. 73
4.4 Soil with continuously varying shear modulus versus discrete heterogeneous layers. 74
4.5 Convergence of pile response with numbers of layers. 75
4.6 Impulse response of pile tip. 76

4.7 Pile group configurations for (a) one, (b) two, and (c) four piles under vertical and horizontal loads 78
4.8 Real and imaginary part of u_z^* for a single pile. 78
4.9 Real and imaginary part of u_x^* and u_z^* for a group of two piles. 79
4.10 Real and imaginary part of u_x^* and u_z^* for a group of four piles. 79
4.11 Real and imaginary part of u_x^* for a single pile. 80
4.12 Real and imaginary part of u_x^* and u_z^* for a group of two piles. 80
4.13 Real and imaginary part of u_x^* and u_z^* for a group of four piles. 81
4.14 Horizontal response of second pile for different elastic moduli. 82
4.15 Vertical response of second pile for different elastic moduli. 83
4.16 Horizontal response from second pile for different mass densities. 84
4.17 Vertical response from second pile for different mass densities. 85
4.18 Horizontal response from second pile for different lenghts. 86
4.19 Vertical response from second pile for different lenghts. 87
4.20 Total computational cost to solve a single pile with M elements and N piles with $l = 20$ elements. 90
4.21 Pile group configurations for (a) one, (b) four, and (c) nine piles 90
4.22 Frontal plane of a structure submitted to a vertical load 91
4.23 Frontal plane of a supported structure submitted to a vertical load 92
4.24 Shear strain at the frontal face due to a vertical load for nondimensional frequency $a_0 = 0.5$ and $a_0 = 1.0$ 92
4.25 Volumetric strain at the frontal face due to a vertical load for nondimensional frequency $a_0 = 0.5$ and $a_0 = 1.0$ 93
4.26 Central plane of a structure submitted to a vertical load 93
4.27 Shear strain at the central face due to a vertical load for nondimensional frequency $a_0 = 0.5$ and $a_0 = 1.0$ 94
4.28 Volumetric strain at the central face due to a vertical load for nondimensional frequency $a_0 = 0.5$ and $a_0 = 1.0$ 94
4.29 Central plane of a supported structure submitted to a vertical load 95
4.30 Frontal plane of a structure submitted by a horizontal load 95
4.31 Frontal plane of a supported structure submitted by a horizontal load 95
4.32 Shear strain at the frontal face due to a horizontal load for nondimensional frequency $a_0 = 0.5$ and $a_0 = 1.0$ 96
4.33 Volumetric strain at the frontal face due to a horizontal load for nondimensional frequency $a_0 = 0.5$ and $a_0 = 1.0$ 96

4.34 Central plane of a structure submitted by a horizontal load 97
4.35 Shear strain at the central face due to a horizontal load for nondimensional frequency $a_0 = 0.5$ and $a_0 = 1.0$ 97
4.36 Volumetric strain at the central face due to a horizontal load for nondimensional frequency $a_0 = 0.5$ and $a_0 = 1.0$ 98
4.37 Central plane of a supported structure submitted by a horizontal load 98

List of Tables

4.1 Non-normalized vertical displacement of the pile head in single and double precision 88
4.2 Non-normalized vertical displacement of the pile tip in single and double precision 88
4.3 Computational cost of single pile with different numbers of elements M in seconds. 89
4.4 Computational cost of a pile group with N piles in seconds. 89
4.5 Computational cost of a pile group in seconds. 91

List of symbols and abbreviations

Latin Letters

A_p	-	Area of a pile section
A_j	-	Cross-sectional area of a general element j
a_0	-	Nondimensional frequency
$\mathbf{B}$	-	Vector of the shape functions derivatives
c_{xx}, c_{zz}	-	Dampings of the pile foundation associated with horizontal and vertical modes of vibration
C_p, C_s	-	Pressure and shear wave velocities of the soil
$\mathbf{D}$	-	Constitutive matrix of the element
d_p	-	Diameter of the pile
E_p, E_s, E_{st}	-	Moduli of elasticity of the piles, the soil, and the external structure
E_j	-	Modulus of elasticity of a general element j
EA	-	Axial rigidity of the beam
EI	-	Flexural rigidity of the beam
f_r, f_θ, f_z	-	Body forces in the soil medium in the r, θ and z directions
f_{rn}, $f_{\theta n}$, f_{zn}	-	Amplitude of Fourier series of f_r, f_θ and f_z
f_{1n}, f_{2n}, f_{3n}	-	Transformed loads
F_p	-	Dynamic flexibility matrix of piles under fixed-end conditions
F_s	-	Flexibility matrix of the soil
h	-	Height of a layer
h_b	-	Height of the external structure
H	-	Constant axial force in a pile
$\mathbf{J}$	-	Jacobian of transformation
$J_n(kr)$	-	n^{th} order Bessel function of the 1^{st} kind
k	-	Parameter of a Hankel transform
k_j	-	Stiffness of an element j
k_{xx}, k_{zz}	-	Stiffnesses of the pile foundation associated with horizontal and vertical modes of vibration

K_e	-	Impedance stiffness matrix of the pile group
$\mathbf{K}_e$	-	Stiffness matrix of the element
K_p	-	Dynamic stiffness matrix of the piles
$\mathbf{K}_G$	-	Global stiffness matrix
$\bar{\mathbf{K}}_G$	-	Dynamic global stiffness matrix
l	-	Number of cylindrical segments along the pile depth
l_b	-	Width of the external structure
l_p	-	Length of the pile
L_j	-	Length of a general element j
L	-	Length of the beam
m	-	Mass per unit length of the piles
M	-	Moment at a pile section
$\mathbf{M}_e$	-	Element mass matrix
$\mathbf{M}_G$	-	Global mass matrix
N	-	Number of piles in a group
$\mathbf{N}$	-	Vector of shape functions
P	-	Vector of forces of the pile-soil interface
P_e	-	Vector of forces for the ends of pile
r	-	Distance in the radial direction
R	-	Radius of the piles
s	-	Distance between adjacent piles
t	-	Time
$\mathbf{u}$	-	Displacement vectors of the element
u_x, u_y, u_z	-	Displacements of the pile-soil interface in the x, y and z directions
u_r, u_θ, u_z	-	Displacements in the soil in the x, θ and z directions
u_{rn}, $u_{\theta n}$, u_{zn}	-	Amplitudes of Fourier series of u_r, u_θ and u_z
u_{1n}, u_{2n}, u_{3n}	-	Transformed displacements
U^j	-	Vector of displacements of pile-soil interface
U_e	-	Vector of displacements for the ends of pile
V	-	Shear at a pile section
z	-	Distance in the vertical direction

Greek Letters

α	-	Parameter defined for the soil properties
β_p, β_s	-	Material damping of the pile and the soil
γ	-	Parameter defined for the soil properties (Eq. (2.38))
Δ	-	Dilatation (Eq. (2.18))
Δ_{total}	-	Total elapsed time to solve Eq.(2.11)
Δ_{F_s}	-	Time spent to fill matrix F_s
$\Delta_{Eq.(2.11)}$	-	Time spent to solve the linear system in Eq.(2.11)
ζ	-	Parameter defined for the piles (Eq. (2.121))
η	-	Parameter defined for the piles (Eq. (2.114))
θ	-	Angle between a vertical plane and the $x-z$ plane
λ, μ	-	Lamé's constants
ν_p, ν_s	-	Poison ratios of the pile and the soil
ξ	-	Parameter defined for the piles (Eq. (2.114))
ρ_p, ρ_s, ρ_{st}	-	Mass density of the pile, the soil and the external structure
σ_{rz}, $\sigma_{\theta z}$, σ_{zz}	-	Components of stress on a horizontal plane in cylindrical coordinates
σ_{rzn}, $\sigma_{\theta zn}$, σ_{zzn}	-	Amplitudes of Fourier series of σ_{rz}, $\sigma_{\theta z}$ and σ_{zz}
σ_{21n}, σ_{22n}, σ_{23n}	-	Transformed stresses
Ψ	-	Dynamic flexibility matrix of clamped-end piles for harmonic end displacements
ω	-	Frequency of vibration

Abbreviations

DSSI	-	Dynamic soil-structure interaction
FEM	-	Finite Element Method
LAPACK	-	Linear Algebra PACKage
MKL	-	Math Kernel Library
OpenMP	-	Open Multi-Processing
PARDISO	-	Parallel Direct Sparse Solver Interface
SMM	-	Stiffness Matrix Method
FFT	-	Fourier Fast Transform

Table of Contents

1 Introduction **19**

1.1 Literature review . . . 20
1.2 Motivation . . . 23
1.3 Objectives . . . 23
1.4 Organization of the text . . . 23

2 Impedance Matrix Method **25**

2.1 Flexibility matrix of soil medium $\mathbf{F_s}$ . . . 30
2.1.1 Green's functions for viscoelastic layered soil media . . . 30
2.1.2 Layer and halfspace stiffness matrices . . . 35
2.1.3 Displacements within a layer . . . 43
2.1.4 Integral representation . . . 45
2.1.5 Assembly of the flexibility matrix . . . 50
2.1.6 Evaluation of influence functions . . . 54
2.2 Dynamic stiffness matrix of the piles $\mathbf{K_p}$ . . . 56
2.3 Dynamic flexibility matrix of clamped-end piles $\mathbf{F_p}$ . . . 59
2.4 Dynamic flexibility matrix of clamped-end piles for harmonic end displacements $\mathbf{\Psi}$ 61
2.5 Implementation of dynamic piles code . . . 64
2.5.1 Validation . . . 64

3 Model of a surface structure **66**

3.1 Modeling of structure by FEM . . . 66
3.2 Coupling scheme . . . 67

4 Numerical results **72**

4.1 Number of piles . . . 72
4.2 Number of layers . . . 74
4.3 Reach in frequency . . . 75
4.4 Bonding condition . . . 76
4.4.1 Pile group configurations . . . 77
4.4.2 Pile parameters . . . 81
4.5 Numerical precision and computational cost . . . 88
4.6 Strain simulation of the flexible structure . . . 91

4.6.1 Strain field due to vertical loads 91
4.6.2 Strain field due to horizontal loads 95

5 Conclusions **99**

References **100**

1 Introduction

The new Brazilian Synchrotron Light Source, Sirius, recently become the largest and most complex Physics research laboratory in the country and one of the first 4th-generation Synchrotron Light Sources in the world. Sirius allows researchers to develop sophisticated analyses in many areas such as in agriculture, energy sector, health and many others. The principle of this source consists of accelerating particles to speeds approaching the speed of light and controlling their trajectories through magnetic field to produce Synchrotron Light, and to directed it to workstations for such analyses. In order for Sirius to operate properly, it is necessary that its foundation vibration should not exceed very strict limits. A typical approach to solve this vibration problem is to design the structure to be on top of a large group of piles. Figure 1.1 shows a stage in the construction of the Sirius Project, in which only a small fraction of its foundation can be seen, but which contains a large number of piles.

Figure 1.1: Stage of the construction of the Sirius facilities - large group of piles.

Piles are structures that are widely used in geotechnical projects for their ability to stiffen the soil locally, imbuing it with additional static load bearing capacity, and to transfer the loads from the superstructure to the ground. Usually, they are attached to a surface plate or a pile cap to increase the stiffness of the group. The response of the pile foundation embedded in soils is encompassed by the theory of dynamic soil-structure interaction (DSSI). This theory deals with two distinct issues

(Kausel, 2017). The first issue involves problems in which a dynamic external load is applied directly onto the structure, such as machines on elastic foundation, or buildings subjected to wind loads. The second one investigates the internal loads, that is, the dynamic excitation and sources applied within the soil mass.

These loads induce the propagation of waves into the media. For the case of an unbounded, homogeneous, isotropic, elastic fulll-space, only body waves in the form of pressure (P) and shear (S) waves are present, which propagate along arbitrary directions. For a half-space, however, the free boundary admits a nondispersive guided wave known as the Rayleigh wave, and may support body waves, which are the $SV - P$ and SH waves. The first one are vertically polarized S and P waves, which show particle motions in the vertical plane perpendicular to the surface and the direction of propagation. The second one are horizontally polarized shear waves involving particle motions in horizontal planes parallel to the free surface and perpendicular to the plane of propagation. The addition of one or more layers to the half-space complicates the analysis, since a set of interface waves will arise.

Many researchers have been investigating the interference of these waves in the response of the structure-foundation-soil system. Section 1.1 provides a review of some solutions of DSSI problems over the years.

1.1 Literature review

The theory of DSSI began in 1936 with a publication by Reissner (1936). In his work, the effect of time-harmonic uniform vertical load on circular disks applied onto elastic half-spaces was explored. A few years later in 1944, Reissner and Sagoci (1944) provided a rigorous solution for a dynamically loaded plate and exact formulas for rigid spheres, constituting one of the few problems that closed-form solutions are known.

Some decades later, Apsel and Luco (1976) used spheroidal coordinates to produce an exact solution for the torsional response of both prolate and oblate ellipsoidal foundations embedded in an elastic halfspace subjected to a harmonic torque about the vertical axis and to SH waves (horizontally polarized shear waves) propagating along arbitrary directions. Chadwick and Trowbridge (1967a) provided an exact solution of a rigid sphere in a full-space subjected to torsion and an

exact solution for a sphere subjected to lateral or vertical loads in a infinite elastic solid (Chadwick and Trowbridge, 1967b), both in the frequency and time domains. The solutions developed by these authors are important tools for validation of the results obtained with approximate numerical methods.

In decades of the 1950s and 1960s, a large quantity of publications dealing with dynamically loaded circular plates resting on half-spaces as well as on multilayered medium was observed. It is worth to highlight the papers developed by Quinlan (1954), Sung (1954), Bycroft (1956), Warburton (1957), Kobori and Thompson (1963), Awojobi and Grootenhuis (1965), and Gladwell (1968). All these works are based on some kind of approximation for the contact stress distributions and for evaluation of the integral equations. For instance, Bycroft's (1956) work evaluates the impedance of a rigid circular plate resting on a free surface of a semi-infinite elastic space or an elastic stratum for its four modes of vibration. In this work, he assumes that the stress distribution in the dynamic case can be approximated by the static distribution and obtains the plate's compliances by taking the 'weighted average' of the displacements over the loaded area, originally proposed by Arnold et al. (1955).

The first studies of pile groups were focused on the understanding of the static pile behavior, which resulted in many methods for pile foundation design, such as Poulos and Aust (1968), Poulos and Mattes (1971), Poulos (1971), Butterfiel and Banerjee (1971) and Banerjee (1978). These authors related the displacements to the corresponding forces in both the soil medium, through Midlin's fundamental solution, and in the piles, through pile differential equations, and coupled the two systems by using the direct equilibrium and kinematic compatibility at the soil-pile interface. Despite the fact that these solutions accounted for significant aspects of static pile group behavior, they were not capable of dealing with the dynamic aspects of the problem.

Extensive works have been developed to investigate the dynamic pile behavior. Some researches represented the soil as a Winkler foundation with distributed springs and dashpots that are constant or frequency dependent (Penzien, 1970; Matlock, 1970; Prakash and Chandrasekaran, 1973; Desai and Kuppusamy, 1980). The principal advantage of this model is the ability to represent non-linearity, inhomogeneity and hysteretic degradation of the soil surrounding the pile by changing the spring and dashpot constants. This approach, however, ignores the continuity between individual piles through the surrounding medium and cannot adequately describe the behavior of pile groups (Sen et al., 1985).

Some works have been implemented to overcome the limitations of Winkler model. Lysmer (1970) and Lysmer and Waas (1972) originally introduced the layer stiffness approach for the analysis of generalized Rayleigh waves in layered elastic media. Novak (1974) proposed an alternative approach to consider the soil-pile interaction in a relatively simple manner. In his model, the waves propagate only in the horizontal direction and there is no strain in the vertical direction. Nogami and Novák (1976) incorporated the vertical vibration in this model. Wolf and von Arx (1978) used a finite element scheme to obtain Green's functions for ring loads and then to investigate the horizontal as well as vertical dynamic stiffnesses of pile groups in a multilayered medium supported by a rigid bedrock. Waas and Hartmann (1981) used this methodology to analyse the behavior of pile groups in lateral vibration. Kausel and Roësset (1981) proposed the stiffness or impedance matrix method (SMM) which is based on a rigorous formulation for waves in layered media. This method encompasses layers of arbitrary thickness and high frequencies, differently than the semi-discrete Thin-Layer Method (Kausel and Peek, 1982). This semi-discrete method is based on a linearization of the displacement field in the direction of layering, in such a way that the transcendental Green's functions in the wavenumber domain become algebraic functions. However, this linearization is only possible when the wavelengths of plane shear waves are greater than approximately $4h$ (four times the layer thickness). Kaynia and Kausel (1991) proposed solutions for dynamic buried ring load (axial or lateral) and obtained the response of pile foundations to external and seismic excitation. In their numerical model, the piles are represented as elastic beams, the surrounding soil is represented by Green's functions for layered elastic halfspace, the impedance matrix of which is obtained by SMM, and the coupling between the two systems is obtained by direct equilibrium and kinematic compatibility at the soil-pile interface. More details about the impedance matrix method can be found in Kausel (2006, 2018).

Although Kaynia and Kausel's solution provides enough accuracy in modeling the dynamic response of pile groups with regards to their wave propagation response, their implementations are meant for practical application problems in which the number of piles is below a few dozen piles, the number of layers is up to thirty and the structure that connects the pile group is a rigid body. Moreover, the results of their solution have a single precision floating point value which is not sufficient for some applications. This last work is the basis for the development of the presented dissertation.

1.2 Motivation

This work is motivated by the investigation of pile group foundations connected to large flexible structures such as particle accelerators, concert halls, and nuclear powerplants. Modelling and understanding the dynamic response of such systems and their energy dissipation and absorption through the soil is fundamental for their remarkably strict vibration requirements to be complied with.

1.3 Objectives

The main objective of this dissertation is to propose a coupling scheme between a pile group modeled by the Impedance Matrix Method (SMM) and a flexible structure obtained by the Finite Element Method (FEM). The present implementation intends to extend Kaynia and Kausel's pile group model for an arbitrary number of soil layers, piles and excitation frequencies. The list below contains the specific objectives of this research.

- Implementation of the Impedance Matrix Method using Fortran 90;
- Study and implementation of techniques for reduction of the computational cost of the code;
- Implementation of the flexible structure using Finite Element Method;
- Implementation of the coupling between a pile group and a flexible structure;
- Analysis of the response of structures supported by pile groups.

1.4 Organization of the text

This dissertation is organized as follows.

In Chapter 2, the SMM is detailed as reported by Kaynia and Kausel (1991). The dynamic stiffness matrix of the pile group submitted to external loads is obtained. In this model, the loads

at pile-soil interface are defined as lateral and vertical forces. Finally, details about the present implementation are described. A literature example is used for its validation.

Chapter 3 presents the model for the structure supported by the pile group. The chapter begins with a brief review of the FEM and a description of the element used to model such structure. The coupling scheme for the case of piled structures is proposed. The present scheme is validated with a literature example.

In Chapter 4, the numerical results for different pile groups obtained by the present implementation are compared with results from the literature. Original numerical results for various number of layers, piles and frequencies are shown. Lastly, strain-deformation simulations of the flexible structure are obtained in order to verify the physical consistency of the proposed coupling scheme.

2 Impedance Matrix Method

The stiffness or impedance matrix method is a tool for analysis of wave propagation problems in elastic media. In this chapter, the formulation proposed by Kaynia (1982) is described in detail.

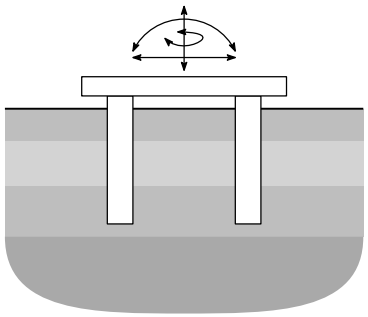

Figure 2.1: Pile group in a layered semi-infinite soil medium

Consider the pile group shown in Fig. 2.1. The piles consist of linear elastic beams connected to a rigid cap and embedded in a layered viscoelastic three-dimensional medium resting on a half-space or a rigid bedrock. The group is submitted to harmonically-vibrating external loads, which can be represented by vertical and horizontal forces, and rocking and torsional moments. It is assumed that there is no loss of bondage between the piles and the soil. The traction distribution in pile-soil interface can be resolved into frictional and lateral components (Fig. 2.2).

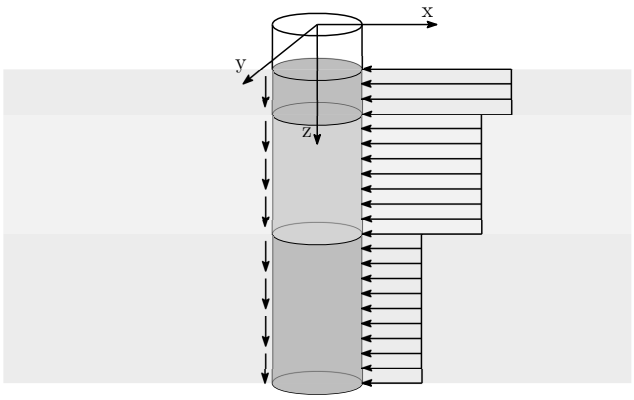

Figure 2.2: Traction distribution on the j^{th} pile of the group

This interface is discretized into l arbitrary cylindrical segments along the pile corresponding to the soil layers and one circular segment ($l + 1$) at pile-tip. The pile head and the center of

each segment define then $(l+2)$ nodes. The actual traction distribution is replaced by a piecewise constant distributions for each segment.

From the equilibrium of pile j under the pile-soil interface forces, the vector of resultant of these forces P^j can be defined as

$$P^j = \begin{bmatrix} p^j_{1x} & p^j_{1y} & p^j_{1z} & \cdots & p^j_{(l+1)x} & p^j_{(l+1)y} & p^j_{(l+1)z} \end{bmatrix}^T \tag{2.1}$$

and the vector of displacements U^j of nodes 1 through $(l+1)$

$$U^j = \begin{bmatrix} u^j_{1x} & u^j_{1y} & u^j_{1z} & \cdots & u^j_{(l+1)x} & u^j_{(l+1)y} & u^j_{(l+1)z} \end{bmatrix}^T \tag{2.2}$$

Kaynia defined the vector U^j as the superposition of the displacements caused by the translation and rotation of both ends of a pile without loads, and the displacements caused by tractions P^j in a pile with both ends fixed. Then,

$$U^j = \Psi^j U^j_e - F^j_p P^j \tag{2.3}$$

in which U^j_e is the vector of displacements for the ends of pile j, represented by

$$U^j_e = \begin{bmatrix} u^j_{0x} & \phi^j_{0x} & u^j_{0y} & \phi^j_{0y} & u^j_{0z} & u^j_{(l+1)x} & \phi^j_{(l+1)x} & u^j_{(l+1)y} & \phi^j_{(l+1)y} & u^j_{(l+1)z} \end{bmatrix}^T, \tag{2.4}$$

Ψ^j is a $3(l+1) \times 10$ shape matrix defining displacements of the center of segments due to end displacements of the pile when P^j are not present, and F^j_p is the flexibility matrix of pile j under fixed-end conditions, associated with nodes 1 through $(l+1)$.

Assuming that the dynamic stiffness matrix of pile j is denoted by K^j_p and the vector of external loads (forces and moments) at the two ends of this pile by P^j_e, such that

$$P^j_e = \begin{bmatrix} R^j_{0x} & M^j_{0x} & R^j_{0y} & M^j_{0y} & R^j_{0z} & R^j_{(l+1)x} & M^j_{(l+1)x} & R^j_{(l+1)y} & M^j_{(l+1)y} & R^j_{(l+1)z} \end{bmatrix}^T \tag{2.5}$$

then the following expression can be written

$$P^j_e = K^j_p U^j_e + \Psi^{jT} P^j \tag{2.6}$$

in which the first term of Eq. (2.6) corresponds to pile-end forces due to pile-end displacements when there are no loads on the pile, and the second term corresponds to pile-end forces due to loads on the pile when the ends are fixed.

For the N piles in the group, the global load and displacement vectors are defined as

$$P = \begin{bmatrix} P^1 \\ P^2 \\ \vdots \\ P^N \end{bmatrix}; \quad U = \begin{bmatrix} U^1 \\ U^2 \\ \vdots \\ U^N \end{bmatrix}; \quad P_e = \begin{bmatrix} P_e^1 \\ P_e^2 \\ \vdots \\ P_e^N \end{bmatrix}; \quad U_e = \begin{bmatrix} U_e^1 \\ U_e^2 \\ \vdots \\ U_e^N \end{bmatrix}; \tag{2.7}$$

and the matrices

$$K_p = \begin{bmatrix} K_p^1 & & & \\ & K_p^2 & & \\ & & \ddots & \\ & & & K_p^N \end{bmatrix}; \quad F_p = \begin{bmatrix} F_p^1 & & & \\ & F_p^2 & & \\ & & \ddots & \\ & & & F_p^N \end{bmatrix}; \quad \Psi = \begin{bmatrix} \Psi^1 & & & \\ & \Psi^2 & & \\ & & \ddots & \\ & & & \Psi^N \end{bmatrix}; \tag{2.8}$$

Then for the ensemble of piles in the group, the Eqs. (2.3) and (2.6) can be written by

$$\begin{cases} U = \Psi U_e - F_p P \\ P_e = K_p U_e + \Psi^T P \end{cases} \tag{2.9}$$

From the equilibrium of the soil mass under forces P, the relation between the piecewise-constant segmental loads and the average displacements along the segments is given by

$$U = F_s P \tag{2.10}$$

where F_s is the flexibility matrix of the soil medium. Substituting Eq. (2.10) into Eq. (2.9), the following expression is obtained

$$P_e = \left[K_p + \Psi^T \left(F_s + F_p\right)^{-1} \Psi\right] U_e = K_e U_e \tag{2.11}$$

Matrix K_e is the impedance or dynamic stiffness matrix of the pile group ($10N \times 10N$) which relates the five components of forces at the piles ends to their corresponding displacements. This

relation is only applicable in a group of unrestrained piles. In order to obtain the dynamic stiffness matrix of a rigid foundation (pile group along with pile cap) to which the piles are connected, it is necessary to enforce equilibrium and kinematic compatibility at the pile head-pile cap interface.

The matrix F_s corresponds to the flexibility of a soil mass with N cavities, which include a significant computational effort into the evaluation of such matrix. In order to overcome this effort, the cavities are filled with the soil and the appropriate modifications are imposed on the formulation.

Consider a single pile embedded in a semi-infinite soil medium as shown in Fig. 2.3.

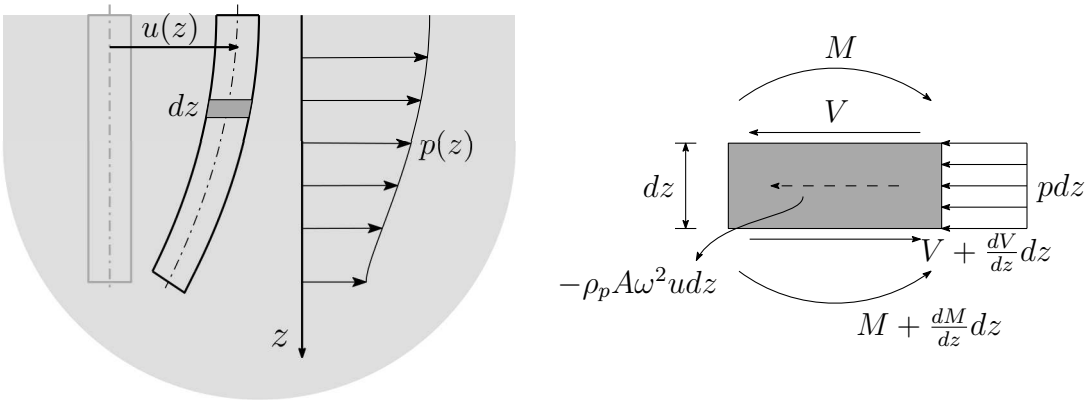

Figure 2.3: Forces on the single pile

The lateral soil pressure and lateral pile displacement are defined as $p(z)$ and $u(z)$, respectively. The equilibrium equation for a pile element is given by

$$\frac{dV}{dz} + \rho_p A \omega^2 u = p \tag{2.12}$$

in which V and A are the shear and area of the pile section, respectively, and ρ_p is the mass density of the pile.

In next analysis, consider the same soil medium, but without the pile, and the resulting cavity is filled with soil such that the original uniform soil mass is obtained (free field). The dashed line in Fig. 2.4 represents the column of soil added at the cavity. $f(z)$ defines a force distribution along the depth of the soil column, which supposes to cause approximately the same displacement $u(z)$ at its centerline.

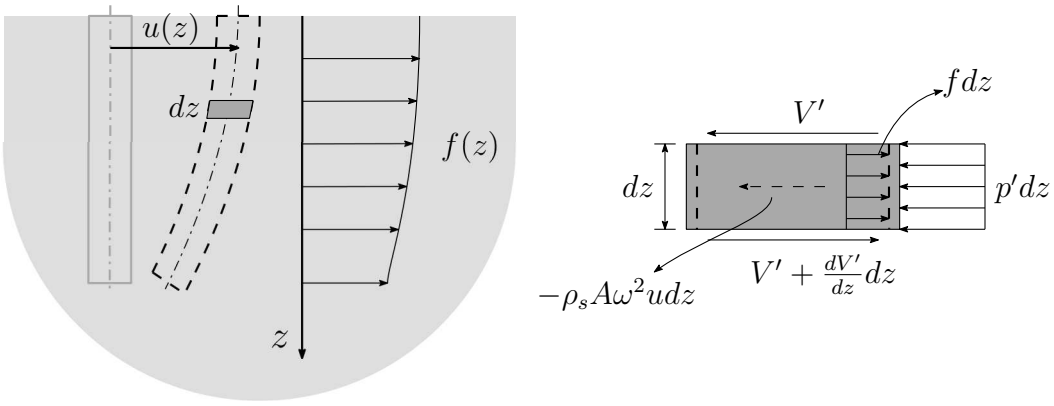

Figure 2.4: Forces on the free field

The equilibrium equation for a soil differential element is given by

$$\frac{dV'}{dz} + \rho_s A\omega^2 u + f = p' \tag{2.13}$$

where p' is the lateral force on this element.

If p' is considered equal to p, Eq. (2.13) can be written as

$$\frac{dV'}{dz} + \rho_s A\omega^2 u + f = p \tag{2.14}$$

The displacement $u(z)$ due to a distributed force $p(z)$ in the soil with the cavity is obtained when a distributed force $f(z)$ is applied into the uniform soil medium. Thus, $f(z)$ is given by

$$f = p - \rho_s A\omega^2 u - \frac{dV'}{dz} \tag{2.15}$$

The equilibrium of the differential pile element can be expressed in terms of f by introducing Eq. (2.14) into Eq. (2.12), that is

$$\frac{d}{dz}(V - V') + (\rho_p - \rho_s)A\omega^2 u = f \tag{2.16}$$

The differential equation (2.16) can be interpreted as a beam with a mass density $(\rho_p - \rho_s)$ and a modulus of elasticity $(E_p - E_s)$ excited by a distributed force $f(z)$.

This approximate scheme suggests that if forces P in Eqs. (2.9) and (2.10) are replaced by the vectorial equivalent of the distributed forces f, then the flexibility matrix of the soil F_s should be taken as that corresponding to a free field soil and the matrices K_p, F_p and Ψ represent piles with reduced mass density and elasticity modulus.

Sections 2.1 to 2.4 describe in detail each of the terms involved in Eq. (2.11).

2.1 Flexibility matrix of soil medium $\mathbf{F_s}$

This section evaluates the dynamic flexibility matrix F_s for the soil medium. This matrix relates piecewise uniform loads distributed over vertical cylindrical surfaces or horizontal circular surfaces and a representative displacement of these regions. Green's functions are used to define the displacement fields due to these loads and are computed by solving the wave equations through Fourier and Hankel transforms.

2.1.1 Green's functions for viscoelastic layered soil media

Consider an elastic, three-dimensional, isotropic full-space, with cylindrical coordinate systems (r,θ,z) aligned in such a way that the z axis is orthogonal to plane of isotropy of the medium. The displacements in the radial, tangential and vertical directions are u_r, u_θ and u_z, and the associated external loads per unit volume are f_r, f_θ and f_z. The equations of motion of this elastic body in cylindrical coordinates are

$$\begin{cases} (\lambda+2\mu)\dfrac{\partial\Delta}{\partial r} - \dfrac{2\mu}{r}\dfrac{\partial\omega_z}{\partial\theta} + 2\mu\dfrac{\partial\omega_\theta}{\partial z} + \omega^2\rho u_r + f_r = 0 \\ (\lambda+2\mu)\dfrac{1}{r}\dfrac{\partial\Delta}{\partial\theta} - 2\mu\dfrac{\partial\omega_r}{\partial z} + 2\mu\dfrac{\partial\omega_z}{\partial r} + \omega^2\rho u_\theta + f_\theta = 0 \\ (\lambda+2\mu)\dfrac{\partial\Delta}{\partial z} - \dfrac{2\mu}{r}\dfrac{\partial}{\partial r}(r\omega_\theta) + \dfrac{2\mu}{r}\dfrac{\partial\omega_r}{\partial\theta} + \omega^2\rho u_z + f_z = 0 \end{cases} \tag{2.17}$$

where λ and μ are Lamé's constant, ρ is the mass density and ω is the frequency of steady-state vibration. The dilatation Δ and the rotations ω_r, ω_θ and ω_z are expressed by

$$\Delta = \frac{1}{r}\frac{\partial}{\partial r}(ru_r) + \frac{1}{r}\frac{\partial u_\theta}{\partial \theta} + \frac{\partial u_z}{\partial z} \tag{2.18}$$

$$\begin{aligned} \omega_r &= \frac{1}{2}\left(\frac{1}{r}\frac{\partial u_z}{\partial \theta} - \frac{\partial u_\theta}{\partial z}\right) \\ \omega_\theta &= \frac{1}{2}\left(\frac{\partial u_r}{\partial z} - \frac{\partial u_z}{\partial r}\right) \\ \omega_z &= \frac{1}{2r}\left(\frac{\partial}{\partial r}(ru_\theta) - \frac{\partial u_r}{\partial \theta}\right) \end{aligned} \tag{2.19}$$

In order to include the viscoelastic effect of hysteretic type into the soil, one can replace λ and μ in Eq. (2.17) by the complex Lamé's moduli

$$\begin{cases} \lambda^c = \lambda(1 + 2\beta i) \\ \mu^c = \mu(1 + 2\beta i) \end{cases} \tag{2.20}$$

where β is the fraction of critical damping (Christensen, 2012).

For the solution of Eq. (2.17), a separation of variables is used by expanding displacements and body forces which are symmetric with respect to $\theta = 0$ in a Fourier series in tangential direction (Muki, 1960), that is

$$\begin{cases} u_r(r,\theta,z) = \sum_{n=0}^{\infty} u_{rn}(r,z)\ \cos(n\theta) \\ u_\theta(r,\theta,z) = \sum_{n=0}^{\infty} u_{\theta n}(r,z)\ \sin(n\theta) \\ u_z(r,\theta,z) = \sum_{n=0}^{\infty} u_{zn}(r,z)\ \cos(n\theta) \\ f_r(r,\theta,z) = \sum_{n=0}^{\infty} f_{rn}(r,z)\ \cos(n\theta) \\ f_\theta(r,\theta,z) = \sum_{n=0}^{\infty} f_{\theta n}(r,z)\ \sin(n\theta) \\ f_z(r,\theta,z) = \sum_{n=0}^{\infty} f_{zn}(r,z)\ \cos(n\theta) \end{cases} \tag{2.21}$$

Substituting these expansions and Eqs. (2.18) and (2.19) into Eq. (2.17) gives

$$\sum_{n=0}^{\infty}\{\ \mu\left[\frac{\partial^2 u_{rn}}{\partial r^2}+\frac{1}{r}\frac{\partial u_{rn}}{\partial r}-\frac{n^2+1}{r^2}u_{rn}+\frac{\partial^2 u_{rn}}{\partial z^2}\right]+(\lambda+\mu)\frac{\partial \Delta_n}{\partial r} \\ -2\mu\frac{n}{r^2}u_{\theta n}+\omega^2\rho u_{rn}+f_{rn}\ \}\cos(n\theta)=0 \tag{2.22}$$

$$\sum_{n=0}^{\infty}\{\ \mu\left[\frac{\partial^2 u_{\theta n}}{\partial r^2}+\frac{1}{r}\frac{\partial u_{\theta n}}{\partial r}-\frac{n^2+1}{r^2}u_{\theta n}+\frac{\partial^2 u_{\theta n}}{\partial z^2}\right]-(\lambda+\mu)\frac{n}{r}\Delta_n \\ -2\mu\frac{n}{r^2}u_{rn}+\omega^2\rho u_{\theta n}+f_{\theta n}\ \}\sin(n\theta)=0 \tag{2.23}$$

$$\sum_{n=0}^{\infty}\{\ \mu\left[\frac{\partial^2 u_{zn}}{\partial r^2}+\frac{1}{r}\frac{\partial u_{zn}}{\partial r}-\frac{n^2}{r^2}u_{zn}+\frac{\partial^2 u_{zn}}{\partial z^2}\right]+(\lambda+\mu)\frac{\partial \Delta_n}{\partial z} \\ +\omega^2\rho u_{zn}+f_{zn}\ \}\cos(n\theta)=0 \tag{2.24}$$

where

$$\Delta_n=\frac{1}{r}\frac{\partial}{\partial r}(ru_{rn})+\frac{n}{r}u_{\theta n}+\frac{\partial u_{zn}}{\partial z} \tag{2.25}$$

Equations (2.22), (2.23) and (2.24) are satisfied when the terms in braces are identically zero. If the two equations resulting from Eqs. (2.22) and (2.23) are combined, then the following three conditions are obtained, to be satisfied for any value of n,

$$\mu\left[\frac{\partial^2}{\partial r^2}(u_{rn}+u_{\theta n})+\frac{1}{r}\frac{\partial}{\partial r}(u_{rn}+u_{\theta n})-\frac{(n+1)^2}{r^2}(u_{rn}+u_{\theta n})+\frac{\partial^2}{\partial z^2}(u_{rn}+u_{\theta n})\right] \\ +(\lambda+\mu)\left(\frac{\partial \Delta_n}{\partial r}-\frac{n}{r}\Delta_n\right)+\omega^2\rho(u_{rn}+u_{\theta n})+(f_{rn}+f_{\theta n})=0 \tag{2.26}$$

$$\mu\left[\frac{\partial^2}{\partial r^2}(u_{rn}-u_{\theta n})+\frac{1}{r}\frac{\partial}{\partial r}(u_{rn}-u_{\theta n})-\frac{(n-1)^2}{r^2}(u_{rn}-u_{\theta n})+\frac{\partial^2}{\partial z^2}(u_{rn}-u_{\theta n})\right] \\ +(\lambda+\mu)\left[\frac{\partial \Delta_n}{\partial r}+\frac{n}{r}\Delta_n\right]+\omega^2\rho(u_{rn}-u_{\theta n})+(f_{rn}-f_{\theta n})=0 \tag{2.27}$$

$$\mu\left[\frac{\partial^2 u_{zn}}{\partial r^2}+\frac{1}{r}\frac{\partial u_{zn}}{\partial r}-\frac{n^2}{r^2}u_{zn}+\frac{\partial^2 u_{zn}}{\partial z^2}\right]+(\lambda+\mu)\frac{\partial \Delta_n}{\partial z}+\omega^2\rho u_{zn}+f_{zn}=0 \tag{2.28}$$

Applying the following Hankel Transforms

$$\begin{cases} u_{1n}(k,z) + u_{3n}(k,z) = \int_0^\infty (u_{rn} + u_{\theta n}) J_{n+1}(kr)\, r dr \\ -u_{1n}(k,z) + u_{3n}(k,z) = \int_0^\infty (u_{rn} - u_{\theta n}) J_{n-1}(kr)\, r dr \\ u_{2n}(k,z) = \int_0^\infty u_{zn} J_n(kr)\, r dr \\ f_{1n}(k,z) + f_{3n}(k,z) = \int_0^\infty (f_{rn} + f_{\theta n}) J_{n+1}(kr)\, r dr \\ -f_{1n}(k,z) + f_{3n}(k,z) = \int_0^\infty (f_{rn} - f_{\theta n}) J_{n-1}(kr)\, r dr \\ f_{2n}(k,z) = \int_0^\infty f_{zn} J_n(kr)\, r dr \end{cases} \tag{2.29}$$

where $J_n(kr)$ is the n^{th} order Bessel function of the 1^{st} kind, and the following identities

$$\int_0^\infty \left[\frac{\partial^2}{\partial r^2} + \frac{1}{r}\frac{\partial}{\partial r} - \frac{m^2}{r^2} + \frac{\partial^2}{\partial z^2}\right] \phi J_m(kr) r dr = \left(\frac{\partial^2}{\partial z^2} - k^2\right) \int_0^\infty \phi J_m(kr) r dr \tag{2.30}$$

$$\int_0^\infty \left(\frac{\partial}{\partial r} - \frac{m}{r}\right) \phi J_{m+1}(kr) r dr = -k \int_0^\infty \phi J_m(kr) r dr \tag{2.31}$$

$$\int_0^\infty \left(\frac{\partial}{\partial r} + \frac{m}{r}\right) \phi J_{m-1}(kr) r dr = k \int_0^\infty \phi J_m(kr) r dr \tag{2.32}$$

into Eqs. (2.26), (2.27) and (2.28) leads to

$$\begin{cases} \mu\left[\frac{\partial^2}{\partial z^2} - k^2 + \omega^2 \frac{\rho}{\mu}\right](u_{1n} + u_{3n}) + (\lambda+\mu)(-k\Delta'_n) + f_{1n} + f_{3n} = 0 \\ \mu\left[\frac{\partial^2}{\partial z^2} - k^2 + \omega^2 \frac{\rho}{\mu}\right](-u_{1n} + u_{3n}) + (\lambda+\mu)(k\Delta'_n) - f_{1n} + f_{3n} = 0 \\ \mu\left[\frac{\partial^2}{\partial z^2} - k^2 + \omega^2 \frac{\rho}{\mu}\right] u_{2n} + (\lambda+\mu)\frac{\partial}{\partial z}\Delta'_n + f_{2n} = 0 \end{cases} \tag{2.33}$$

where $\Delta'_n = \int_0^\infty \Delta_n J_n(kr) r dr$ is the n^{th} order Hankel Transform of Δ_n. Using the following property of Bessel functions

$$\frac{n}{r} J_n(kr) = \pm \frac{\partial}{\partial r} J_n(kr) + k J_{n\pm1}(kr) \tag{2.34}$$

and the relations (2.31) and (2.32), this term also can be defined as

$$\Delta'_n = ku_{1n} + \frac{\partial}{\partial z}u_{2n} \tag{2.35}$$

Substituting Equation (2.35) into Eqs. (2.33) and then combining the two first equations of Eq. (2.33), the following ordinary differential equations are obtained

$$\begin{cases} \left[\mu\dfrac{\partial^2}{\partial z^2} - k^2(\lambda+2\mu) + \rho\omega^2\right]u_{1n} - (\lambda+\mu)k\dfrac{\partial}{\partial z}u_{2n} + f_{1n} = 0 & \text{(2.36a)} \\ (\lambda+\mu)k\dfrac{\partial}{\partial z}u_{1n} + \left[(\lambda+2\mu)\dfrac{\partial^2}{\partial z^2} - \mu k^2 + \rho\omega^2\right]u_{2n} + f_{2n} = 0 & \text{(2.36b)} \\ (\mu\dfrac{\partial^2}{\partial z^2} - \mu k^2 + \rho\omega^2)u_{3n} + f_{3n} = 0 & \text{(2.36c)} \end{cases}$$

Equations $(2.36a)$ and $(2.36b)$ are coupled and define a system of two ordinary linear differential equations for u_{1n} and u_{2n}, whereas Eq. $(2.36c)$ is uncoupled from u_{1n} and u_{2n}. Then, u_{3n} can be obtained by solving Eq. $(2.36c)$. In the next steps, the following parameters will be introduced:

$$\alpha = \sqrt{k^2 - \frac{\rho\omega^2}{\lambda+2\mu}} = \sqrt{k^2 - \left(\frac{\omega}{C_p}\right)^2} \tag{2.37}$$

$$\gamma = \sqrt{k^2 - \frac{\rho\omega^2}{\mu}} = \sqrt{k^2 - \left(\frac{\omega}{C_s}\right)^2} \tag{2.38}$$

where C_s and C_p are the velocities of shear and pressure waves, respectively. Introducing these parameters into Eq. (2.36) gives

$$\begin{cases} (\lambda+2\mu)\left[\dfrac{\mu}{\lambda+2\mu}\dfrac{\partial^2}{\partial z^2} - \alpha^2\right]u_{1n} - (\lambda+\mu)k\dfrac{\partial}{\partial z}u_{2n} + f_{1n} = 0 & \text{(2.39a)} \\ (\lambda+\mu)k\dfrac{\partial}{\partial z}u_{1n} + \mu\left[\dfrac{\lambda+2\mu}{\mu}\dfrac{\partial^2}{\partial z} - \gamma^2\right]u_{2n} + f_{2n} = 0 & \text{(2.39b)} \end{cases}$$

$$\mu\left(\frac{\partial^2}{\partial z^2} - \gamma^2\right)u_{3n} + f_{3n} = 0 \tag{2.40}$$

In order to obtain the homogeneous solution of Eq. (2.39), it is assumed that $u_{1n} = Ae^{\eta z}$ and

$u_{2n} = Be^{\eta z}$ in Eq. (2.39). The resulting system of algebraic equations for η and A/B yields four sets of solutions, which are used to define the following homogeneous solutions for u_{1n} and u_{2n}

$$\begin{cases} u_{1n}^H(k,z) = -k\,C_{1n}\,e^{-\alpha z} + \gamma\,C_{2n}\,e^{-\gamma z} - C_{3n}\,e^{\alpha z} + \gamma\,C_{4n}\,e^{\gamma z} \\ u_{2n}^H(k,z) = -\alpha\,C_{1n}\,e^{-\alpha z} + k\,C_{2n}\,e^{-\gamma z} + \alpha\,C_{3n}\,e^{\alpha z} - k\,C_{4n}\,e^{\gamma z} \end{cases} \tag{2.41}$$

where $C_{1n}(k)$, $C_{2n}(k)$, $C_{3n}(k)$ and $C_{4n}(k)$ are unknown constants. In order to obtain a particular solution, a method of variation of parameters can be used. However, the loadings involved in this problem, f_{1n} and f_{2n} are independent of z. Therefore, particular solutions can be obtained by the inspection method. A set of solutions for u_{1n} and u_{2n} are

$$\begin{cases} u_{1n}^P = \dfrac{1}{\alpha^2(\lambda+2\mu)}\,f_{1n} \\ u_{2n}^P = \dfrac{1}{\gamma^2\mu}\,f_{2n} \end{cases} \tag{2.42}$$

Then, the solutions of Eq. (2.39) are

$$\begin{Bmatrix} u_{1n}(k,z) \\ u_{2n}(k,z) \end{Bmatrix} = \begin{bmatrix} -k & \gamma & -k & \gamma \\ -\alpha & k & \alpha & -k \end{bmatrix} \begin{Bmatrix} C_{1n}\,e^{-\alpha z} \\ C_{2n}\,e^{-\gamma z} \\ C_{3n}\,e^{\alpha z} \\ C_{4n}\,e^{\gamma z} \end{Bmatrix} + \begin{Bmatrix} f_{1n}/\alpha^2(\gamma+2\mu) \\ f_{2n}/\gamma^2\mu \end{Bmatrix} \tag{2.43}$$

Applying a similar scheme to Eq. (2.39) gives the solution of this equation

$$u_{3n}(k,z) = \begin{bmatrix} 1 & 1 \end{bmatrix} \begin{Bmatrix} C_{5n}\,e^{-\gamma z} \\ C_{6n}\,e^{\gamma z} \end{Bmatrix} + \frac{1}{\gamma^2\mu} f_{3n} \tag{2.44}$$

2.1.2 Layer and halfspace stiffness matrices

Consider the layered soil medium shown in Fig. 2.5. The soil consists of l layers resting on a halfspace. Fig. 2.5b shows the j^{th} layer confined between two planes (A and B) and Fig. 2.5c shows the halfspace bounded by the plane C.

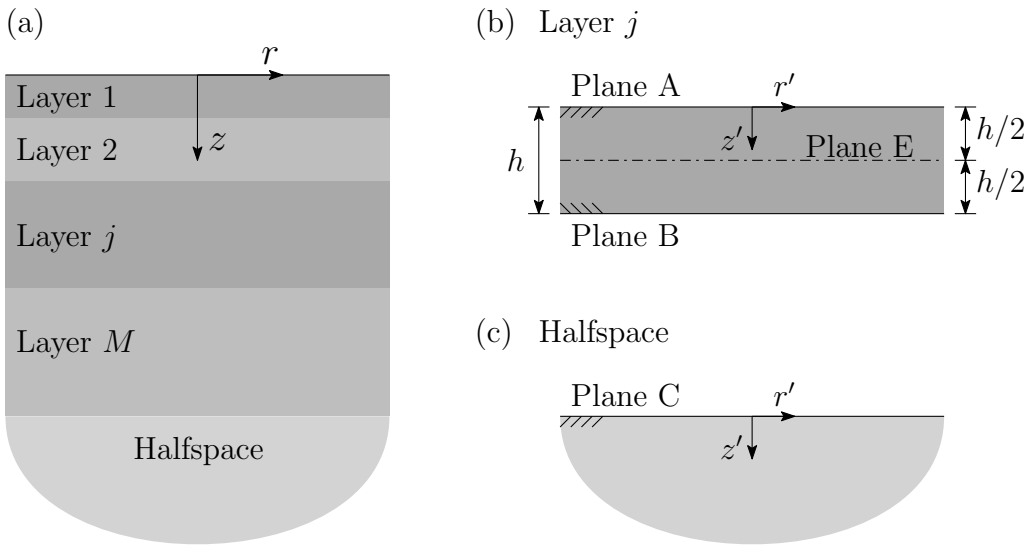

Figure 2.5: Layered soil medium

In order to obtain the stiffness matrices of the layer and halfspace, it is necessary to relate the transformed displacements in Eqs. (2.43) and (2.44) with the associated transformed stresses. Then, the next step in the solution procedure is to derive expressions for these stresses. The three components of stress on a plane perpendicular to the z-axis in cylindrical coordinates are

$$\begin{cases} \sigma_{rz} = \mu \left(\dfrac{\partial u_z}{\partial r} + \dfrac{\partial u_r}{\partial z} \right) \\ \sigma_{\theta z} = \mu \left(\dfrac{\partial u_\theta}{\partial z} + \dfrac{1}{r} \dfrac{\partial u_z}{\partial \theta} \right) \\ \sigma_{zz} = 2\mu \dfrac{\partial u_z}{\partial z} + \lambda \Delta \end{cases} \tag{2.45}$$

Using the Fourier expansion of u_r, u_θ and u_z (Eq. (2.21)) in the above equations, it is obtained

$$\begin{cases} \sigma_{rz} = \sum_{n=0}^{\infty} \sigma_{rzn} \cos(n\theta) \\ \sigma_{\theta z} = \sum_{n=0}^{\infty} \sigma_{\theta zn} \sin(n\theta) \\ \sigma_{zz} = \sum_{n=0}^{\infty} \sigma_{zzn} \cos(n\theta) \end{cases} \tag{2.46}$$

where σ_{rzn}, $\sigma_{\theta zn}$ and σ_{zzn} are given by

$$\begin{cases} \sigma_{rzn} = \mu\left(\dfrac{\partial u_{zn}}{\partial r} + \dfrac{\partial u_{rn}}{\partial z}\right) & \text{(2.47a)} \\ \sigma_{\theta zn} = \mu\left(\dfrac{\partial u_{\theta n}}{\partial z} - \dfrac{n}{r}u_{zn}\right) & \text{(2.47b)} \\ \sigma_{zzn} = 2\mu\dfrac{\partial u_{zn}}{\partial z} + \lambda\Delta_n & \text{(2.47c)} \end{cases}$$

If the following Hankel transforms are defined

$$\pm\,\sigma_{21n}(k,z) + \sigma_{23n}(k,z) = \int_0^\infty (\sigma_{rzn} \pm \sigma_{\theta zn}) J_{n\pm1}(kr) r dr \tag{2.48}$$

$$\sigma_{22n}(k,z) = \int_0^\infty \sigma_{zzn} J_n(kr) r dr \tag{2.49}$$

then combining Equations $(2.47a)$ and $(2.47b)$ and applying Hankel transforms, results in

$$\pm\,\sigma_{21n} + \sigma_{23n} = \mu\left[\mp k u_{2n} + \frac{\partial}{\partial z}(\pm u_{1n} + u_{3n})\right] \tag{2.50}$$

$$\sigma_{22n} = (\lambda + 2\mu)\frac{\partial u_{2n}}{\partial z} + \lambda(k u_{1n}) \tag{2.51}$$

Substituting the expressions obtained for u_{1n}, u_{2n} and u_{3n} (Eqs. (2.43) and (2.44)) in Eqs. (2.50) and (2.51), the transformed stresses σ_{21n}, σ_{23n} and σ_{22n} can be expressed as

$$\begin{Bmatrix} \sigma_{21n}(k,z) \\ \sigma_{22n}(k,z) \end{Bmatrix} = \mu \begin{bmatrix} 2\alpha k & -(k^2+\gamma^2) & -2\alpha k & (k^2+\gamma^2) \\ (k^2+\gamma^2) & -2\gamma k & (k^2+\gamma^2) & -2\gamma k \end{bmatrix} \begin{Bmatrix} C_{1n}\, e^{-\alpha z} \\ C_{2n}\, e^{-\gamma z} \\ C_{3n}\, e^{\alpha z} \\ C_{4n}\, e^{-\gamma z} \end{Bmatrix}$$

$$+ \begin{Bmatrix} -k f_{2n}/\gamma^2 \\ \lambda k f_{1n}/\alpha^2(\lambda+2\mu) \end{Bmatrix} \tag{2.52}$$

$$\sigma_{23n}(k,z) = \mu[-\gamma \quad \gamma] \begin{Bmatrix} C_{5n}\, e^{-\gamma z} \\ C_{6n}\, e^{\gamma z} \end{Bmatrix} \tag{2.53}$$

It is important to notice that the solution of u_{3n} involves only γ. From this point, all quantities associated with u_{3n} will be identified as "SH-wave" quantities, whereas "SV-P waves" will be used to refer to quantities associated with u_{1n} and u_{2n}.

Layer stiffness matrix and load vector for SV-P waves

Equation (2.43) can be used to obtain the expressions for the transformed displacements u_{1n} and u_{2n} of the planes A and B (Fig. 2.5b) associated with local coordinates $z' = 0$ and $z' = h$. The resulting matrix can be written as

$$\begin{Bmatrix} u_{1n}^A - \bar{u}_{1n} \\ u_{2n}^A - \bar{u}_{2n} \\ u_{1n}^B - \bar{u}_{1n} \\ u_{2n}^B - \bar{u}_{2n} \end{Bmatrix} = \begin{bmatrix} -k & \gamma & -k & \gamma \\ -\alpha & k & \alpha & -k \\ -k\,e^{-\alpha h} & \gamma\,e^{-\gamma h} & -k\,e^{\alpha h} & \gamma\,e^{\gamma h} \\ -\alpha\,e^{-\alpha h} & k\,e^{-\gamma h} & \alpha\,e^{\alpha h} & -k\,e^{\gamma h} \end{bmatrix} \begin{Bmatrix} C_{1n} \\ C_{2n} \\ C_{3n} \\ C_{4n} \end{Bmatrix} \tag{2.54}$$

where $\bar{u}_{1n}$ and $\bar{u}_{2n}$ are

$$\begin{cases} \bar{u}_{1n} = f_{1n}/\alpha^2(\lambda + 2\mu) & \text{(2.55a)} \\ \bar{u}_{2n} = f_{2n}/\gamma^2\mu & \text{(2.55b)} \end{cases}$$

In a similar way, Eq. (2.52) can be used to express the transformed stresses σ_{21n} and σ_{22n} on the exterior side of these planes as

$$\begin{Bmatrix} \sigma_{21n}^A + \bar{\sigma}_{21n} \\ \sigma_{22n}^A + \bar{\sigma}_{22n} \\ \sigma_{21n}^B + \bar{\sigma}_{21n} \\ \sigma_{22n}^B + \bar{\sigma}_{22n} \end{Bmatrix} = \mu \begin{Bmatrix} -2\alpha k & (k^2+\gamma^2) & 2\alpha k & -(k^2+\gamma^2) \\ -(k^2+\gamma^2) & 2\gamma k & -(k^2+\gamma^2) & 2\gamma k \\ 2\alpha k e^{-\alpha h} & -(k^2+\gamma^2) & -2\alpha k e^{\alpha h} & (k^2+\gamma^2)e^{\gamma h} \\ (k^2+\gamma^2)e^{-\alpha h} & -2\gamma k e^{-\gamma h} & (k^2+\gamma^2)e^{\alpha h} & -2\gamma k e^{\gamma h} \end{Bmatrix} \begin{Bmatrix} C_{1n} \\ C_{2n} \\ C_{3n} \\ C_{4n} \end{Bmatrix} \tag{2.56}$$

where $\bar{\sigma}_{21n}$ and $\bar{\sigma}_{22n}$ are

$$\begin{cases} \bar{\sigma}_{21n} = -k f_{2n}/\gamma^2 & \text{(2.57a)} \\ \bar{\sigma}_{22n} = \lambda k f_{1n}/\alpha^2(\lambda + 2\mu) & \text{(2.57b)} \end{cases}$$

Isolating the unknown constants vector in Eqs. (2.54) and (2.56) and then combining the

resulting expressions, the following equation can be written:

$$\left\{\sigma_{SV-P}^{AB}\right\} = \left[K_{SV-P}^{AB}\right]\left\{u_{SV-P}^{AB}\right\} + \left\{\bar{\sigma}_{SV-P}^{AB}\right\} \tag{2.58}$$

where $\left\{\sigma_{SV-P}^{AB}\right\}$ and $\left\{u_{SV-P}^{AB}\right\}$ are the transformed stress and displacements vectors given by

$$\left\{\sigma_{SV-P}^{AB}\right\} = \begin{Bmatrix} \sigma_{21n}^{A} \\ \sigma_{22n}^{A} \\ \sigma_{21n}^{B} \\ \sigma_{22n}^{B} \end{Bmatrix}; \left\{u_{SV-P}^{AB}\right\} = \begin{Bmatrix} u_{1n}^{A} \\ u_{2n}^{A} \\ u_{1n}^{B} \\ u_{2n}^{B} \end{Bmatrix}; \tag{2.59}$$

and $\left\{\bar{\sigma}_{SV-P}^{AB}\right\}$ is the vector of "fixed-end stresses" given by (Kaynia, 1982)

$$\left\{\bar{\sigma}_{SV-P}^{AB}\right\} = -\left[K_{SV-P}^{AB}\right]\begin{Bmatrix} \bar{u}_{1n} \\ \bar{u}_{2n} \\ \bar{u}_{1n} \\ \bar{u}_{2n} \end{Bmatrix} + \begin{Bmatrix} -\bar{\sigma}_{21n} \\ -\bar{\sigma}_{22n} \\ \bar{\sigma}_{21n} \\ \bar{\sigma}_{22n} \end{Bmatrix} \tag{2.60}$$

The elements of the symmetric 4×4 layer stiffness matrix K_{SV-P}^{AB} are given by

$$
\begin{aligned}
K_{11} &= \frac{1}{D}\mu\alpha(k^2-\gamma^2)\left[\alpha\gamma S^{\alpha}C^{\gamma} - k^2 S^{\gamma}C^{\alpha}\right] \\
K_{21} &= \frac{1}{D}\mu k\left[\alpha\gamma(3k^2+\gamma^2)(C^{\alpha}C^{\gamma}1) - (k^4+k^2\gamma^2+2\alpha^2\gamma^2)S^{\alpha}S^{\gamma}\right] \\
K_{31} &= \frac{1}{D}\mu\alpha(k^2-\gamma^2)\left[k^2 S^{\gamma} - \alpha\gamma S^{\alpha}\right] \\
K_{41} &= \frac{1}{D}\mu k\alpha\gamma(k^2-\gamma^2)\left[C^{\gamma} - C^{\alpha}\right] \\
K_{22} &= \frac{1}{D}\mu\gamma(k^2-\gamma^2)\left[\alpha\gamma S^{\gamma}C^{\alpha} - k^2 S^{\alpha}C^{\gamma}\right] \\
K_{32} &= -K_{41} \\
K_{42} &= \frac{1}{D}\mu\gamma(k^2-\gamma^2)\left[k^2 S^{\alpha} - \alpha\gamma S^{\gamma}\right] \\
K_{33} &= K_{11} \\
K_{43} &= -K_{21} \\
K_{44} &= K_{22}
\end{aligned}
\tag{2.61}
$$

where

$$
D = \alpha\gamma\left[-2k^2 + 2k^2 C^{\alpha}C^{\gamma} - \frac{\alpha^2\gamma^2+k^4}{\alpha\gamma}S^{\alpha}S^{\gamma}\right] \tag{2.62}
$$

and

$$
\begin{aligned}
C^{\alpha} &\equiv \cosh(\alpha h) \quad ; \quad S^{\alpha} \equiv \sinh(\alpha h) \\
C^{\gamma} &\equiv \cosh(\gamma h) \quad ; \quad S^{\gamma} \equiv \sinh(\gamma h)
\end{aligned}
\tag{2.63}
$$

For the case in which $|\omega/kC_s| \ll 1$, Kaynia (1982) recommended to use the asymptotic

values of these expressions to avoid errors in the operations. Therefore,

$$\begin{aligned}
K_{11} &\sim \frac{2}{D'}\mu k\left[kh(1-\varepsilon^2)-(1+\varepsilon^2)S^kC^k\right]\\
K_{21} &\sim \frac{2}{D'}\mu k\left[k^2h^2(1-\varepsilon^2)^2-\varepsilon^2(1+\varepsilon^2)(S^k)^2\right]\\
K_{31} &\sim \frac{2}{D'}\mu k\left[(1+\varepsilon^2)S^k-kh(1-\varepsilon^2)C^k\right]\\
K_{41} &\sim -\frac{2}{D'}\mu k\left[kh(1-\varepsilon^2)S^k\right]\\
K_{22} &\sim -\frac{2}{D'}\mu k\left[kh(1-\varepsilon^2)+(1+\varepsilon^2)S^kC^k\right]\\
K_{42} &\sim \frac{2}{D'}\mu k\left[(1+\varepsilon^2)S^k+kh(1-\varepsilon^2)C^k\right]
\end{aligned} \tag{2.64}$$

where

$$D' = k^2h^2(1-\varepsilon^2)^2-(1+\varepsilon^2)^2(S^k)^2, \tag{2.65}$$

$\varepsilon = C_s/C_p$, and C^k and S^k are

$$C^k \equiv \cosh(kh) \quad ; \quad S^k \equiv \sinh(kh) \tag{2.66}$$

Halfspace stiffness matrix for SV-P waves

In order to evaluate transformed displacements (Eq. (2.43)) and stresses (Eq. (2.52)) in a halfspace, it is required that the Sommerfeld's radiation condition (Sommerfeld, 1949) be satisfied. That is, the value of stresses and displacements should tend to zero as z approaches infinity. Therefore, the unknown constants C_{3n} and C_{4n} in Eqs. (2.43) and (2.52) are equal to zero. Thus,

$$\begin{Bmatrix} u^C_{1n} \\ u^C_{2n} \end{Bmatrix} = \begin{bmatrix} -k & \gamma \\ -\alpha & k \end{bmatrix} \begin{Bmatrix} C_{1n} \\ C_{2n} \end{Bmatrix} \tag{2.67}$$

$$\begin{Bmatrix} \sigma^C_{21n} \\ \sigma^C_{22n} \end{Bmatrix} = \mu \begin{bmatrix} -2\alpha k & k^2+\gamma^2 \\ -(k^2+\gamma^2) & 2\gamma k \end{bmatrix} \begin{Bmatrix} C_{1n} \\ C_{2n} \end{Bmatrix} \tag{2.68}$$

Combining Equations (2.67) and (2.68), gives

$$\begin{Bmatrix} \sigma_{21n}^C \\ \sigma_{22n}^C \end{Bmatrix} = \left[K_{SV-P}^C\right] \begin{Bmatrix} u_{1n}^C \\ u_{2n}^C \end{Bmatrix} \tag{2.69}$$

in which the symmetric 2×2 halfspace stiffness matrix is

$$\left[K_{SV-P}^C\right] = \frac{\mu}{k^2 - \alpha\gamma} \begin{bmatrix} \alpha(k^2 - \gamma^2) & k(k^2 + \gamma^2 - 2\alpha\gamma) \\ k(k^2 + \gamma^2 - 2\alpha\gamma) & \gamma(k^2 - \gamma^2) \end{bmatrix} \tag{2.70}$$

and when $|\omega/kC_s| \ll 1$

$$\left[K_{SV-P}^C\right] \sim \frac{2\mu k}{1 + \varepsilon^2} \begin{bmatrix} 1 & \varepsilon^2 \\ \varepsilon^2 & 1 \end{bmatrix} \tag{2.71}$$

Layer stiffness matrix and load vector for SH waves

Equations (2.44) and (2.53) can be used to express transformed displacements and external stresses associated with planes A and B (Fig. 2.5b), such that

$$\begin{Bmatrix} u_{3n}^A - \bar{u}_{3n} \\ u_{3n}^B - \bar{u}_{3n} \end{Bmatrix} = \begin{bmatrix} 1 & 1 \\ e^{-\gamma h} & e^{\gamma h} \end{bmatrix} \begin{Bmatrix} C_{5n} \\ C_{6n} \end{Bmatrix} \tag{2.72}$$

$$\begin{Bmatrix} \sigma_{23n}^A \\ \sigma_{23n}^B \end{Bmatrix} = \mu \begin{bmatrix} \gamma & -\gamma \\ -\gamma e^{-\gamma h} & \gamma e^{\gamma h} \end{bmatrix} \begin{Bmatrix} C_{5n} \\ C_{6n} \end{Bmatrix} \tag{2.73}$$

where $\bar{u}_{3n} = f_{3n}/\gamma^2\mu$. Combining Eqs. (2.72) and (2.73), gives

$$\left\{\sigma_{SH}^{AB}\right\} = \left[K_{SH}^{AB}\right] \left\{u_{SH}^{AB}\right\} + \left\{\bar{\sigma}_{SH}^{AB}\right\} \tag{2.74}$$

where $\left\{\sigma_{SH}^{AB}\right\}$ and $\left\{u_{SH}^{AB}\right\}$ are the stress and displacement vectors expressed as

$$\left\{\sigma_{SH}^{AB}\right\} = \begin{Bmatrix} \sigma_{23n}^A \\ \sigma_{23n}^B \end{Bmatrix} \quad ; \quad \left\{u_{SH}^{AB}\right\} = \begin{Bmatrix} u_{3n}^A \\ u_{3n}^B \end{Bmatrix} \tag{2.75}$$

and $\left\{\bar{\sigma}_{SH}^{AB}\right\}$ is the vector of "fixed-end stresses" given by (Kaynia, 1982)

$$\left\{\bar{\sigma}_{SH}^{AB}\right\} = -\left[K_{SH}^{AB}\right] \begin{Bmatrix} \bar{u}_{3n} \\ \bar{u}_{3n} \end{Bmatrix} \tag{2.76}$$

and the 2×2 layer stiffness matrix is

$$\left[K_{SH}^{AB}\right] = \frac{\gamma\mu}{\sinh(\gamma h)} \begin{bmatrix} \cosh(\gamma h) & -1 \\ -1 & \cosh(\gamma h) \end{bmatrix} \tag{2.77}$$

Halfspace stiffness matrix for SH waves

The expressions for the transformed stress and displacement of plane C (Fig. 2.5c), resulting from imposition of the radiation condition into Eqs. (2.44) and (2.53) , are

$$u_{3n}^{C} = C_{5n} \tag{2.78}$$

$$\sigma_{23n}^{C} = \gamma\mu C_{5n} \tag{2.79}$$

Combining Eqs. (2.78) and (2.79), the following expression is obtained

$$\sigma_{23n}^{C} = \gamma\mu u_{3n}^{C} \tag{2.80}$$

2.1.3 Displacements within a layer

Since the nodes of each layer are located at their centers, the displacements of the middle of the layers need to be computed. The following expressions give the mid-layer transformed displacements.

Mid-layer transformed displacements for SV-P Waves

The transformed displacements of the center of the layer shown in Fig. 2.5 are related to those of planes A and B by

$$\begin{Bmatrix} u_{1n}^{E} \\ u_{2n}^{E} \end{Bmatrix} = \left[T_{SV-P}^{E}\right] \begin{Bmatrix} u_{1n}^{A} - \bar{u}_{1n} \\ u_{2n}^{A} - \bar{u}_{2n} \\ u_{1n}^{B} - \bar{u}_{1n} \\ u_{2n}^{B} - \bar{u}_{2n} \end{Bmatrix} + \begin{Bmatrix} \bar{u}_{1n} \\ \bar{u}_{2n} \end{Bmatrix} \tag{2.81}$$

in which the elements of $[T_{SV-P}^{E}]$ are

$$\begin{aligned}
T_{11} &= \frac{1}{D}\left[\alpha\gamma k^2(C^{\alpha}C^{\gamma/2} + C^{\alpha/2}C^{\gamma}) - \alpha^2\gamma^2 S^{\alpha}S^{\gamma/2} - k^4 S^{\alpha/2}S^{\gamma} - \alpha\gamma k^2(C^{\alpha/2} + C^{\gamma/2})\right] \\
T_{21} &= \frac{1}{D}\alpha k\left[\alpha\gamma(C^{\gamma}S^{\alpha/2} - C^{\gamma/2S^{\alpha}}) + k^2(S^{\gamma/2}C^{\alpha} - S^{\gamma}C^{\alpha/2}) + k^2 S^{\gamma/2} + \alpha\gamma S^{\alpha/2}\right] \\
T_{12} &= \frac{1}{D}\gamma k\left[\alpha\gamma(C^{\alpha S^{\gamma/2}} - C^{\alpha/2}S^{\gamma}) + k^2(S^{\alpha/2}C^{\gamma} - S^{\alpha}C^{\gamma/2}) + k^2 S^{\alpha/2} + \alpha\gamma S^{\gamma/2}\right] \\
T_{22} &= \frac{1}{D}\left[\alpha\gamma k^2(C^{\gamma}C^{\alpha/2} + C^{\gamma/2}C^{\alpha}) - \alpha^2\gamma^2 S^{\gamma}S^{\alpha/2} - k^4 S^{\gamma/2}S^{\alpha} - \alpha\gamma k^2(C^{\gamma/2} + C^{\alpha/2})\right] \\
T_{13} &= T_{11} \\
T_{23} &= -T_{21} \\
T_{14} &= -T_{12} \\
T_{24} &= T_{22}
\end{aligned} \tag{2.82}$$

and the symbols $C^{\alpha/2}$, $C^{\gamma/2}$, $S^{\alpha/2}$ and S^{γ} are denoted by

$$\begin{cases} C^{\alpha/2} \equiv \cosh(\alpha h/2) & S^{\alpha/2} \equiv \sinh(\alpha h/2) \\ C^{\gamma/2} \equiv \cosh(\gamma h/2) & S^{\gamma/2} \equiv \sinh(\gamma h/2) \end{cases} \tag{2.83}$$

For the case in which $|\omega/kC_s| \ll 1$, Kaynia (1982) defined the asymptotic value of the terms

of $[T^E_{SV-P}]$ as

$$\begin{aligned}
T_{11} &\sim \frac{1}{2D'}\left[khC^{k/2}(\varepsilon^2-1)+2S^{k/2}(1+\varepsilon^2)\right]\left[kh(\varepsilon^2-1)-2C^{k/2}S^{k/2}(1+\varepsilon^2)\right] \\
T_{21} &\sim \frac{1}{2D'}kh(1-\varepsilon^2)S^{k/2}\left[2(1+\varepsilon^2)S^{k/2}C^{k/2}-kh(1-\varepsilon^2)\right] \\
T_{12} &\sim \frac{1}{2D'}kh(1-\varepsilon^2)S^{k/2}\left[2(1+\varepsilon^2)S^{k/2}C^{k/2}+kh(1-\varepsilon^2)\right] \\
T_{22} &\sim \frac{1}{2D'}\left[khC^{k/2}(1-\varepsilon^2)+2S^{k/2}(1+\varepsilon^2)\right]\left[kh(1-\varepsilon^2)-2C^{k/2}S^{k/2}(1+\varepsilon^2)\right]
\end{aligned} \tag{2.84}$$

where $C^{k/2}$ and $S^{k/2}$ are

$$C^{k/2} \equiv \cosh(kh/2) \quad ; \quad S^{k/2} \equiv \sinh(kh/2) \tag{2.85}$$

Mid-layer transformed displacements for SH Waves

The transformed displacement of plane E (Fig. 2.5) in terms of the transformed displacement of planes A and B is

$$u^E_{3n} = \frac{1}{2\cosh(\gamma h/2)}\left(u^A_{3n}+u^B_{3n}-2\bar{u}_{3n}\right)+\bar{u}_{3n} \tag{2.86}$$

2.1.4 Integral representation

In this section, the derived transformed displacements u^E_{1n}, u^E_{2n} and u^E_{3n} are used to obtain the displacements in a layered soil media caused by uniform load distributions over cylindrical or circular surfaces. In the model proposed by Kaynia, the soil is divided into a number of layers in such a way that the traction distribution can be well represented. Each layer contains a cylindrical uniform load distribution which can be treated as body forces along the pile shafts for which the "fixed-end stresses" can be evaluated. At the pile tips, the circular loads can be considered as external forces at the interface of two layers.

Consider the uniform horizontal an vertical loads on cylindrical and circular surfaces presented in Fig. 2.6. The radii of the cylinders and circular surfaces are denoted by R, and the height

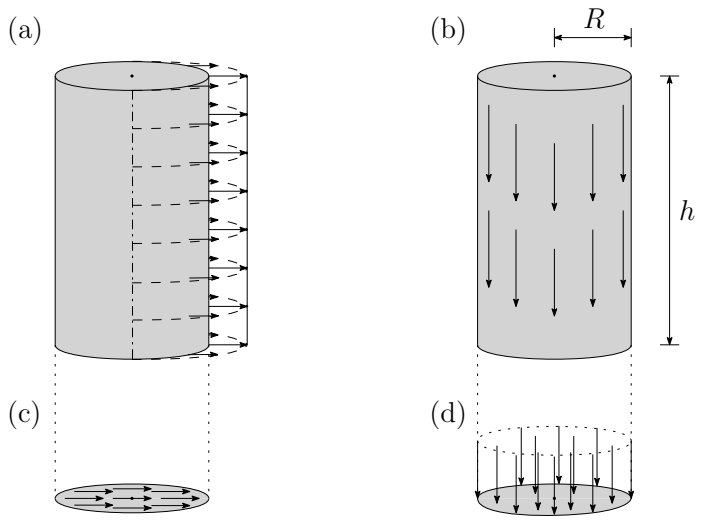

Figure 2.6: Type of loads in pile-soil interface

of the cylinders by h. These quantities also represent the radius of the piles and the thickness of a layer, respectively. The lateral load on a cylindrical surface (Fig. 2.6a) can be expressed in cylindrical coordinates as

$$\begin{cases} f_r(r,\theta,z) = \dfrac{1}{2\pi Rh}\delta(r-R)\cos\,\theta \\ f_\theta(r,\theta,z) = \dfrac{-1}{2\pi Rh}\delta(r-R)\sin\,\theta \\ f_z(r,\theta,z) = 0 \end{cases} \tag{2.87}$$

where δ represents the Dirac delta function. Comparing Eq. (2.87) with the expansion of loads in Eq. (2.21), it is obtained

$$\begin{cases} f_{r1} = \dfrac{1}{2\pi Rh}\delta(r-R) \\ f_{\theta 1} = \dfrac{-1}{2\pi Rh}\delta(r-R) \\ f_{z1} = 0 \end{cases} \tag{2.88}$$

and

$$f_{rn} = f_{\theta n} = f_{zn} = 0; \quad \text{for} \quad n \neq 1 \tag{2.89}$$

Since the values of the Fourier expansion of loads in Eq. (2.89) are zero for n different than one, the corresponding displacements are contributed only by the terms associated with n = 1.

Therefore, the displacement expansions reduce to

$$\begin{cases} u_r(r,\theta,z) = u_{r1}(r,z)\,\cos\,\theta \\ u_\theta(r,\theta,z) = u_{\theta 1}(r,z)\,\sin\,\theta \\ u_z(r,\theta,z) = u_{z1}(r,z)\,\cos\,\theta \end{cases} \tag{2.90}$$

Applying Hankel transforms (Eq. (2.29)) into f_{r1}, $f_{\theta 1}$ and f_{z1} yields

$$\begin{cases} f_{11} = -\dfrac{J_0(kR)}{2\pi h} \\ f_{21} = 0 \\ f_{31} = \dfrac{J_0(kR)}{2\pi h} \end{cases} \tag{2.91}$$

The transformed displacements associated with these transformed loads can be obtained by the procedure described in previous sections. If u_{11}, u_{21} and u_{31} correspond to $f_{11} = f_{31} = 1/2\pi h$ and $f_{21} = 0$, then actual transformed displacements associated with Eq. (2.91) are given by $-J_0(kR)u_{11}$, $-J_0(kR)u_{21}$ and $J_0(kR)u_{31}$. Therefore, the Hankel transform of displacements in Eq. (2.29) can be written as (n = 1)

$$\begin{cases} -J_0(kR)u_{11} + J_0(kR)u_{31} = \int_0^\infty (u_{r1} + u_{\theta 1})\, J_2(kR)\, r dr \\ J_0(kR)u_{11} + J_0(kR)u_{31} = \int_0^\infty (u_{r1} - u_{\theta 1})\, J_0(kR)\, r dr \\ -J_0(kR)u_{21} = \int_0^\infty u_{z1} J_1(kr)\, r dr \end{cases} \tag{2.92}$$

The application of inverse Hankel transform to these equations results

$$\begin{cases} u_{r1} + u_{\theta 1} = \int_0^\infty (-u_{11} + u_{31}) J_0(kR)\, J_2(kr)\, k dk \\ u_{r1} - u_{\theta 1} = \int_0^\infty (u_{11} + u_{31}) J_0(kR)\, J_0(kr)\, k dk \\ u_{z1} = \int_0^\infty (-u_{21}) J_0(kR)\, J_1(kr)\, k dk \end{cases} \tag{2.93}$$

Using the recurrence relations for the Bessel functions, the following integral representation for

u_{r1}, $u_{\theta 1}$ and u_{z1} can be obtained

$$\begin{cases} u_{r1} = \dfrac{1}{2\pi h}\int_0^\infty \left[u_{11}J_0(kr)\,J_0(kR) + (u_{31}-u_{11})\dfrac{J_1(kr)}{kr}\,J_0(kR)\right]\,kdk \\ u_{\theta 1} = -\dfrac{1}{2\pi h}\int_0^\infty \left[u_{31}J_0(kr)\,J_0(kR) + (u_{11}-u_{31})\dfrac{J_1(kr)}{kr}\,J_0(kR)\right]\,kdk \\ u_{z1} = -\dfrac{1}{2\pi h}\int_0^\infty u_{21}\,J_1(kr)\,J_0(kR)\,kdk \end{cases} \tag{2.94}$$

For a frictional force on a cylindrical surface (Fig. 2.6b), the integral representation of corresponding displacements can be obtained in a similar scheme. Initially, the load distribution can be written as

$$\begin{cases} f_r(r,\theta,z) = 0 \\ f_\theta(r,\theta,z) = 0 \\ f_z(r,\theta,z) = \dfrac{1}{2\pi Rh}\delta(r-R) \end{cases} \tag{2.95}$$

Comparing Eq. (2.95) with the expansion of loads in Eq. (2.21), it is obtained

$$\begin{cases} f_{r0} = 0 \\ f_{\theta 0} = 0 \\ f_{z0} = \dfrac{1}{2\pi Rh}\delta(r-R) \end{cases} \tag{2.96}$$

and

$$f_{rn} = f_{\theta n} = f_{zn} = 0; \quad \text{for} \quad n \neq 0 \tag{2.97}$$

The load expansion is only a nonzero term when $n = 0$. In this case, the displacement expansion also has a non-zero value, whereas all other terms will vanish when $n \neq 0$. Therefore,

$$\begin{cases} u_r(r,\theta,z) = u_{r0}(r,z) \\ u_\theta(r,\theta,z) = 0 \\ u_z(r,\theta,z) = u_{z0}(r,z) \end{cases} \tag{2.98}$$

Applying the procedure described for horizontal loading, it is obtained that u_{10} and u_{20} are transformed displacements due to transformed loads $f_{10} = 0$ and $f_{20} = 1/2\pi h$. Therefore, u_{r0} and u_{z0} are written as

$$\begin{cases} u_{r0} = \dfrac{1}{2\pi h} \int_0^\infty u_{10} J_1(kr)\, J_0(kR)\, kdk \\ u_{z0} = \dfrac{1}{2\pi h} \int_0^\infty u_{20} J_0(kr)\, J_0(kR)\, kdk \end{cases} \tag{2.99}$$

For the loads distributed over circular surfaces (Figs. 2.6c and 2.6d), it is necessary that the corresponding transformed forces be evaluated directly. Consider first the frictional force on a circular face (Fig. 2.6c). This load can be represented by

$$\begin{cases} \bar{\sigma}_{rz} = \dfrac{1}{\pi R^2} \cos\theta \\ \bar{\sigma}_{\theta z} = \dfrac{-1}{\pi R^2} \sin\theta \qquad\qquad r \le R \\ \bar{\sigma}_{zz} = 0 \end{cases} \tag{2.100}$$

$$\bar{\sigma}_{rz} = \bar{\sigma}_{\theta z} = \bar{\sigma}_{zz} = 0; \qquad\qquad r > R$$

Applying a Fourier expansion of these loads and comparing with Eq. (2.100), it can be concluded that

$$\begin{cases} \bar{\sigma}_{rz1} = \dfrac{1}{\pi R^2} \\ \bar{\sigma}_{\theta z1} = \dfrac{-1}{\pi R^2} \\ \bar{\sigma}_{zz1} = 0 \end{cases} \tag{2.101}$$

and

$$\bar{\sigma}_{rzn} = \bar{\sigma}_{\theta zn} = \bar{\sigma}_{zzn} = 0; \quad \text{for} \quad n \neq 1 \tag{2.102}$$

Therefore, only the terms associated with $n = 1$ in the expansion of displacements u_r, u_θ and u_z need to be considered (Eq. (2.90)). Applying the Hankel transforms into Eq. (2.101), the

transformed loads associated with $\bar{\sigma}_{rz1}$, $\bar{\sigma}_{\theta z1}$ and $\bar{\sigma}_{zz1}$ are obtained, which are given by

$$\begin{cases} \bar{\sigma}_{211} = -\dfrac{1}{\pi}\dfrac{J_1(kR)}{kR} \\ \bar{\sigma}_{221} = 0 \\ \bar{\sigma}_{231} = \dfrac{1}{\pi}\dfrac{J_1(kR)}{kR} \end{cases} \tag{2.103}$$

For this case, the integral representation of u_{r1}, $u_{\theta 1}$ and u_{z1}, which is obtained by a similar procedure described for the loads on cylindrical surfaces, is represented by Eq. (2.94), except that the term $J_0(kR)$ is replaced by $J_1(kR)/kR$ and $1/2\pi h$ is replaced by $1/\pi$. The transformed displacements u_{11}, u_{21} and u_{31} in these equations correspond to transformed applied stresses $\bar{\sigma}_{211} = 1/\pi$, $\bar{\sigma}_{221} = 0$ and $\bar{\sigma}_{231} = 1/\pi$.

For the vertical force on a circular surface (Fig. 2.6d), only the terms associated with $n = 0$ in the Fourier expansions are considered and the expressions for displacements are given by Eq. (2.99), except that the term $J_0(kR)$ should be replaced by $J_1(kR)/kR$ and $1/2\pi h$ should be replaced by $1/\pi$. The transformed displacements u_{10} and u_{20} in these equations correspond to the transformed applied stresses $\bar{\sigma}_{210} = 0$ and $\bar{\sigma}_{220} = 1/\pi$.

2.1.5 Assembly of the flexibility matrix

In order to understand how the flexibility matrix of the soil is assembled, consider the example shown in Fig. 2.7.

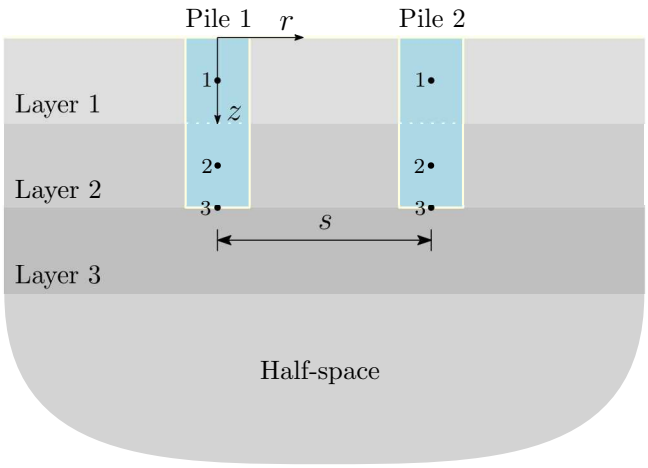

Figure 2.7: Pile group in a multilayered media

For this case, the integral representations presented in Equations (2.94 and 2.99) must be obtained for $r = 0$ (Pile 1) and $r = s$ (Pile 2). The transformed displacements at the central nodes of the Pile 1 are

$$u_{11}^{E} = \begin{bmatrix} u_{11}^{u_1,f_1} & u_{11}^{u_1,f_2} & u_{11}^{u_1,f_3} \\ u_{11}^{u_2,f_1} & u_{11}^{u_2,f_2} & u_{11}^{u_2,f_3} \\ u_{11}^{u_3,f_1} & u_{11}^{u_3,f_2} & u_{11}^{u_3,f_3} \end{bmatrix}, \; u_{21}^{E} = \begin{bmatrix} u_{21}^{u_1,f_1} & u_{21}^{u_1,f_2} & u_{21}^{u_1,f_3} \\ u_{21}^{u_2,f_1} & u_{21}^{u_2,f_2} & u_{21}^{u_2,f_3} \\ u_{21}^{u_3,f_1} & u_{21}^{u_3,f_2} & u_{21}^{u_3,f_3} \end{bmatrix}, \; u_{31}^{E} = \begin{bmatrix} u_{31}^{u_1,f_1} & u_{31}^{u_1,f_2} & u_{31}^{u_1,f_3} \\ u_{31}^{u_2,f_1} & u_{31}^{u_2,f_2} & u_{31}^{u_2,f_3} \\ u_{31}^{u_3,f_1} & u_{31}^{u_3,f_2} & u_{31}^{u_3,f_3} \end{bmatrix}, \tag{2.104}$$

$$u_{10}^{E} = \begin{bmatrix} u_{10}^{u_1,f_1} & u_{10}^{u_1,f_2} & u_{10}^{u_1,f_3} \\ u_{10}^{u_2,f_1} & u_{10}^{u_2,f_2} & u_{10}^{u_2,f_3} \\ u_{10}^{u_3,f_1} & u_{10}^{u_3,f_2} & u_{10}^{u_3,f_3} \end{bmatrix}, \; u_{20}^{E} = \begin{bmatrix} u_{20}^{u_1,f_1} & u_{20}^{u_1,f_2} & u_{20}^{u_1,f_3} \\ u_{20}^{u_2,f_1} & u_{20}^{u_2,f_2} & u_{20}^{u_2,f_3} \\ u_{20}^{u_3,f_1} & u_{20}^{u_3,f_2} & u_{20}^{u_3,f_3} \end{bmatrix} \tag{2.105}$$

where the terms u^{u_i,f_j} of each matrix represent the displacement of node i due to a load at node j. Substituting the terms of these matrices into the expressions of the displacements in the spatial domain (Eqs. (2.94) and (2.99)), the following matrices are obtained

$$u_{r1} = \begin{bmatrix} u_{r1}^{u_1,f_1} & u_{r1}^{u_1,f_2} & u_{r1}^{u_1,f_3} \\ u_{r1}^{u_2,f_1} & u_{r1}^{u_2,f_2} & u_{r1}^{u_2,f_3} \\ u_{r1}^{u_3,f_1} & u_{r1}^{u_3,f_2} & u_{r1}^{u_3,f_3} \end{bmatrix}, \; u_{\theta 1} = \begin{bmatrix} u_{\theta 1}^{u_1,f_1} & u_{\theta 1}^{u_1,f_2} & u_{\theta 1}^{u_1,f_3} \\ u_{\theta 1}^{u_2,f_1} & u_{\theta 1}^{u_2,f_2} & u_{\theta 1}^{u_2,f_3} \\ u_{\theta 1}^{u_3,f_1} & u_{\theta 1}^{u_3,f_2} & u_{\theta 1}^{u_3,f_3} \end{bmatrix}, \; u_{z1} = \begin{bmatrix} u_{z1}^{u_1,f_1} & u_{z1}^{u_1,f_2} & u_{z1}^{u_1,f_3} \\ u_{z1}^{u_2,f_1} & u_{z1}^{u_2,f_2} & u_{z1}^{u_2,f_3} \\ u_{z1}^{u_3,f_1} & u_{z1}^{u_3,f_2} & u_{z1}^{u_3,f_3} \end{bmatrix}, \tag{2.106}$$

$$u_{r0} = \begin{bmatrix} u_{r0}^{u_1,f_1} & u_{r0}^{u_1,f_2} & u_{r0}^{u_1,f_3} \\ u_{r0}^{u_2,f_1} & u_{r0}^{u_2,f_2} & u_{r0}^{u_2,f_3} \\ u_{r0}^{u_3,f_1} & u_{r0}^{u_3,f_2} & u_{r0}^{u_3,f_3} \end{bmatrix}, \; u_{z0} = \begin{bmatrix} u_{z0}^{u_1,f_1} & u_{z0}^{u_1,f_2} & u_{z0}^{u_1,f_3} \\ u_{z0}^{u_2,f_1} & u_{z0}^{u_2,f_2} & u_{z0}^{u_2,f_3} \\ u_{z0}^{u_3,f_1} & u_{z0}^{u_3,f_2} & u_{z0}^{u_3,f_3} \end{bmatrix} \tag{2.107}$$

It is worth noting that the term $1/2\pi h$ should be replaced by $1/\pi$ for the integrals contained

in the last column of each matrix, since this position represents the displacements due to the load on pile tip. The same procedure is used to obtain the matrices of integral representations for Pile 2.

The terms in the diagonal of the flexibility matrix are represented by the displacements at the nodes of one pile due to the loads at the nodes of the same pile, whereas the terms out of the diagonal represent the displacements at the nodes of one pile due to the loads at the nodes of the other pile. The flexibility matrix of the Pile 1 is given by

$$F_s^1 = \begin{bmatrix} u_{r1}^1(1,1) & 0 & 0 & u_{r1}^1(1,2) & 0 & 0 & u_{r1}^1(1,3) & 0 & 0 \\ 0 & u_{r1}^1(1,1) & 0 & 0 & u_{r1}^1(1,2) & 0 & 0 & u_{r1}^1(1,3) & 0 \\ 0 & 0 & u_{z0}^1(1,1) & 0 & 0 & u_{z0}^1(1,2) & 0 & 0 & u_{z0}^1(1,3) \\ u_{r1}^1(2,1) & 0 & 0 & u_{r1}^1(2,2) & 0 & 0 & u_{r1}^1(2,3) & 0 & 0 \\ 0 & u_{r1}^1(2,1) & 0 & 0 & u_{r1}^1(2,2) & 0 & 0 & u_{r1}^1(2,3) & 0 \\ 0 & 0 & u_{z0}^1(2,1) & 0 & 0 & u_{z0}^1(2,2) & 0 & 0 & u_{z0}^1(2,3) \\ u_{r1}^1(3,1) & 0 & 0 & u_{r1}^1(3,2) & 0 & 0 & u_{r1}^1(3,3) & 0 & 0 \\ 0 & u_{r1}^1(3,1) & 0 & 0 & u_{r1}^1(3,2) & 0 & 0 & u_{r1}^1(3,3) & 0 \\ 0 & 0 & u_{z0}^1(3,1) & 0 & 0 & u_{z0}^1(3,2) & 0 & 0 & u_{z0}^1(3,3) \end{bmatrix} \tag{2.108}$$

The same scheme of Equation (2.108) is used to obtain the flexibility matrix of Pile 2, that is, F_s^2. The flexibility matrix of the interaction between Pile 1 and Pile 2, F_s^{1-2}, is given by

$$F_s^{1-2} = \begin{bmatrix} F_s^{1-2}[u(1,1)] & F_s^{1-2}[u(1,2)] & F_s^{1-2}[u(1,3)] \\ F_s^{1-2}[u(2,1)] & F_s^{1-2}[u(2,2)] & F_s^{1-2}[u(2,3)] \\ F_s^{1-2}[u(3,1)] & F_s^{1-2}[u(3,2)] & F_s^{1-2}[u(3,3)] \end{bmatrix} \tag{2.109}$$

where $F_s^{1-2}[u(i,j)]$ are 3×3 sub-matrices, the terms of which are expressed as

$$
\begin{aligned}
F_s^{1-2}[u(i,j)](1,1) &= (u_{r1}^1(i,j) + u_{r1}^2(i,j))\cos^2\theta - (u_{t1}^1(i,j) + u_{t1}^2(i,j))\sin^2\theta \\
F_s^{1-2}[u(i,j)](2,1) &= (u_{r1}^1(i,j) + u_{r1}^2(i,j))\cos\theta\sin\theta - (u_{t1}^1(1,1) + u_{t1}^2(i,j))\sin\theta\cos\theta \\
F_s^{1-2}[u(i,j)](3,1) &= (u_{z1}^1(i,j) + u_{z1}^2(i,j))\cos\theta \\
F_s^{1-2}[u(i,j)](1,2) &= (u_{r1}^1(i,j) + u_{r1}^2(i,j))\sin\theta\cos\theta - (u_{t1}^1(i,j) + u_{t1}^2(i,j))\cos\theta\sin\theta \\
F_s^{1-2}[u(i,j)](2,2) &= (u_{r1}^1(i,j) + u_{r1}^2(i,j)\sin^2\theta - (u_{t1}^1(i,j) + u_{t1}^2(i,j)\cos^2\theta \\
F_s^{1-2}[u(i,j)](3,2) &= (u_{z1}^1(i,j) + u_{z1}^2(i,j))\sin\theta \\
F_s^{1-2}[u(i,j)](1,3) &= (u_{r0}^1(i,j) + u_{r0}^2(i,j))\cos\theta \\
F_s^{1-2}[u(i,j)](2,3) &= (u_{r0}^1(i,j) + u_{r0}^2(i,j))\sin\theta \\
F_s^{1-2}[u(i,j)](3,3) &= (u_{z0}^1(i,j) + u_{z0}^2(i,j))
\end{aligned}
\tag{2.110}
$$

and θ is the angle between the piles. Figure 2.8 illustrates the profile of the flexibility matrix of soil.

$$
[\mathbf{F_s}] = \begin{bmatrix} F_s^1 & \text{Sym} \\ F_s^{1-2} & F_s^2 \end{bmatrix}
$$

Figure 2.8: Scheme of assemble of flexibility matrix of soil

Figure 2.9 shows the final profile of this matrix if two more piles are added into the system.

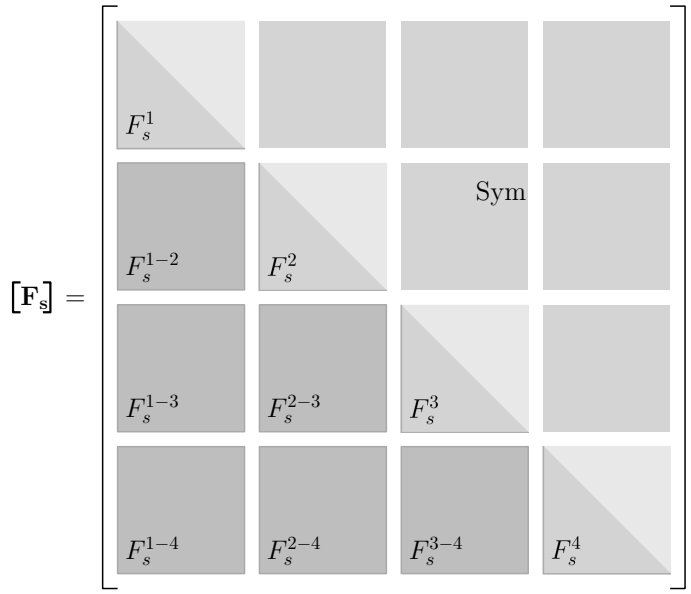

Figure 2.9: Scheme of assemble of flexibility matrix of soil for a group of four piles

2.1.6 Evaluation of influence functions

It can be observed in Equations (2.94) and (2.99) that the expressions for displacements involve integrals of the form

$$I = \int_0^\infty f(k) J_n(kr)\, J_m(kR)\, dk \tag{2.111}$$

in which the integrand is composed by a function $f(k)$ and a product of Bessel functions. Figure 2.10 shows the real part of the integrand of $u_{r1}^{u_1,f_1}$ (Eq. (2.106)) represented by u_{r1}^*. Notice that there are two well-defined regions. The first region is characterized by the presence of singularities, which are associated with surface wave modes. As the number of layers increases more singularities appear in the integrand. The second region is characterized by a smooth and decaying oscillation, which is defined from the argument of Bessel functions.

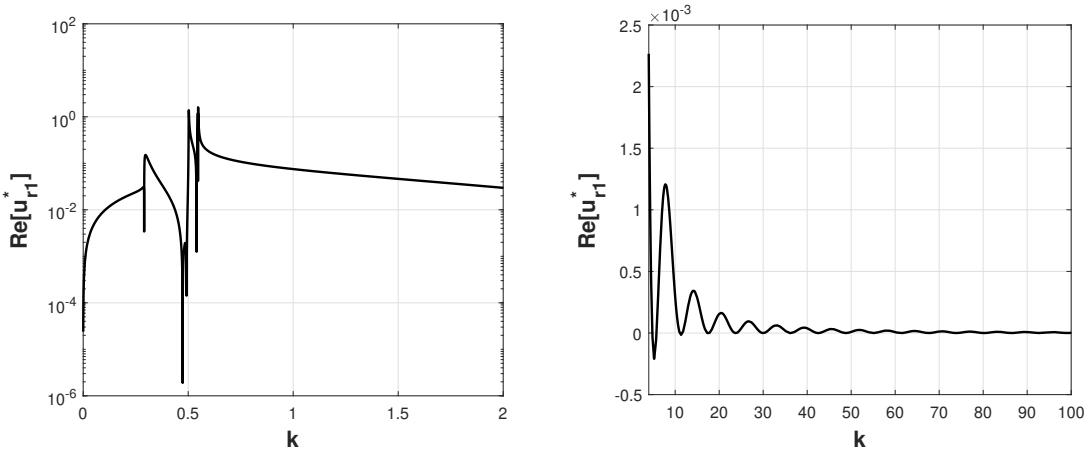

Figure 2.10: Integrand representation of $Re[u_{r1}^{u_1,f_1}]$ (Equation (2.106)).

This peculiar behavior of the integrand requires an appropriate numerical evaluation to ensure consistent results. The works of Vasconcelos et al. (2017) and Cavalcante et al. (2017) investigated a set of numerical methods for evaluation of each region of such integrand. For the first region, the adaptive quadrature showed a good approximation. This technique uses the idea of a standard quadrature, which is to divide the domain integration into a number of discrete intervals, and add more intervals at the sections that contain a singularity. For the second region, Cavalcante et al. (2017) showed that an extrapolation method performs an accurate evaluation of improper integrals. A considerable quantity of numerical packages encompassing these methods are available. In this research, the QUADPACK package was used (for more details about the numerical integration of such functions, see Section 2.5).

In the next sections, the stiffness and flexibility matrices of the piles are obtained. The piles are modeled with a beam element, which has three degrees of freedom per node (two lateral vibration, corresponding to translation and rotation, and one axial vibration, corresponding to axial displacement).

2.2 Dynamic stiffness matrix of the piles $\mathbf{K_p}$

The differential equation of a beam in steady-state lateral vibration, including the axial force effect (Fig. 2.11) is given by

$$\frac{d^4u}{dz^4} + \left(\frac{H}{EI}\right)\frac{d^2u}{dz^2} - \left(\frac{m\omega^2}{EI}\right)u = 0 \tag{2.112}$$

where m is the mass per unit length of the beam, H is the constant axial force in the beam and EI is the flexural rigidity of the beam.

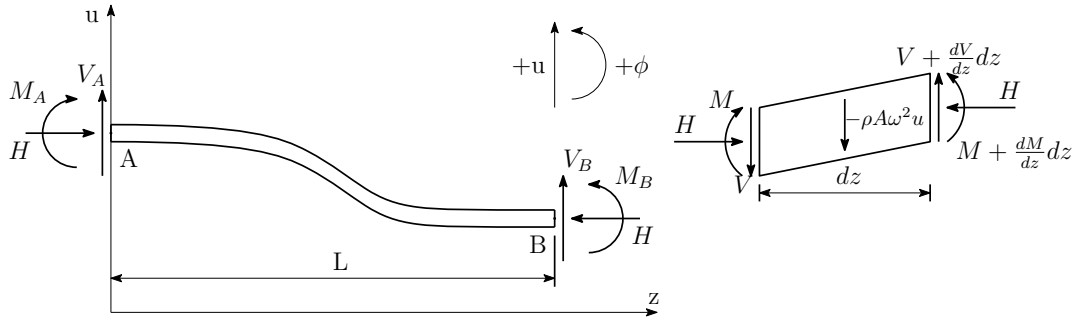

Figure 2.11: Beam in steady-state lateral vibration.

The solution of Eq. (2.112) can be written as

$$u = C_1\cos(\eta z) + C_2\sin(\eta z) + C_3\cosh(\xi z) + C_4\sinh(\xi z) \tag{2.113}$$

where

$$\begin{cases} \eta = \left\{\left[\left(\dfrac{H}{2EI}\right)^2 + \dfrac{m\omega^2}{EI}\right]^2 + \dfrac{H}{2EI}\right\}^{1/2} \\ \xi = \left\{\left[\left(\dfrac{H}{2EI}\right)^2 + \dfrac{m\omega^2}{EI}\right]^2 - \dfrac{H}{2EI}\right\}^{1/2} \end{cases} \tag{2.114}$$

The dynamic stiffness matrix of the beam is obtained by relating the forces at the two ends

with their corresponding displacements. Therefore,

$$\begin{Bmatrix} V_A \\ M_A \\ V_B \\ M_B \end{Bmatrix} = \left[\mathbf{K^l}\right] \begin{Bmatrix} u_A \\ \phi_A \\ u_B \\ \phi_B \end{Bmatrix} \tag{2.115}$$

where the terms of the symmetric 4×4 dynamic stiffness matrix $\mathbf{K^l}$ are given by

$$\begin{aligned}
K^l_{11} &= \frac{EI}{T_0}(\eta^2 + \xi^2)(\eta\, S^\eta\, C^\xi + \xi\, C^\eta\, S^\xi) \\
K^l_{21} &= \frac{EI}{T_0}[(\eta^2 - \xi^2)(1 - C^\eta\, C^\xi) + 2\,\eta\xi\, S^\eta\, S^\xi] \\
K^l_{31} &= -\frac{EI}{T_0}(\eta^2 + \xi^2)(\eta\, S^\eta + \xi\, S^\xi) \\
K^l_{41} &= \frac{EI}{T_0}(\eta^2 + \xi^2)(C^\xi - C^\eta) \\
K^l_{22} &= \frac{EI}{T_0}\left(\frac{\eta}{\xi} + \frac{\xi}{\eta}\right)(\xi\, S^\eta\, C^\xi - \eta\, C^\eta\, S^\xi) \\
K^l_{32} &= -\frac{EI}{T_0}(\eta^2 + \xi^2)(C^\xi - C^\eta) \\
K^l_{42} &= \frac{EI}{T_0}\left(\frac{\eta}{\xi} + \frac{\xi}{\eta}\right)(\eta\, S^\xi - \xi\, S^\eta) \\
K^l_{33} &= K_{11} \\
K^l_{43} &= -K_{21} \\
K^l_{44} &= K_{22}
\end{aligned} \tag{2.116}$$

where

$$T_0 = 2 - 2\, C^\eta\, C^\xi - \left(\frac{\eta}{\xi} - \frac{\xi}{\eta}\right) S^\eta\, S^\xi \tag{2.117}$$

and

$$\begin{aligned}
C^\eta &\equiv \cos(\eta L) \quad ; \quad S^\eta \equiv \sin(\eta L) \\
C^\xi &\equiv \cosh(\xi L) \quad ; \quad S^\eta \equiv \sinh(\xi L)
\end{aligned} \tag{2.118}$$

in which L is the length of the beam.

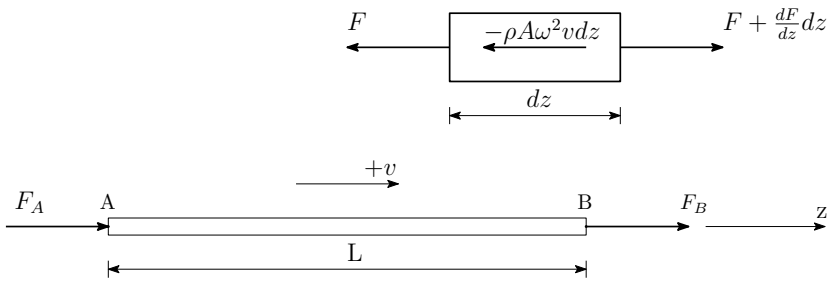

Figure 2.12: Beam in steady-state axial vibration.

Now, considering the case of the steady-state axial vibration of a beam (Fig. 2.12). The differential equation is

$$\frac{d^2v}{dz^2} + \frac{m}{EA}\omega^2 v = 0 \tag{2.119}$$

The solution of this equation can be written as

$$v = C_1 \cos(\zeta z) + C_2 \sin(\zeta z) \tag{2.120}$$

where

$$\zeta = \left(\frac{m\omega^2}{EA}\right)^{1/2} \tag{2.121}$$

The dynamic stiffness matrix can be obtained by the same procedure done in the lateral vibration. Therefore,

$$\begin{Bmatrix} F_A \\ F_B \end{Bmatrix} = \frac{EA\zeta}{\sin(\zeta L)} \begin{bmatrix} \cos(\zeta L) & -1 \\ -1 & \cos(\zeta L) \end{bmatrix} \begin{Bmatrix} v_A \\ v_B \end{Bmatrix} \tag{2.122}$$

or

$$\begin{Bmatrix} F_A \\ F_B \end{Bmatrix} = [\mathbf{K^a}] \begin{Bmatrix} v_A \\ v_B \end{Bmatrix} \tag{2.123}$$

The complete dynamic stiffness matrix of a pile element is given by the combination of Eqs. 2.115 and 2.123, that is

$$\{F\} = [\mathbf{K_p}] \{u\} \tag{2.124}$$

where

$$\begin{aligned}\{F\} &= \{V_{xA} \quad M_{xA} \quad V_{yA} \quad M_{yA} \quad F_A \quad V_{xB} \quad M_{xB} \quad V_{yB} \quad M_{yB} \quad F_B\} \\ \{u\} &= \{u_{xA} \quad \phi_{xA} \quad u_{yA} \quad \phi_{yA} \quad v_A \quad u_{xB} \quad \phi_{xB} \quad u_{yB} \quad \phi_{yB} \quad v_B\}\end{aligned} \tag{2.125}$$

2.3 Dynamic flexibility matrix of clamped-end piles $\mathbf{F_P}$

In order to obtain the terms of F_p associated with the lateral degrees of freedom (u and ϕ), it is necessary to derive the expressions for the lateral displacements caused by a lateral point load in a fixed-end beam.

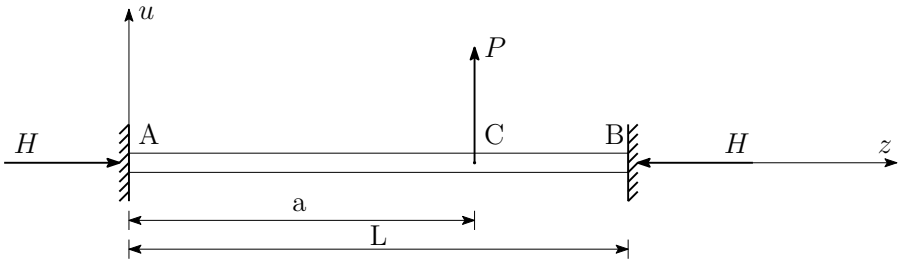

Figure 2.13: Fixed-end beam subjected to a lateral point load P.

For the beam shown in Figure 2.13 subjected to a point force P at $z = a$, Eq. (2.112) can be used to express the displacement of the beam as

$$\begin{cases} u = A_1 \cos(\eta z) + A_2 \sin(\eta z) + A_3 \cosh(\xi z) + A_4 \sinh(\xi z) & 0 \le z \le a \\ u = B_1 \cos(\eta z) + B_2 \sin(\eta z) + B_3 \cosh(\xi z) + B_4 \sinh(\xi z) & a \le z \le L \end{cases} \tag{2.126}$$

where η and ξ were defined in Eq. (2.114), and the unknown constants A_1, A_2, ..., B_3, B_4 are determined by the essential boundary conditions (zero translation and rotation) along with the com-

patibility and equilibrium equations at the point of application of the load. Then,

$$
\begin{aligned}
A_1 &= \frac{P}{EI(\eta^2+\xi^2)T_0}\left[T_3\left(\cosh(\xi a)-\cos(\eta a)\right)+\left(T_1-1\right)\sin\left(\eta a\right)-\left(T_4+\frac{\eta}{\xi}\right)\sinh\left(\xi a\right)\right]\\
A_2 &= -\frac{P}{EI(\eta^2+\xi^2)T_0}\left[\left(T_1-1\right)\cosh\left(\xi a\right)-\left(1+\frac{\xi}{\eta}\,T_4\right)\cosh(\eta a)+T_2\left(\frac{\xi}{\eta}\sin\left(\eta a\right)-\sinh\left(\xi a\right)\right)\right]\\
A_3 &= -A_1\\
A_4 &= -\frac{\eta}{\xi}\,A_2\\
B_1 &= \frac{P}{EI(\eta^2+\xi^2)T_0}\left[T_3\left(\cosh(\xi a)-\cos(\eta a)\right)\left(T_4+\frac{\eta}{\xi}\right)\left(\frac{\xi}{\eta}\sin\left(\eta a\right)-\sinh\left(\xi a\right)\right)\right]\\
B_2 &= -\frac{P}{EI(\eta^2+\xi^2)T_0}\left[\left(T_1-1\right)\left(\cosh\left(\xi a\right)-\cos\left(\eta a\right)\right)+T_2\left(\frac{\xi}{\eta}\sin\left(\eta a\right)-\sinh\left(\xi a\right)\right)\right]\\
B_3 &= -T_1\,B_1-T_3\,B_2\\
B_4 &= T_2\,B_1+T_4\,B_2
\end{aligned}
\tag{2.127}
$$

where

$$
\begin{aligned}
T_1 &= C^{\eta}\,C^{\xi}+\frac{\eta}{\xi}S^{\eta}\,S^{\xi}\\
T_2 &= C^{\eta}\,S^{\xi}+\frac{\eta}{\xi}\,S^{\eta}\,C^{\xi}\\
T_3 &= S^{\eta}\,C^{\xi}-\frac{\eta}{\xi}\,C^{\eta}\,S^{\xi}\\
T_4 &= S^{\eta}\,S^{\xi}-\frac{\eta}{\xi}\,C^{\eta}\,C^{\xi}
\end{aligned}
\tag{2.128}
$$

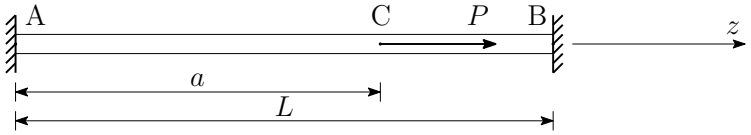

Figure 2.14: Fixed-end beam subjected to a axial point load P.

For a beam in axial vibration (Figure 2.14), the axial displacement in a fixed-end beam sub-

mitted to an axial point load P is given by

$$\begin{cases} v = A_1 \cos(\zeta z) + A_2 \sin(\zeta z) & 0 \le z \le a \\ v = B_1 \cos(\zeta z) + B_2 \sin(\zeta z) & a \le z \le L \end{cases} \tag{2.129}$$

where A_1, A_2, B_1 and B_2 can be determined by the boundary conditions along with the compatibility and equilibrium equations at the point of application of the load. Therefore,

$$\begin{aligned} A_1 &= 0 \\ A_2 &= \frac{P}{EA\zeta}[\cos(\zeta a) - \cot(\zeta L)\,\sin(\zeta a)] \\ B_1 &= \frac{P}{EA\zeta}\,\sin(\zeta a) \\ B_2 &= \frac{-P}{EA\zeta}\,\cot(\zeta L)\,\sin(\zeta a) \end{aligned} \tag{2.130}$$

2.4 Dynamic flexibility matrix of clamped-end piles for harmonic end displacements Ψ

Finally, in order to evaluate the terms of Ψ associated with the lateral degrees of freedom, it is necessary to derive the expression for the lateral displacement of the beam caused by the displacements at the two ends, u_A, u_B, ϕ_A and ϕ_B. This expression can be determined by using Eq. (2.113) along with its derivative to define the end displacements in terms of C_1, C_2, C_3 and C_4. Thus,

$$\begin{aligned} C_1 &= \frac{1}{T_0}\left[\left(1+\frac{\xi}{\eta}T_4\right)u_A + \frac{1}{\eta}T_3\,\phi_A + (C^\eta - C^\xi)\,u_B - \left(\frac{1}{\eta}S^\eta - \frac{1}{\xi}S^\xi\right)\phi_B\right] \\ C_2 &= \frac{1}{T_0}\left[-\frac{\xi}{\eta}T_2\,u_A + \frac{1}{\eta}(1-T_1)\,\phi_A + (S^\eta + \frac{\xi}{\eta}S^\xi)\,u_B + \frac{1}{\eta}(C^\eta - C^\xi)\,\phi_B\right] \\ C_3 &= \frac{1}{T_0}\left[(1-T_1)\,u_A - \frac{1}{\eta}T_3\,\phi_A - (C^\eta - C^\xi)\,u_B + \left(\frac{1}{\eta}S^\eta - \frac{1}{\xi}S^\xi\right)\phi_B\right] \\ C_4 &= \frac{1}{T_0}\left[T_2\,u_A + \left(\frac{1}{\eta}T_4 + \frac{1}{\xi}\right)\phi_A - \left(\frac{\eta}{\xi}S^\eta + S^\xi\right)u_B - \frac{1}{\xi}(C^\eta - C^\xi)\,\phi_B\right] \end{aligned} \tag{2.131}$$

Substituting these constants into Equation (2.113), it is obtained

$$u = C_1' u_A + C_2' \phi_A + C_3' u_B + C_4' \phi_B \tag{2.132}$$

where

$$\begin{aligned}
C_1' &= \frac{1}{T_0}\left[\left(1+\frac{\xi}{\eta}T_4\right)\cos(\eta z) - \frac{\xi}{\eta}T_2\sin(\eta z) + (1-T_1)\cosh(\xi z) + T_2\sinh(\xi z)\right] \\
C_2' &= \frac{1}{T_0}\left[\frac{1}{\eta}T_3\cos(\eta z) + \frac{1}{\eta}(1-T_1)\sin(\eta z) - \frac{1}{\eta}T_3\cosh(\xi z) + \left(\frac{1}{\eta}T_4 + \frac{1}{\xi}\sinh(\xi z)\right)\right] \\
C_3' &= \frac{1}{T_0}\left[(C^\eta - C^\xi)\cos(\eta z) + \left(S^\eta + \frac{\xi}{\eta}S^\xi\right)\sin(\eta z) - (C^\eta - C^\xi)\cosh(\xi z) - \right. \\
&\left.\left(\frac{\eta}{\xi}S^\eta + S^\xi\right)\sinh(\xi z)\right] \\
C_4' &= \left[-\left(\frac{1}{\eta}S^\eta - \frac{1}{\xi}S^\xi\right)\cos(\eta z) + \frac{1}{\eta}(C^\eta - C^\xi)\sin(\eta z) + \left(\frac{1}{\eta}S^\eta - \frac{1}{\xi}S^\xi\right)\cosh(\xi z) - \right. \\
&\left.\frac{1}{\xi}\left(C^\eta - C^\xi\right)\sinh(\xi z)\right]
\end{aligned} \tag{2.133}$$

For lateral vibration, the expressions for C_1 and C_2 of Eq. (2.121) in terms of the end displacements of the beam are

$$\begin{cases} C_1 = v_A \\ C_2 = \dfrac{1}{\sin(\zeta L)}[-\cos(\zeta L)\, v_A + v_B] \end{cases} \tag{2.134}$$

Substituting these constants in Equation 2.120, it is obtained

$$v = C_1^* v_A + C_2^* v_B \tag{2.135}$$

where

$$\begin{aligned}
C_1^* &= \left[\cos(\zeta z) - \frac{1}{\tan(\zeta L)}\sin(\zeta z)\right] \\
C_2^* &= \frac{\sin(\zeta z)}{\sin(\zeta L)}
\end{aligned} \tag{2.136}$$

In order to understand the assemble of the dynamic flexibility matrix Ψ^j, consider the pile j shown in Fig. 2.15.

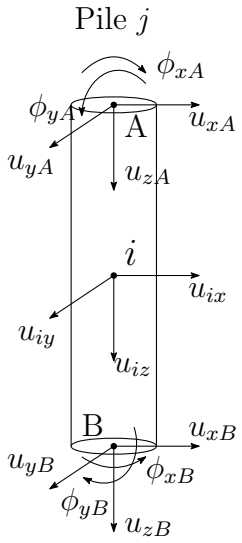

Figure 2.15: Nodal forces at a segment i of a pile j.

This pile contains only one segment, that is, $l = 1$. Therefore, the dimension of the dynamic flexibility matrix Ψ^j is (6×10). The first three rows are related to the node i, whereas the last three ones correspond to the node B.

$$\begin{Bmatrix} u_{ix} \\ u_{iy} \\ u_{iz} \\ u_{Bx} \\ u_{By} \\ u_{Bz} \end{Bmatrix} = \begin{bmatrix} C'_{1x} & C'_{2x} & 0 & 0 & 0 & C'_{3x} & C'_{4x} & 0 & 0 & 0 \\ 0 & 0 & C'_{1y} & C'_{2y} & 0 & 0 & 0 & C'_{3y} & C'_{4y} & 0 \\ 0 & 0 & 0 & 0 & C^*_1 & 0 & 0 & 0 & 0 & C^*_2 \\ 0 & 0 & 0 & 0 & 0 & 1 & 0 & 0 & 0 & 0 \\ 0 & 0 & 0 & 0 & 0 & 0 & 0 & 1 & 0 & 0 \\ 0 & 0 & 0 & 0 & 0 & 0 & 0 & 0 & 0 & 1 \end{bmatrix} \begin{Bmatrix} u_{Ax} \\ \phi_{Ax} \\ u_{Ay} \\ \phi_{Ay} \\ u_{Az} \\ u_{Bx} \\ \phi_{Bx} \\ u_{By} \\ \phi_{By} \\ u_{Bz} \end{Bmatrix} \tag{2.137}$$

2.5 Implementation of dynamic piles code

The presented implementation is based on the model proposed by Kaynia and Kausel (1991) and is written in modern Fortran 90 language. LAPACK linear algebra routines provided by Intel Math Kernel Library (Intel MKL) are used whenever available.

As discussed before, the terms of the flexibility matrix of the soil F_s require an appropriated scheme of integration. For this reason, two numerical routines from QUADPACK library, based on adaptive gaussian quadrature, were chosen for evaluation of each region: DQAGE and DQAGIE (Piessens et al., 2012). The first routine calculates an approximation to a given definite integral and is applied for integration of the first region. A small damping is inserted in the constitutive properties of the soil (Christensen, 2012) in order to make the singularities more easily integrable. The second estimates an integral over a semi-infinite or infinite interval and is applied into the second region. Both routines give double precision results. Since each term of the influence matrix $\mathbf{F_s}$ is independent of each other, they can be computed simultaneously. OpenMP routines for parallel CPU execution were incorporated in the implementation for this purpose. Also, the present implementation can model the pile-soil interface by two kinds of contact conditions: the relaxed and the fully-bonded contact condition. For more details about these conditions, please refer to section 4.4. In order to obtain consistent results in the solution of the final algebraic system of Eq. (2.11), the Intel MKL PARDISO package was used (Schenk and Gartner, 2004).

2.5.1 Validation

In order to verify the presented implementation, the results of the vertical impedance of a 2×2 pile group connected by a rigid base (Fig. 2.16) are compared with those reported by Kaynia and Kausel (1991). The model consists of a homogeneous viscoelastic layer of soil, with depth $H = 75d_p$, resting on a rigid bedrock, with Poisson's ratio $\nu_s = 0.25$ and material damping $\eta_s = 0.03$, in which d_p is the diameter of the piles and the subindices s and p stand for the soil and the pile, respectively. The distance between adjacent piles is denoted by s, and $a_0 = \omega d_p/C_s$ is the nondimensional frequency, in which C_s is the largest shear wave velocity of the soil profile. The piles are characterized by length $(l_p/d_p) = 37.5$, Poisson's ratio $\nu_p = 0.25$, and elastic modulus E_p such that $(\pi\mu_s l_p^2/E_p A) = 1$, where A is the cross-sectional area of the pile, and $s/d_p = 5$.

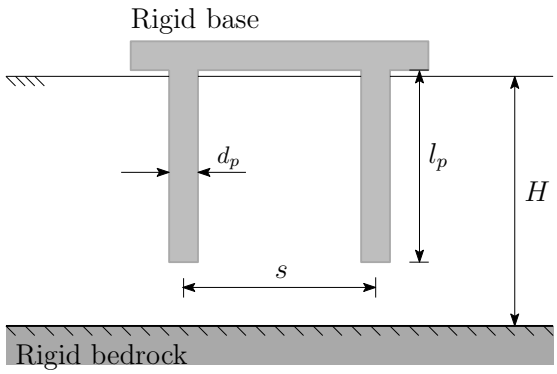

Figure 2.16: Validation using a 2×2 pile grid.

The impedance is a complex quantity, which can be defined as

$$K_{ii} = k_{ii} + ia_0 c_{ii} \tag{2.138}$$

where k_{ii} and c_{ii} are the stiffness and damping of the pile foundation, respectively, in the horizontal or vertical directions ($i = x,z$).

Figure 2.17 compares the vertical impedances K_{zz} obtained by present and Kaynia and Kausel (1991) (Reference) implementations. The superscripts G and S represent values associated with pile groups and single piles, and N is the number of piles in the group. The stiffness and damping values are normalized with respect to the static stiffness. The results show good agreement between the two implementations.

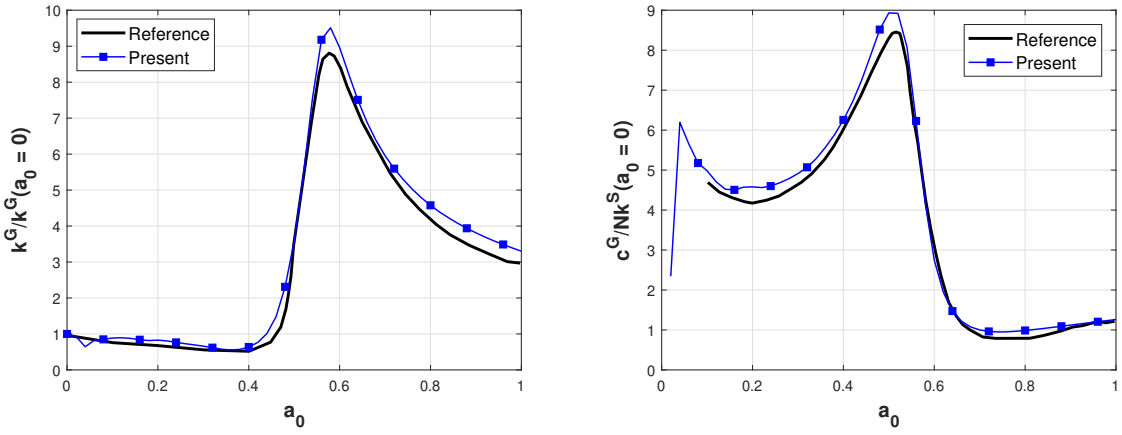

Figure 2.17: Impedance of a 2×2 pile grid connected by a rigid cap.

3 Model of a surface structure

This chapter presents a model for an arbitrarily-shaped structure supported by a pile group. Initially, the dynamic stiffness matrix of the structure is derived by the Finite Element Method. Then, the coupling between this matrix and the impedance matrix of the pile group is presented.

3.1 Modeling of structure by FEM

The structure is modeled by a linear elastic 8-noded hexahedral finite element consisting of three degrees of freedom per node (Fig. 3.1).

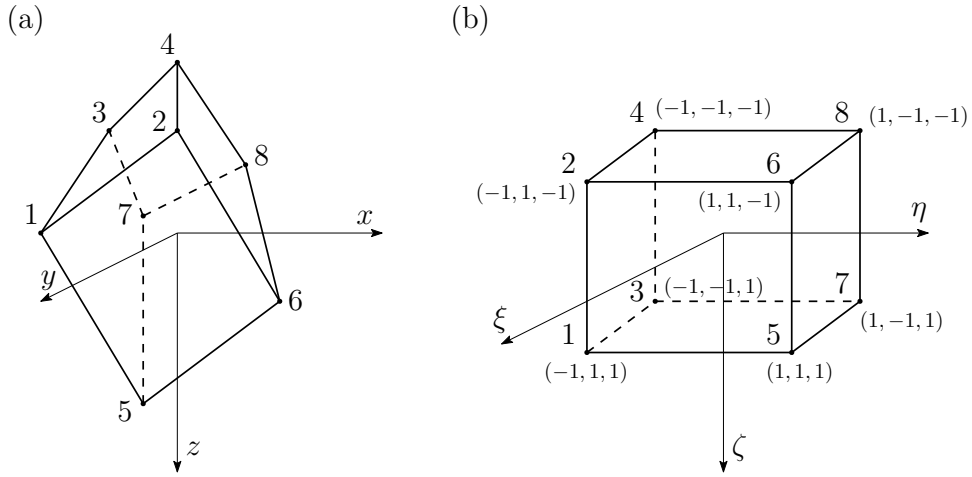

Figure 3.1: 8-noded hexahedral finite element in the (a) physical and (b) natural domain

The stiffness and mass matrices of this element are given by

$$\begin{aligned} \mathbf{K}_e &= \int_{V_e} \mathbf{B}^T\,\mathbf{D}\,\mathbf{B}\,dV = \int_{-1}^{1}\int_{-1}^{1}\int_{-1}^{1} \mathbf{B}^T\,\mathbf{D}\,\mathbf{B}\,\det(\mathbf{J})\,d\xi\,d\eta\,d\zeta \\ \mathbf{M}_e &= \int_{V_e} \rho\,\mathbf{N}^T\,\mathbf{N}\,\det(\mathbf{J})\,d\xi\,d\eta\,d\zeta \end{aligned} \tag{3.1}$$

in which V_e is the volume of the element, $\mathbf{D}$ is the constitutive matrix of the element, $\mathbf{N}$ and $\mathbf{B}$ are the vector of shape functions and the matrix of its derivatives, respectively, and $\mathbf{J}$ is the Jacobian of transformation. For more details about these terms, please refer to Cook (2007). The

inertial stiffness matrix of the structure for a given circular frequency ω is

$$\mathbf{K}_I = \mathbf{K}_G - \omega^2 \, \mathbf{M}_G \tag{3.2}$$

where $\mathbf{K}_G$ and $\mathbf{M}_G$ are the global stiffness and mass matrices assembled from $\mathbf{K}_e$ and $\mathbf{M}_e$.

3.2 Coupling scheme

In order to derive a scheme for coupling the structure and the pile group, consider a fixed-end bar composed by three homogeneous segments and two loads applied at B and D (Figure 3.2a). A free-body diagram of a general element j with elastic modulus E_j, cross-sectional area A_j and length L_j is represented in Fig. 3.2b.

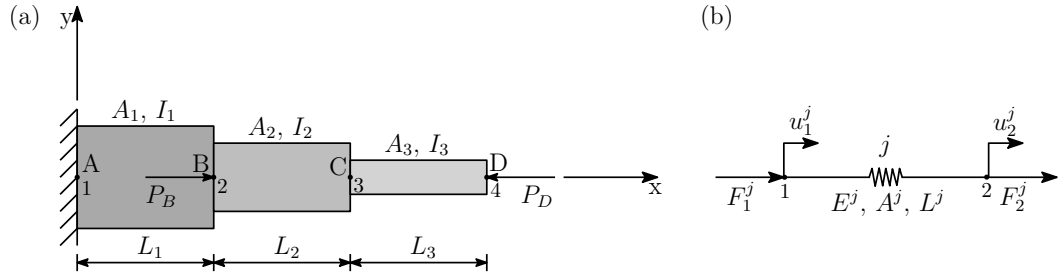

Figure 3.2: Physical problem and free-body diagram of a fixed-end bar

The forces resulting from imposing a displacement at each end of this element are given by

$$F_{11} = F_{21} = \frac{A_j E_j}{L_j} u_1 \quad \text{and} \quad F_{12} = F_{22} = \frac{A_j E_j}{L_j} u_2 \tag{3.3}$$

where F_{ik} is the force at node i (i = 1,2) associated with displacement at node k (k = 1,2). A superposition of these forces allows writing Eq. (3.3) in matrix form. It is considered that forces and displacements are positive in the same direction. Thus,

$$\begin{bmatrix} F_{11} & -F_{12} \\ -F_{21} & F_{22} \end{bmatrix} \begin{Bmatrix} 1 \\ 1 \end{Bmatrix} = \begin{Bmatrix} F_1 \\ F_2 \end{Bmatrix} \quad \text{or} \quad \frac{A_j E_j}{L_j} \begin{bmatrix} 1 & -1 \\ -1 & 1 \end{bmatrix} \begin{Bmatrix} u_1 \\ u_2 \end{Bmatrix} = \begin{Bmatrix} F_1 \\ F_2 \end{Bmatrix} \tag{3.4}$$

in which F_1 and F_2 are the resultant forces at nodes 1 and 2, respectively. Expressing Eq. (3.4) in

terms of a general element j results in

$$\begin{bmatrix} k_j & -k_j \\ -k_j & k_j \end{bmatrix} \begin{Bmatrix} u_1^j \\ u_2^j \end{Bmatrix} = \begin{Bmatrix} F_1^j \\ F_2^j \end{Bmatrix} \quad \text{or} \quad [\mathbf{K}_e]\{\mathbf{u}\} = \{\mathbf{F}\} \tag{3.5}$$

where $\mathbf{K}_e$ is the stiffness matrix of the element, and $\{\mathbf{u}\}$ and $\{\mathbf{F}\}$ are the displacement and load vectors of the element. Now, consider the interface containing node 2 as shown in Fig. 3.3.

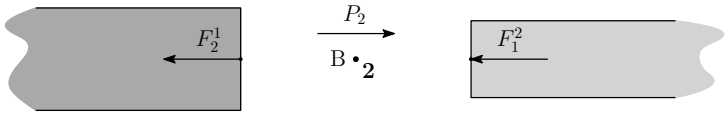

Figure 3.3: Interface B of the fixed-end bar

The equilibrium equation in this interface is given by

$$-\left(F_2^1 + F_1^2\right) + P_2 = 0 \tag{3.6}$$

Substituting Eq. (3.5) into Eq. (3.6) gives

$$P_2 = \left(-k_1 u_1^1 + k_1 u_2^1 + k_2 u_1^2 - k_2 u_2^2\right) \tag{3.7}$$

From kinematic compatibility at this interface, it is known that $u_2 = u_2^1 = u_1^2$. Then,

$$P_2 = \left(-k_1 u_1^1 + (k_1 + k_2) u_2 - k_2 u_2^2\right) \tag{3.8}$$

The same procedure can be applied to other interfaces. The resulting expressions can be written in matrix form, that is

$$\begin{Bmatrix} P_1 \\ P_2 \\ P_3 \\ P_4 \end{Bmatrix} = \begin{bmatrix} k_1 & -k_1 & 0 & 0 \\ -k_1 & k_1 + k_2 & -k_2 & 0 \\ 0 & -k_2 & k_2 + k_3 & -k_3 \\ 0 & 0 & -k_3 & k_3 \end{bmatrix} \begin{Bmatrix} u_1 \\ u_2 \\ u_3 \\ u_4 \end{Bmatrix} \quad \text{or} \quad [\mathbf{K}_G]\{\mathbf{u}_G\} = \{\mathbf{P}_G\} \tag{3.9}$$

where $\mathbf{K}_G$ is the global stiffness matrix and $\{\mathbf{u}_G\}$ and $\{\mathbf{P}_G\}$ are the global displacement and load vectors.

For a dynamic analysis, the mass and inertia properties of the system are considered and included into the mass matrix $\mathbf{M}_G$. The global mass matrix $\mathbf{M}_G$ is obtained by the assembly of

element mass matrices $\mathbf{M}_e$, in the same way that the global stiffness matrix is formed. Thus, the stiffness matrix for such analysis is given by

$$\bar{\mathbf{K}}_G = \mathbf{K}_G - \omega^2 \mathbf{M}_G \tag{3.10}$$

Extending the coupling scheme for the case of piled structures, the discretization of the structure must ensure that there is a node localized at each pile head of the pile group, as shown in Fig. 3.4. The coupling between the pile group and the structure is obtained by establishing kinematic compatibility and equilibrium at the node-pile head interfaces.

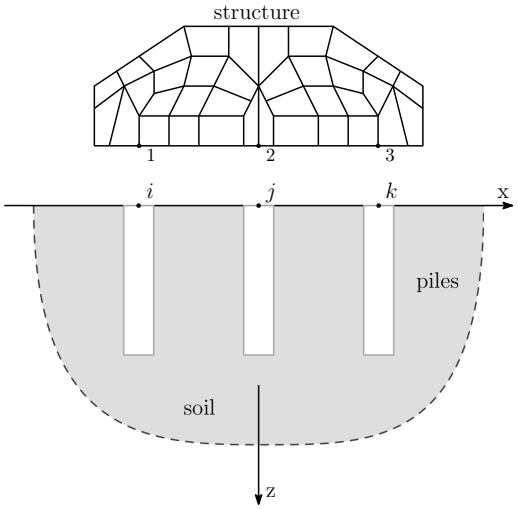

Figure 3.4: Scheme of discretization of a piled structure

In order to illustrate the coupling scheme, consider an arbitrary pile shown in Figure 3.5. P_x^s, P_z^s, P_x^p and P_z^p are the loads in x and z directions at the nodes corresponding to the structure and the pile head, respectively. u_x^s, u_z^s, u_x^p and u_z^p are the displacements due to these loads. F_x and F_z are the external loads that may be applied at the interface.

In a similar procedure developed for the bar, the relation between the nodal displacements and forces in the piled structure is $[\bar{\mathbf{K}}_G]\{\mathbf{u}_G\} = \{\mathbf{P}_G\}$, in which

$$\begin{aligned} \{\mathbf{P}_G\} &= \begin{Bmatrix} P_x^1 & P_y^1 & P_z^1 & P_x^2 & P_y^2 & P_z^2 & \dots & P_x^N & P_y^N & P_z^N \end{Bmatrix} \\ \{\mathbf{u}_G\} &= \begin{Bmatrix} u_x^1 & u_y^1 & u_z^1 & u_x^2 & u_y^2 & u_z^2 & \dots & u_x^N & u_y^N & u_z^N \end{Bmatrix} \end{aligned} \tag{3.11}$$

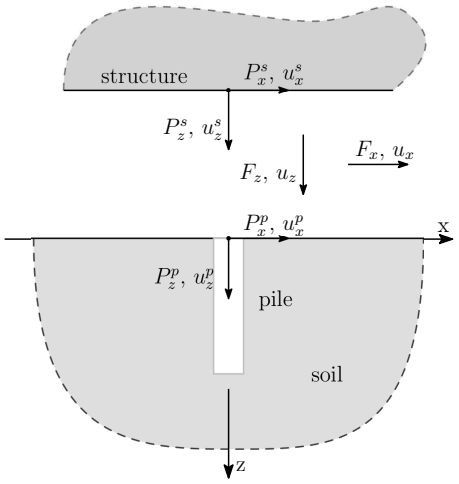

Figure 3.5: Interface and external loads and displacements

where P_i^n and u_i^n are the loads and displacements of node n of the piled structure ($n = 1,N$) in the i-direction ($i = x,y,z$). $[\bar{\mathbf{K}}_G]$ is given by

$$[\bar{\mathbf{K}}_G] = \begin{bmatrix} K_{11}^s & \dots & K_{1n}^s & \dots & K_{1m}^s & \dots & K_{1N}^s \\ \vdots & \ddots & \vdots & & \vdots & & \vdots \\ K_{n1}^s & \dots & K_{nn}^s + K_{ii}^p & \dots & K_{nm}^s + K_{ij}^p & \dots & K_{nN}^s \\ \vdots & & \vdots & \ddots & \vdots & & \vdots \\ K_{m1}^s & \dots & K_{mn}^s + K_{ji}^p & \dots & K_{mm}^s + K_{jj}^p & \dots & K_{mN}^s \\ \vdots & & \vdots & & \vdots & \ddots & \vdots \\ K_{N1}^s & \dots & K_{Nn}^s & \dots & K_{Nm}^s & \dots & K_{NN}^s \end{bmatrix} \tag{3.12}$$

Each term K is a 3×3 matrix that contains the stiffness terms in the x-, y- and z- direction. Sub-indices n and m indicate the nodes that the pile heads i and j are connected to the structure, respectively. For instance, K_{ij}^p is a 3×3 stiffness matrix that relates the displacements of pile head j ($u_x^j,\ u_y^j,\ u_z^j$) due to loads applied on the pile head i ($P_x^i,\ P_y^i,\ P_z^i$). In the same manner, K_{nm}^s is a 3×3 stiffness matrix that relates the displacements of node m of the structure ($u_x^m,\ u_y^m,\ u_z^m$) due to loads applied on the node n ($P_x^n,\ P_y^n,\ P_z^n$).

In order to validate the coupling scheme, consider a 2×2 pile group connected to an elastic surface block (Fig. 3.6).

The results are compared to the reference presented in Fig. 2.17. The block is modeled with

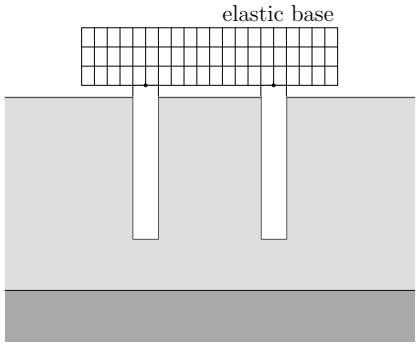

Figure 3.6: 2×2 pile group connected by an elastic surface block

8464 elements. Since this scheme allows for an elastic block to be considered, the effect of variations of the elasticity modulus of the block in the response of the system can be analysed. Figure 3.7 shows the convergence to the rigid plate case obtained by increasing the structure's elasticity modulus.

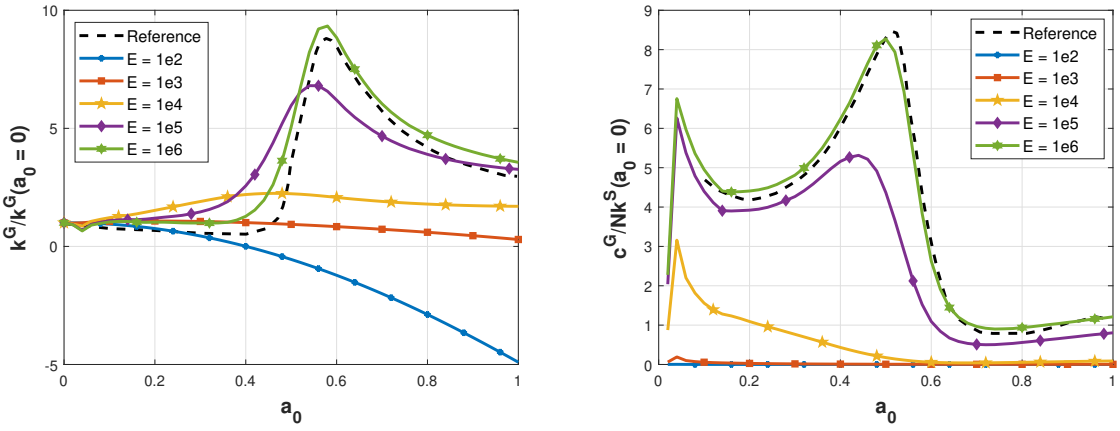

Figure 3.7: Stiffness and damping of the structure-foundation system for different elasticity moduli of the surface block

4 Numerical results

This chapter shows original numerical results of the response of pile groups obtained with the present implementation for various numbers of piles, layers and frequencies of excitation. The precision and the computational cost of the results are analysed. Techniques to reduce of computational cost are investigated. Lastly, strain simulations of the flexible structure are analysed.

4.1 Number of piles

The limiting number of piles is not defined explicitly in both the reference Kaynia and Kausel (1991) implementation and the present implementation. For the reference, it depends on the number of different pile-to-pile distances (the maximum distances allowed is 50), whereas for the present one, it depends on the physical memory of the hardware. In a square grid of $c \times c$ piles containing $N = c^2$ piles, the reference implementation is limited to 5×5, $N = 25$ piles (Fig. 4.1).

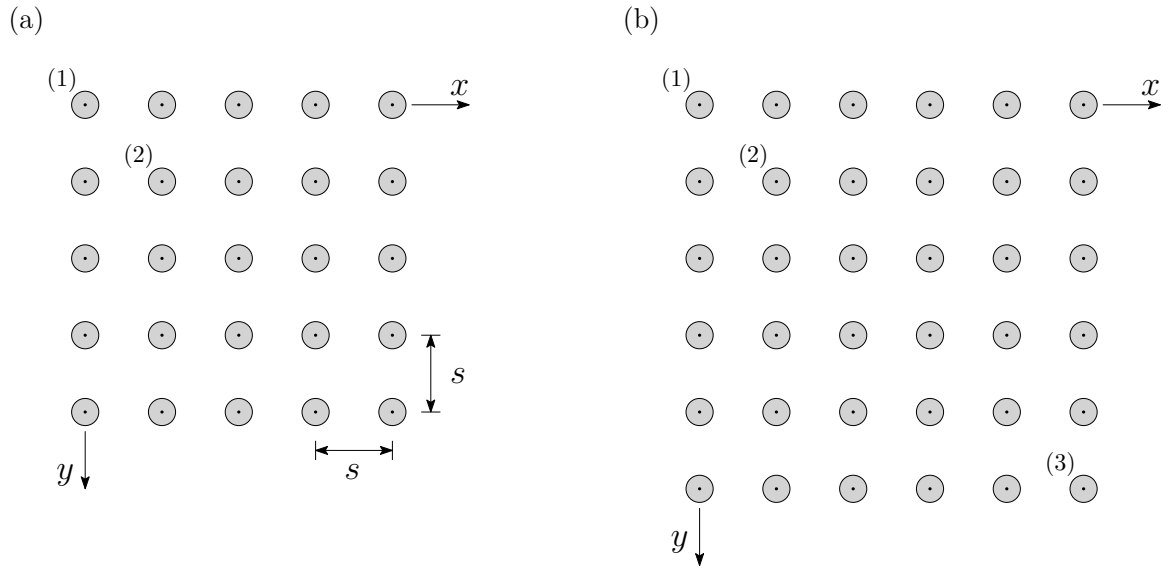

Figure 4.1: Pile grids used in this section, with (a) $N = 25$ and (b) $N = 36$ piles

Figure 4.2 shows a comparison of this case with the present implementation. These results consider piles of length $l_p/d_p = 1$, $E_p/E_s = 100$, $\rho_p/\rho_s = 2$, $\nu_p = \nu_s$, and pile-to-pile distance $s/d_p = 5$, within a homogeneous, isotropic soil. Pile (1) is under vertical excitation with frequency a_0, and the figures show the resulting normalized vertical displacement $u_z^* = u_z/u_z(a_0 = 0)$ of pile

(2). The results show that the present and reference implementations agree for this case.

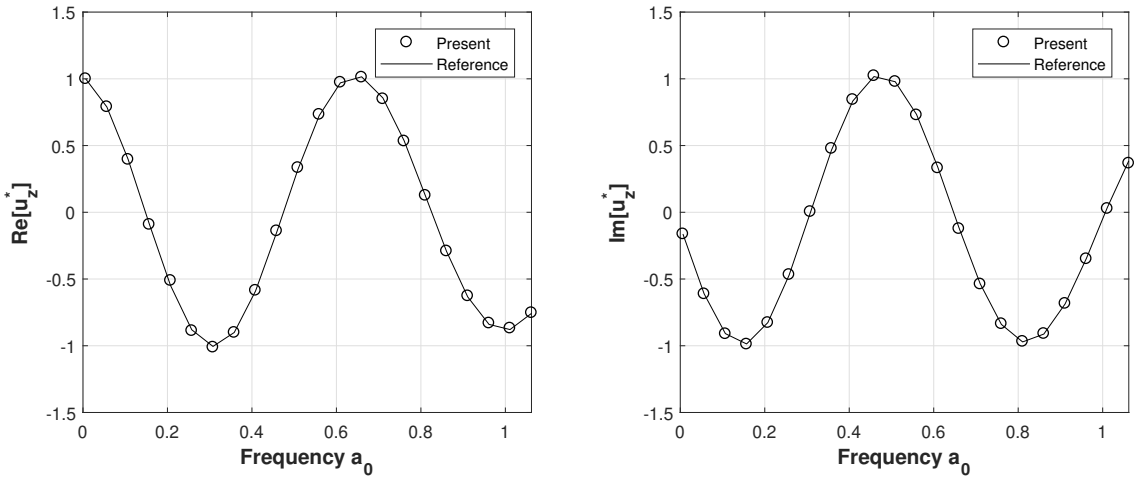

Figure 4.2: Vertical displacement of pile (2) within a 5×5 pile grid.

Figure 4.3 extends the previous analysis for a 6×6 grid of $N = 36$ piles (Fig. 4.1b). The reference implementation is unable to model this problem.

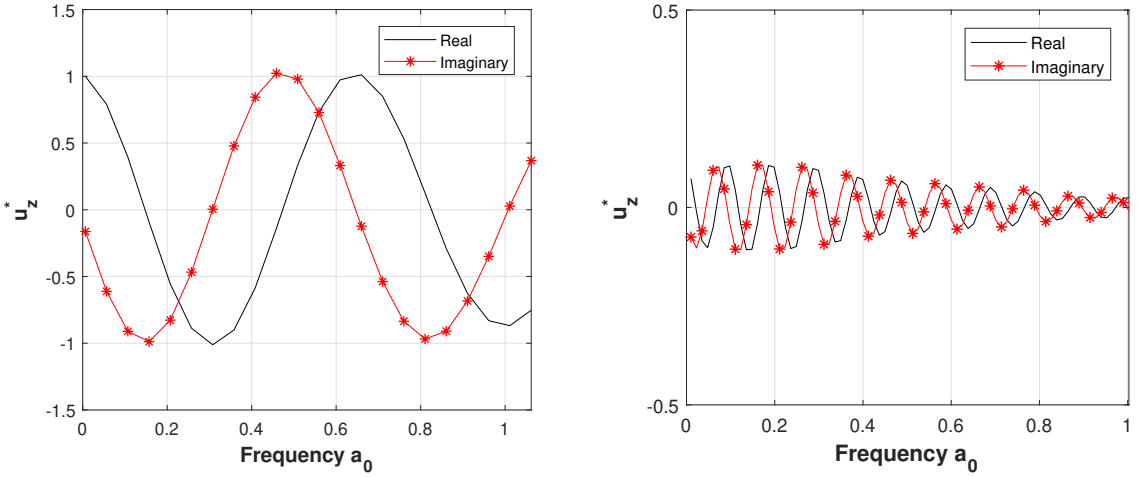

Figure 4.3: Vertical displacements of pile (2) and pile (3) within a 6×6 pile grid.

4.2 Number of layers

The number of layers and layer thickness depend on the geological features of soil. Although the reference implementation provides a limit of thirty layers for the soil medium, this is a good approximation for the pile-soil interaction effects for most practical applications (Barros et al., 2018), as well as cases of heterogeneous layered soils with up to thirty different layers. However, for cases in which the material properties of the soil vary continuously with depth, this quantity could not be enough to represent very well such effects.

In order to analyze such case, Figure 4.4 illustrates the Gibson's soil (Jin, 2014), in which the shear modulus μ_s of the soil varies linearly with depth. Figure 4.4b shows that a small number of layers may not be able to represent the continuous variation of μ_s. It has been shown that an accurate representation of Gibson's soils may require each soil layer to have depth $h_p/d_p \leq 0.25$ (Labaki et al., 2018).

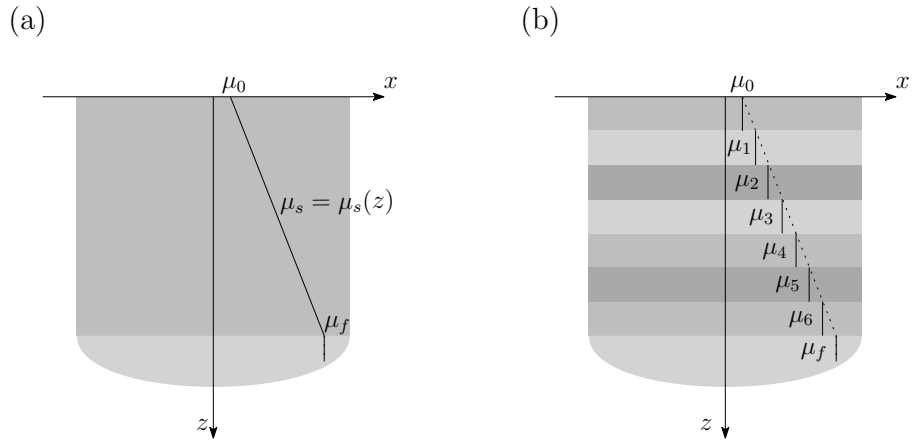

Figure 4.4: Soil with continuously varying shear modulus versus discrete heterogeneous layers.

For further investigation, the problem of a pile of length l_p embedded in Gibson's soil with $\mu_s = \mu_0(1 + mz)$ is considered. The soil is represented by M homogeneous layers with shear modulus $\mu_i = \mu_0(1 + m \cdot i/Ml_p)$, $i = 1,M$. In this study, $l_p/d_p = 20$, $\mu_p/\mu_0 = 100$, $\rho_p/\rho_s = 2$, $\nu_p = \nu_s$, and $m = 2$.

Figure 4.5 compares the normalized displacement $u_z^* = u_z/u_z(M = 10)$ of the pile head for different numbers of layers and $a_0 = 0.5$. The results show that the response tends monotonically to

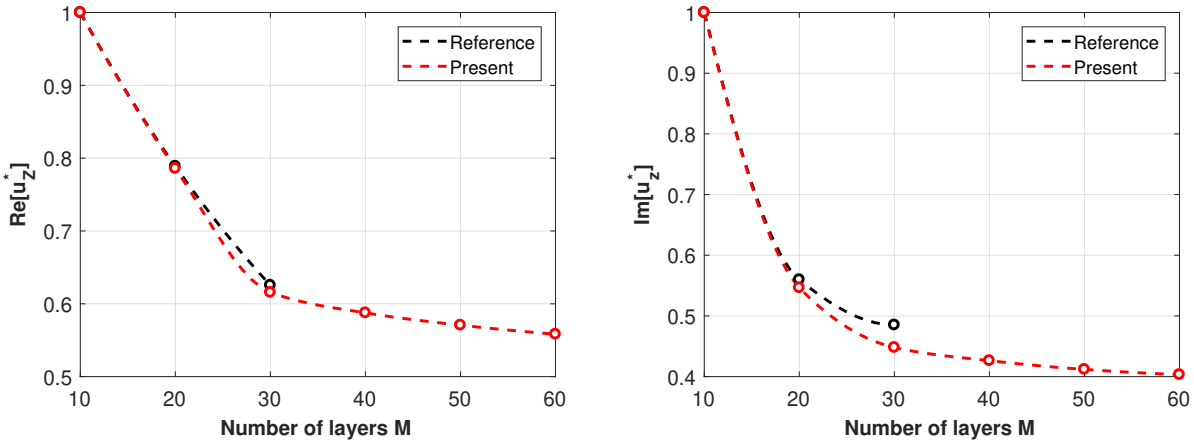

Figure 4.5: Convergence of pile response with numbers of layers.

the value that corresponds to the perfectly continuous variation of shear modulus of the soil, which is significantly different from one obtained by the reference implementation. This conclusion may differ for different values of l_p and m.

The present implementation can be used to model weathered crusts as well, in which the shear modulus of the soil first decreases up to a certain shallow depth, after which it increases, as well as any other soil model in which shear modulus and mass density vary with depth.

4.3 Reach in frequency

The frequency of excitation applied in dynamic SSI problems is usually within the seismic range ($a_0 \leq 1$). However, if a transient impulse response of a system through an Fast-Fourier Transform (FFT) scheme is required, the implementation must be robust enough to obtain the response of this system for high frequencies (Adolph et al., 2001).

Figure 4.6 shows the transient vertical displacement and velocity of the pile tip under a vertical impulse load applied at the pile head, for the case that $l_p/d_p = 20$. Pressure (P) and shear (S) wave fronts travel through the pile from the pile head and reach the pile tip at times $t_i = l_p/c_i$, $i = P,S$, in which $C_p^2 = (\lambda_p + 2\mu_p)/\rho_p$ and $C_s^2 = \mu_p/\rho_p$, λ_p is the Lamé constant of the pile. In Figure 4.6, the dashed red lines represent the time that the pressure and shear waves are expected to reach the pile tip. The results show accurate predictions.

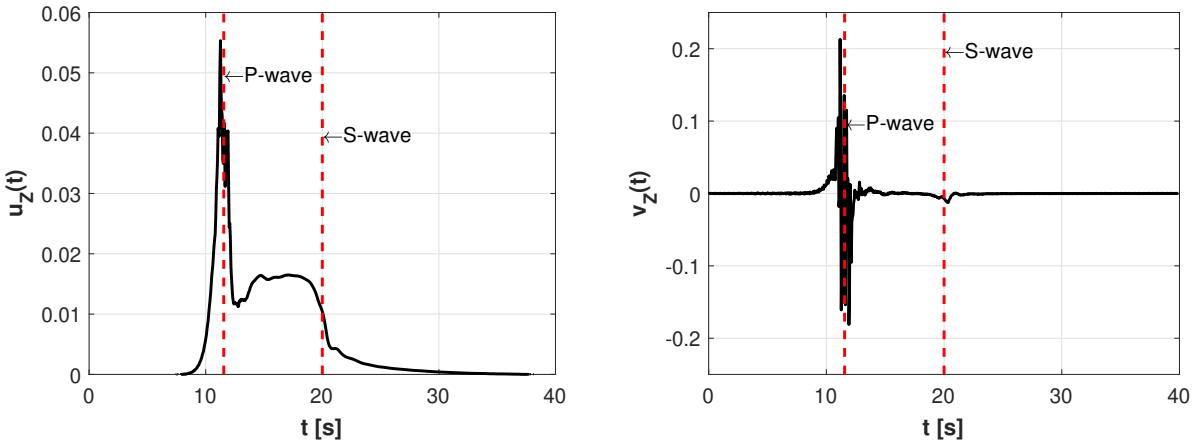

Figure 4.6: Impulse response of pile tip.

The transient response of pile groups not only enables additional information about the system, such as a visualization of wavefronts, but can be used together with convolution schemes to yield the response of the system to any other type of excitation (Labaki et al., 2013).

The discretization in the time domain of the impulse response is directly proportional to the number of values of frequency for which the original time-harmonic signal is computed. The reference implementation is limited to one hundred frequencies, whereas the present one can compute responses for an unlimited number of frequencies. However, this limitation can be overcome by merely executing the reference implementation multiple times. A more significant improvement in this aspect concerns the quality of the numerical integration of the influence terms of F_s. The focus of the present implementation is in the efficiency of the code, but modern integration schemes that are being implemented into it are already producing more accurate integrations than the reference implementation.

4.4 Bonding condition

The contact between the pile and the soil can be described by two kinds of boundary conditions. In the relaxed bonding condition, kinematic compatibility and equilibrium at the pile-soil interface are enforced in the loading direction only. In the fully-bonded contact condition, kinematic compatibility and equilibrium are prescribed in all directions. The fully-bonded contact condition demands a significantly larger amount of influence functions to be computed, which is expected to

increase the computational cost of the solution considerably. Computing the influence functions is typically the most computationally expensive task in a boundary element model such as the present one (Labaki et al., 2011). It has been shown that the difference between the two bonding conditions is negligible for the cases of surface plates (Labaki et al., 2014, 2018) and single piles (Barros, 2006; Barros et al., 2018). In this section, both boundary conditions are investigated for the case of a pile group.

For such investigation, the dynamic response of pile groups under time-harmonic external excitations of circular frequency ω are computed considering both relaxed and fully-coupled contact conditions. The results are presented in terms of the normalized displacement $u_i^*(a_0) = u_i(a_0)/u_i(a_0 = 0)$, $i = x,z$ and normalized frequency $a_0^2 = \omega^2\rho_s/\mu_s$. The soil medium is a viscoelastic, homogeneous, isotropic half-space. Throughout the study, the head of a pile i is subjected to vertical or horizontal loads p_z or p_x, and the effect of this load is measured at the head of pile j in terms of its vertical and horizontal displacements u_z and u_x. In Figures 4.8 to 4.13, continuous and dashed lines represent respectively the real and imaginary displacement for a coupled contact condition whereas discrete markers represent the same quantities for an uncoupled contact condition.

4.4.1 Pile group configurations

Consider three different pile group configurations and the effect of coupling conditions in each case as shown in Fig. 4.7. The first case considers a single pile, the second considers two piles along the $x-$axis, and the third considers four piles in a square grid centered at the origin of the coordinate system. In all cases, $l_p/d_p = 10$, $E_p/E_s = 100$, $\rho_p/\rho_s = 2$, and $s/d_p = 5$.

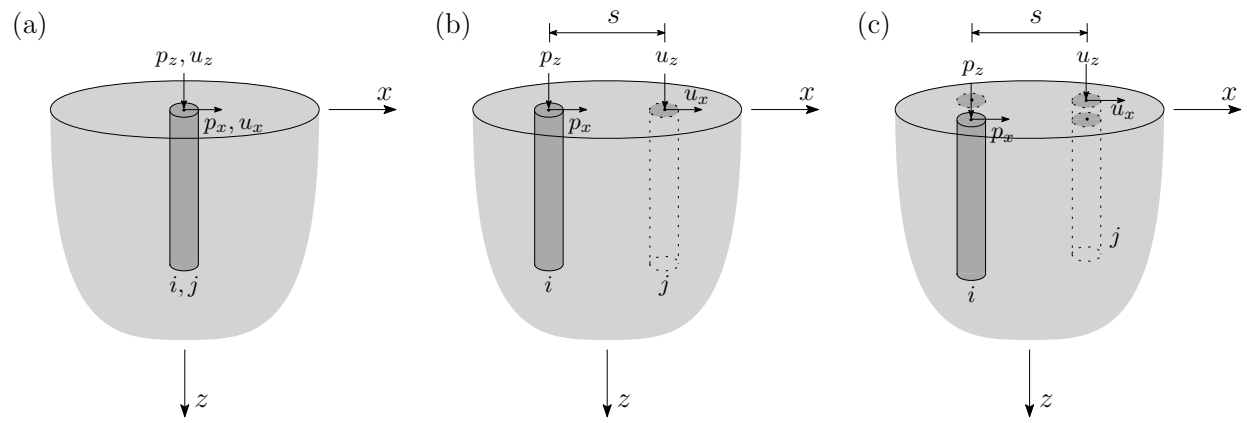

Figure 4.7: Pile group configurations for (a) one, (b) two, and (c) four piles under vertical and horizontal loads

Figures 4.8 to 4.10 show the vertical and horizontal displacements of pile j due to vertical loads applied to pile i in each of the three configurations shown in Fig. 4.7. Note that the figures without markers indicate that the uncoupled contact condition is not applicable for the case. Moreover, due to the symmetry of the single pile case, no horizontal displacements result from the vertical loading case and vice-versa.

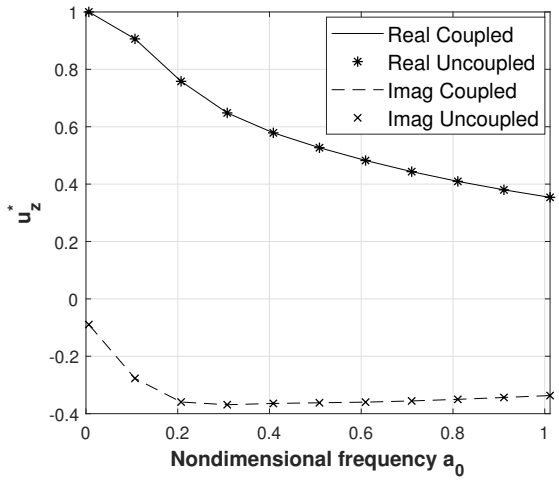

Figure 4.8: Real and imaginary part of u_z^* for a single pile.

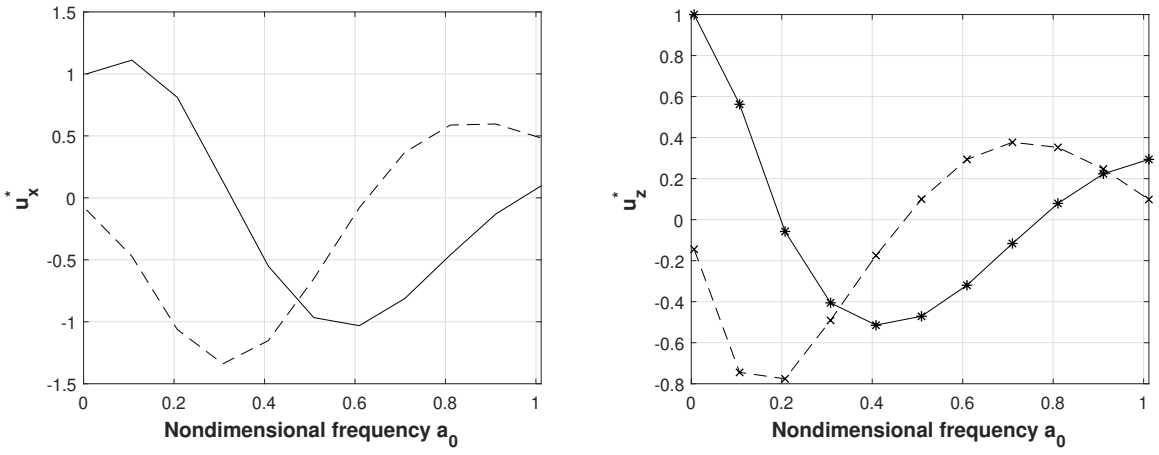

Figure 4.9: Real and imaginary part of u_x^* and u_z^* for a group of two piles.

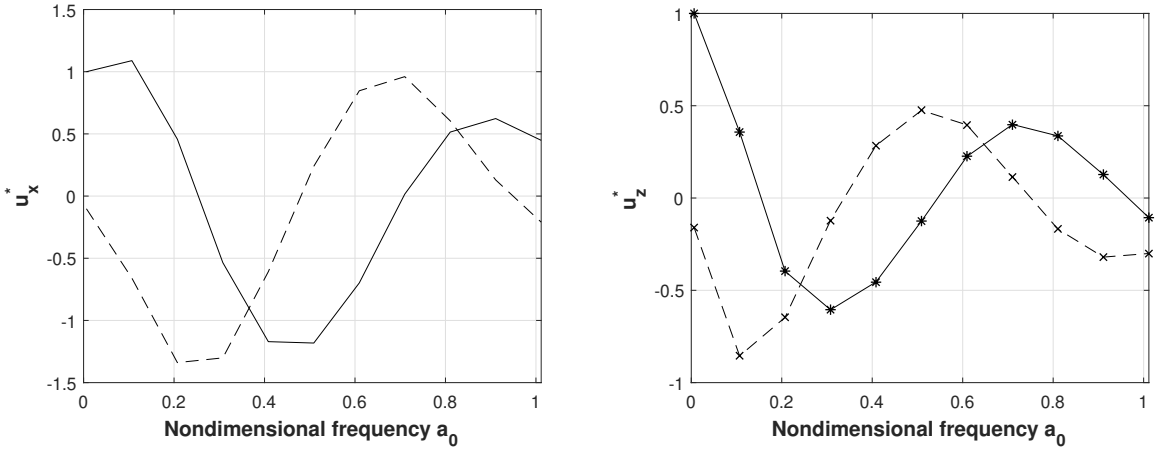

Figure 4.10: Real and imaginary part of u_x^* and u_z^* for a group of four piles.

Analogously, Figs. 4.11 to 4.13 show the corresponding results for the case of horizontal loads applied to pile i in the three configurations.

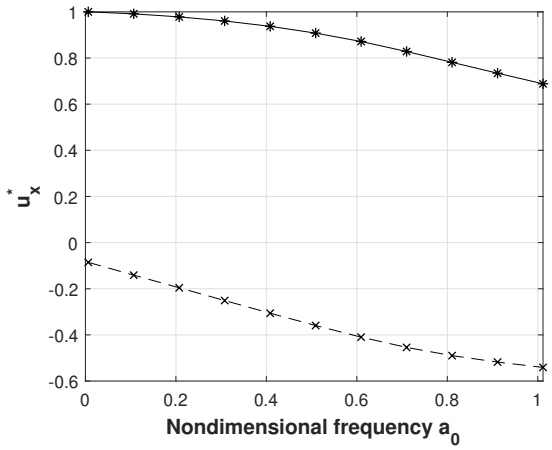

Figure 4.11: Real and imaginary part of u_x^* for a single pile.

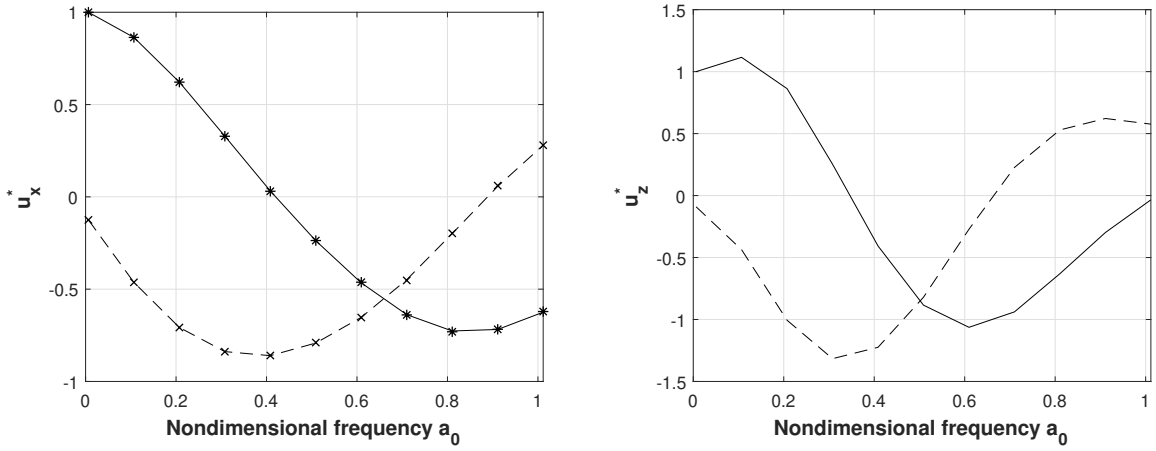

Figure 4.12: Real and imaginary part of u_x^* and u_z^* for a group of two piles.

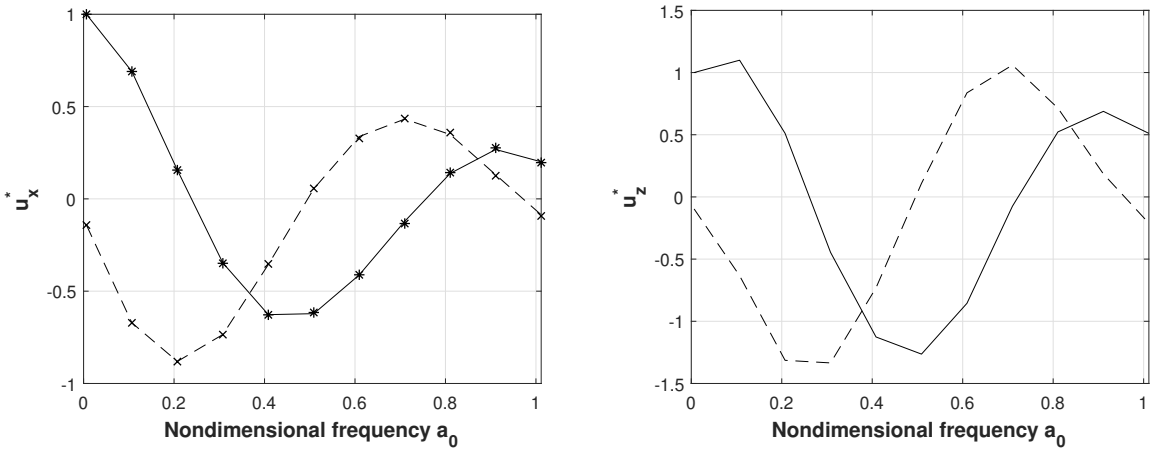

Figure 4.13: Real and imaginary part of u_x^* and u_z^* for a group of four piles.

These results indicate that there is no difference between the response of the piles in different group configurations when either relaxed or fully-bonded coupling conditions are used.

4.4.2 Pile parameters

This section presents a study on the influence of bonding conditions for different pile parameters. The parameters considered are the most relevant in pile group problems, such as pile length l_p, stiffness E_p, and mass density ρ_p, as well as distance s between piles. For the next results, a system of two piles is considered (Fig. 4.7b).

Figures 4.14 and 4.15 show the effect of bonding conditions (continuous lines versus discrete markers) for three different pile stiffnesses and for nondimensional frequencies of $a_0 = 0.5$ and $a_0 = 1$. In these results, $l_p/d_p = 10$ and $\rho_p/\rho_s = 2$. Figure 4.14 presents the horizontal normalized displacements $u^*_{xz} = u_{xz}(s)/u_{xz}(s = 2)$ due to vertical loads resulting from the coupled condition (C) for a stiffness rate ($E' = E_p/E_s$) of $E' = 1$, $E' = 10$ and $E' = 100$.

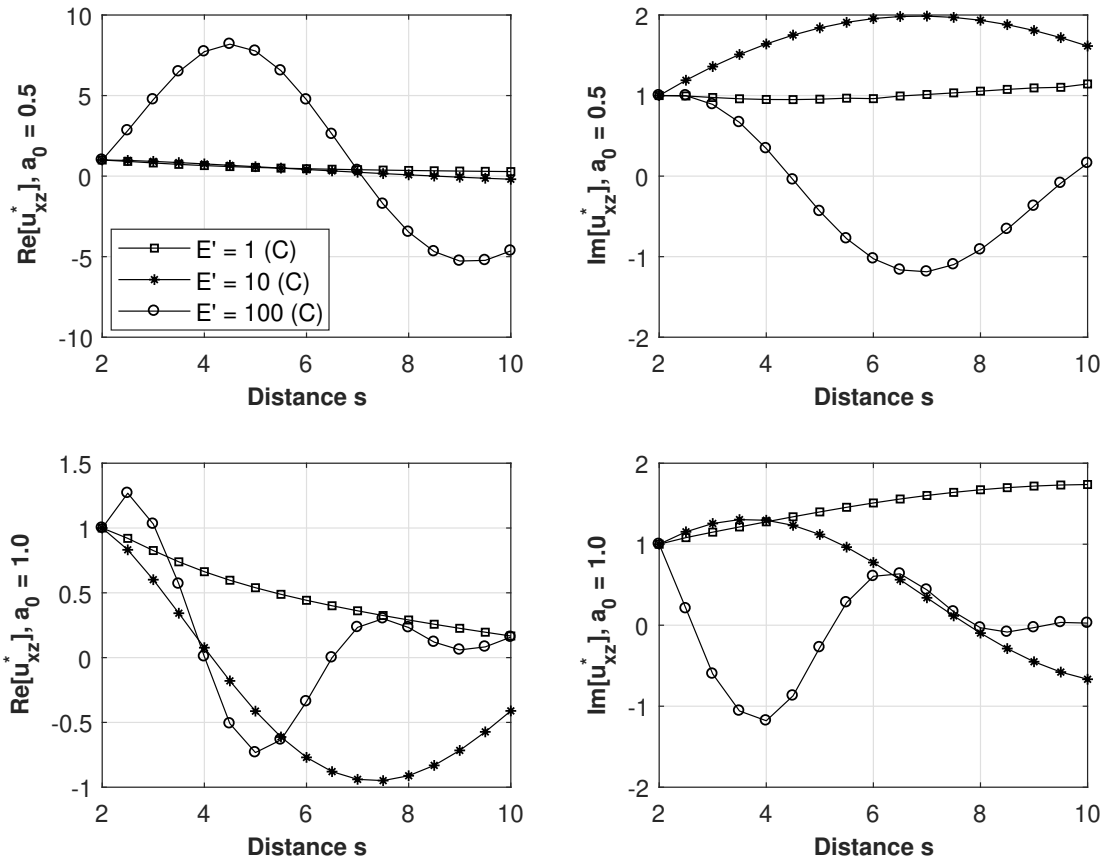

Figure 4.14: Horizontal response of second pile for different elastic moduli.

Figure 4.15 shows vertical normalized displacements $u^*_{zz} = u_{zz}(s)/u_{zz}(s = 2)$ due to vertical loads resulting from the coupled (C) and uncoupled (U) conditions for the same stiffness rates.

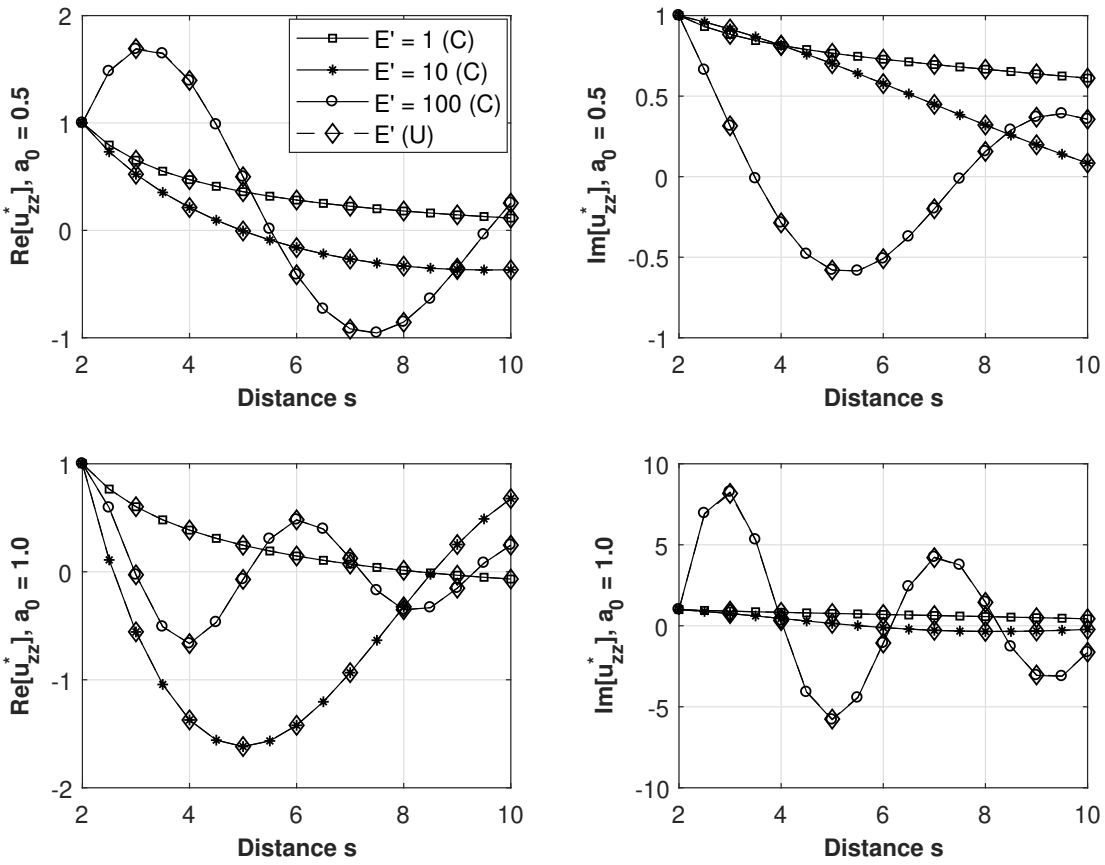

Figure 4.15: Vertical response of second pile for different elastic moduli.

Analogously, Figs. 4.16 and 4.17 consider three different pile mass densities for the same nondimensional frequencies. In these results, $l_p/d_p = 10$ and $E_p/E_s = 100$. Figure 4.16 presents the horizontal normalized displacements $u^*_{xz} = u_{xz}(s)/u_{xz}(s = 2)$ due to vertical loads resulting from the coupled condition (C) for a mass density rate ($\rho' = \rho_p/\rho_s$) of $\rho' = 1$, $\rho' = 10$ and $\rho' = 100$.

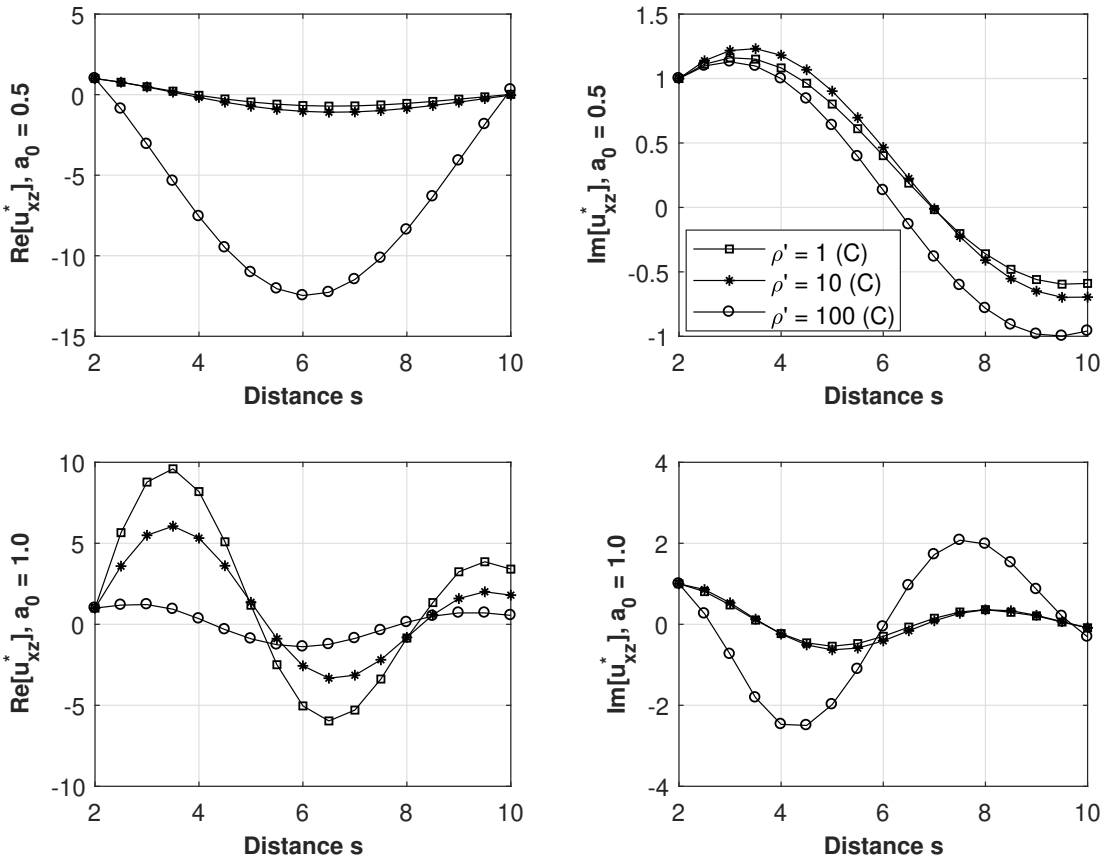

Figure 4.16: Horizontal response from second pile for different mass densities.

Figure 4.17 shows vertical normalized displacements $u^*_{zz} = u_{zz}(s)/u_{zz}(s=2)$ due to vertical loads resulting from the coupled (C) and uncoupled (U) conditions for the same mass density rates.

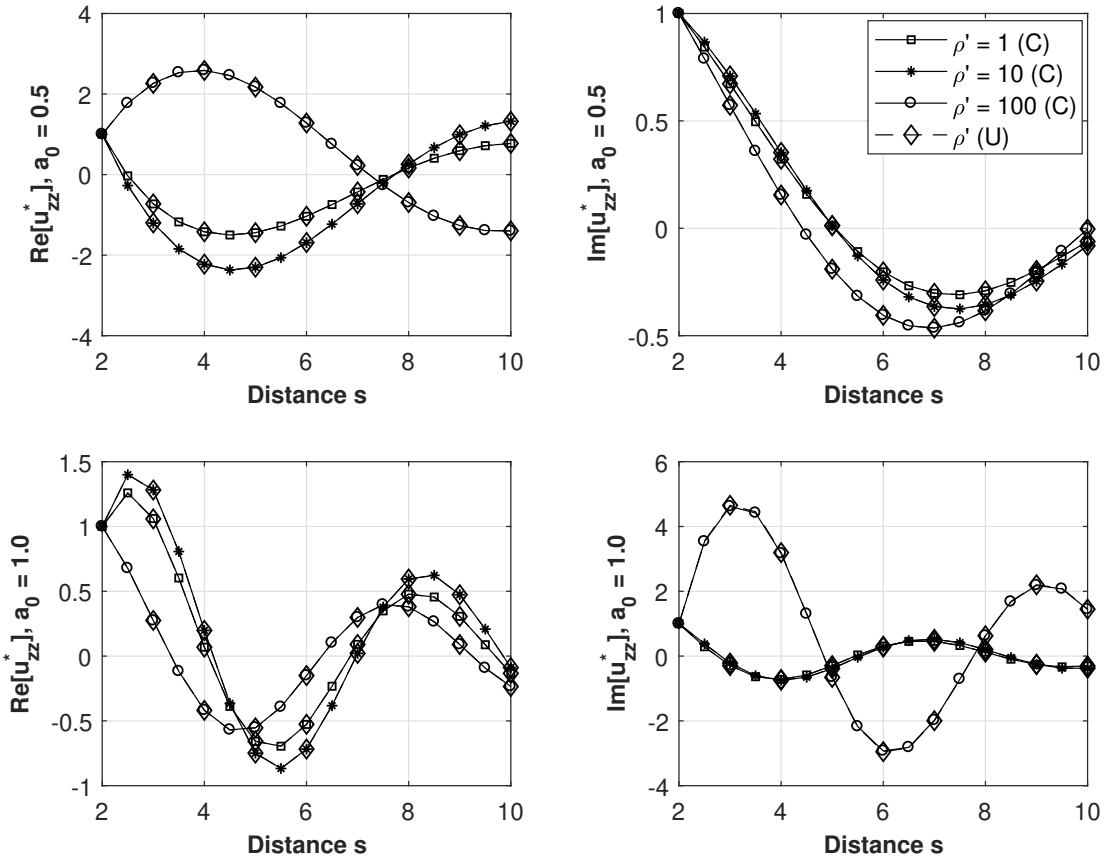

Figure 4.17: Vertical response from second pile for different mass densities.

Finally, Figs. 4.18 and 4.19 consider three different pile lengths. In these results, $\rho_p/\rho_s = 2$ and $E_p/E_s = 100$. Figure 4.18 presents the horizontal normalized displacements $u^*_{xz} = u_{xz}(s)/u_{xz}(s = 2)$ due to vertical loads resulting from the coupled condition (C) for a length-diameter relation ($l' = l_p/d_p$) of $l' = 5$, $l' = 10$ and $l' = 20$.

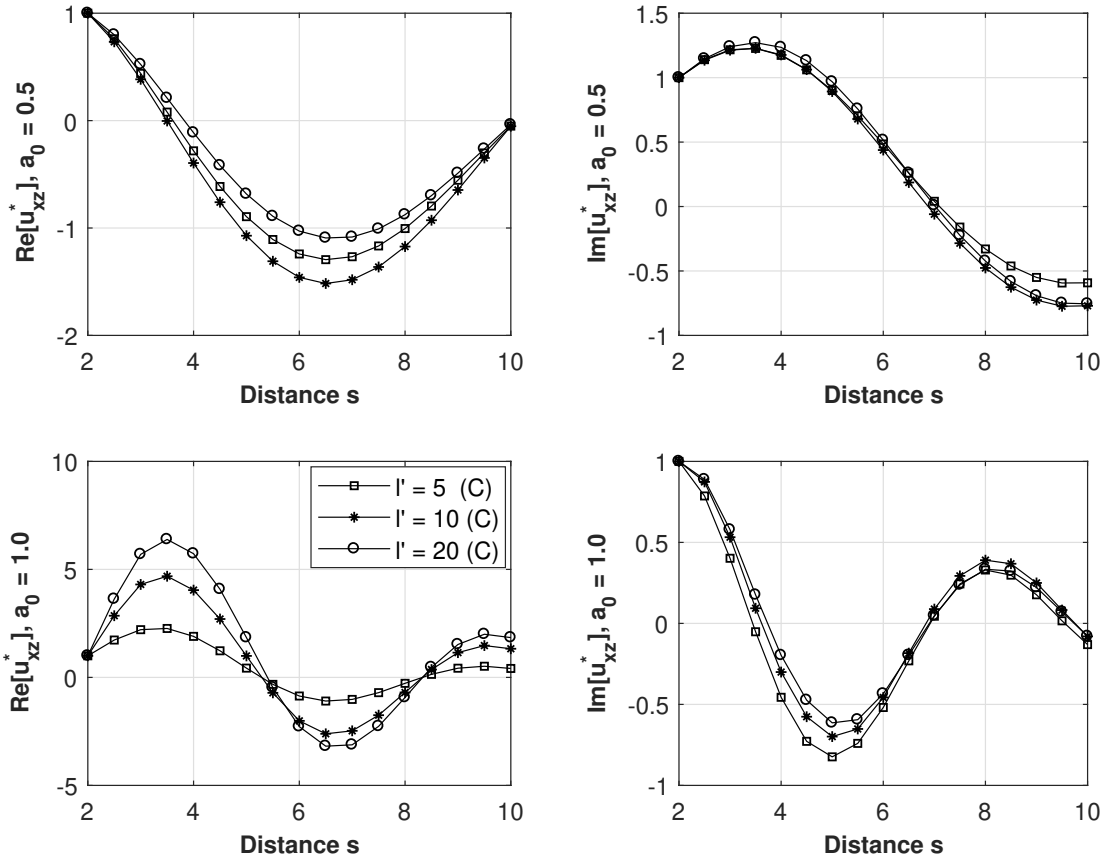

Figure 4.18: Horizontal response from second pile for different lenghts.

Figure 4.19 shows vertical normalized displacements $u^*_{zz} = u_{zz}(s)/u_{zz}(s = 2)$ due to vertical loads resulting from the coupled (C) and uncoupled (U) conditions for the same relations.

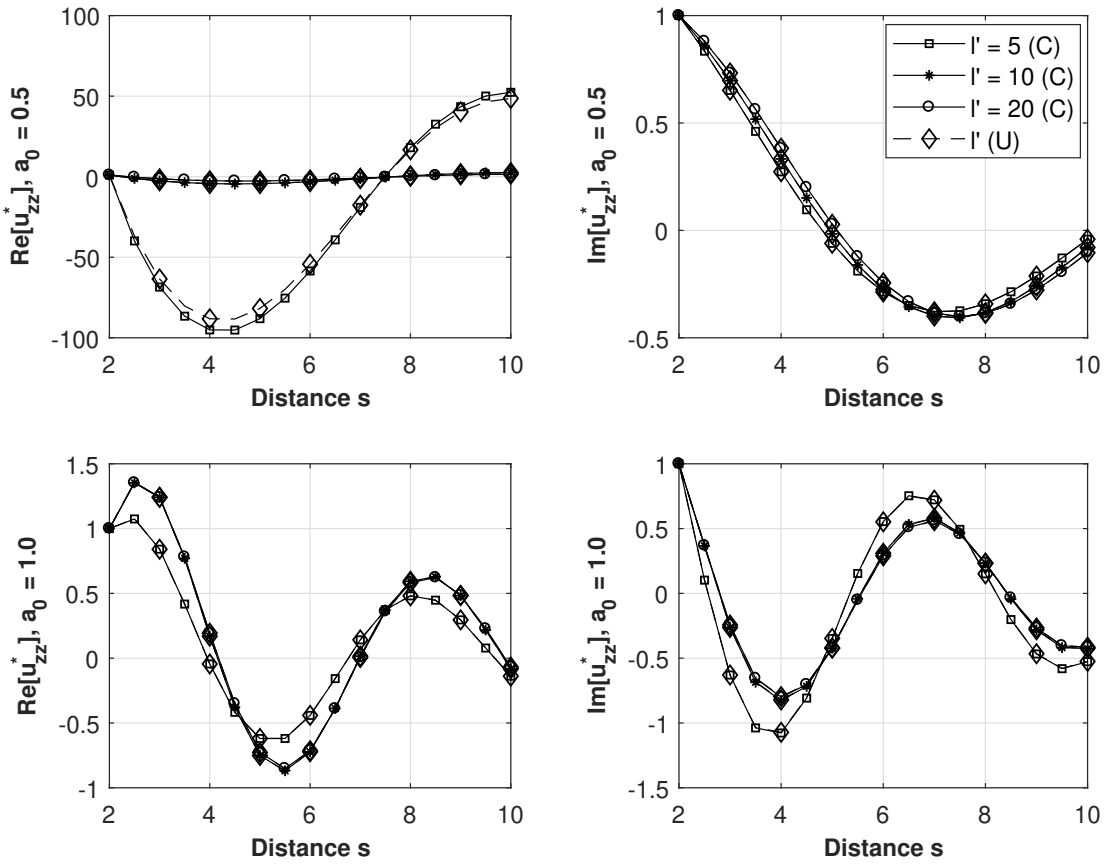

Figure 4.19: Vertical response from second pile for different lenghts.

Once again, the results in this section indicate that the response of the pile group is similar for both coupling conditions. This indicates that one may choose to model a pile group with the coupling condition with the lowest computational cost, without loss of physical consistency of the model.

4.5 Numerical precision and computational cost

All the variables used in the present implementation are declared as double precision value, as well as all routines compute the variables with this data type. This is an improvement over the reference implementation's single precision computations. Tables 4.1 and 4.2 show an example of results obtained with the two implementations. Table 4.1 represents the vertical displacement of pile head for the Gibson's soil problem considered in Fig. 4.5, whereas Tab. 4.2 shows the same quantity of pile tip. Double-precision computing is particularly important for highly detailed analyses such as that in Fig. 4.6.

Table 4.1: Non-normalized vertical displacement of the pile head in single and double precision

l	$u_z^{ref}(z=0)$	$u_z^{present}(z=0)$
10	2.51E-02 - 2.68E-03i	2.533091964329770E-002 - 2.708101515209209E-003i
20	1.98E-02 - 1.50E-03i	1.990730241373737E-002 - 1.479873021093602E-003i
30	1.57E-02 - 1.30E-03i	1.559579569852306E-002 -1.213291072226059E-003i

Table 4.2: Non-normalized vertical displacement of the pile tip in single and double precision

l	$u_z^{ref}(z=l_p)$	$u_z^{present}(z=l_p)$
10	-1.27E-04 - 3.94E-05i	-1.185645004647512E-004 - 4.581495383222291E-005i
20	-9.82E-05 - 8.56E-05i	-1.072022351902839E-004 - 8.123614967273680E-005i
30	- 9.45E-05 - 9.86E-05i	-1.018054846131397E-004 - 8.813936429117812E-005i

The number of integrals of the flexibility matrix of the soil F_s to be evaluated in a given execution of the present code varies with the number of elements l used in the pile discretization (equal to the number of layers in the system) and the number of piles in the group. Even considering a case of a single pile, the computational cost due to the integration of the terms of such matrix does not vary linearly with $\sqrt{l}$. This is due to the fact that integrals may be more or less difficult to evaluate depending on the parameters of the problem. Table 4.3 shows the computational cost to solve the case of a single pile discretized by $l = 1,...,20$ elements. The table breaks down the total elapsed time Δt_{total} into the time spent to fill matrix F_s, Δt_{F_s}, and the time spent to solve the final linear system in Eq. (2.11), $\Delta t_{Eq.(2.11)}$. Table 4.3 shows that the time spent to solve the linear system in Eq. (2.11) is negligible.

Table 4.3: Computational cost of single pile with different numbers of elements M in seconds.

l	Δt_{total}	$\Delta t_{\mathbf{F}_s}$	$\Delta t_{Eq.(2.11)}$	l	Δt_{total}	$\Delta t_{\mathbf{F}_s}$	$\Delta t_{Eq.(2.11)}$
1	1.377	1.277	0.100	11	78.523	78.423	0.100
2	2.677	2.576	0.101	12	100.698	100.589	0.109
3	5.099	4.998	0.101	13	121.613	121.504	0.109
4	7.941	7.841	0.100	14	148.737	148.627	0.110
5	14.183	14.081	0.100	15	169.977	169.852	0.109
6	18.187	18.087	0.100	16	212.661	212.558	0.101
7	26.879	26.778	0.101	17	251.851	251.749	0.101
8	37.606	37.504	0.100	18	307.368	307.265	0.101
9	47.754	47.652	0.100	19	333.696	333.585	0.111
10	61.757	61.648	0.100	20	412.041	411.939	0.100

Additionally, Table 4.4 shows the time spent to solve the cases of $N = 1,...,6$ piles of $l = 20$ elements each. Again, the time spent to fill matrix F_s has a significant contribution in computational cost.

Table 4.4: Computational cost of a pile group with N piles in seconds.

N	Δt	$\Delta t_{Eq.(2)}$
1	412.041	0.100
2	1185.538	0.109
3	1942.404	0.102
4	2950.984	0.105
5	3045.961	0.140
6	3990.635	0.125

Figure 4.20 presents the contribution of the increase in the number of layers and piles in the computational cost. The first graph of Fig. 4.20 shows that the cost to solve this problem increases slightly more than linearly with the number of integrals to be solved, whereas the second one shows that the addition of new piles with the same geometry and properties increases the computational cost of the solution in an irregular manner.

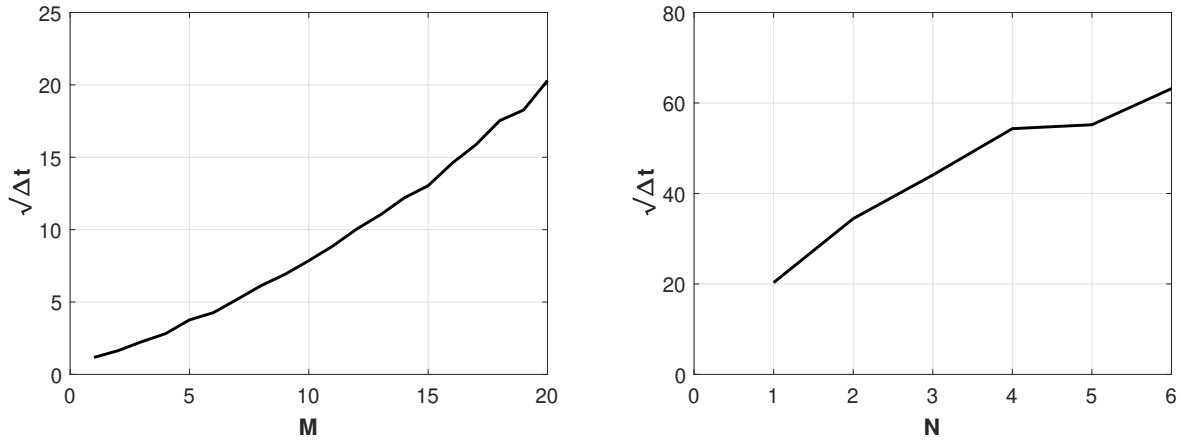

Figure 4.20: Total computational cost to solve a single pile with M elements and N piles with $l = 20$ elements.

This section also compares the computational cost of fully-coupled and relaxed bonding conditions for pile groups. For the analysis of computational cost, the three pile group configurations shown in Fig. 4.21 are considered. In all cases, all piles have length $l_p/d_p = 10$, $E_p/E_s = 100$, $\rho_p/\rho_s = 2$, and are discretized by $l = 20$ elements.

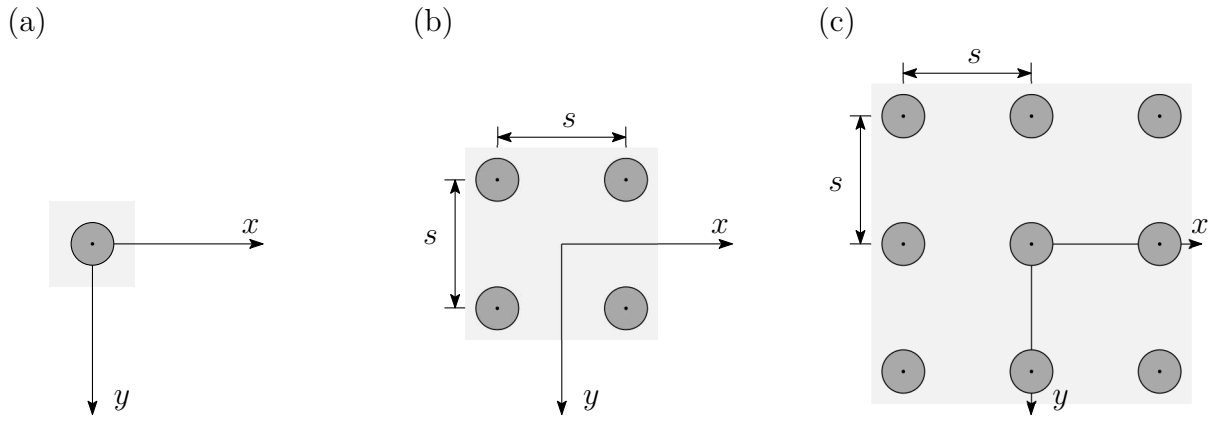

Figure 4.21: Pile group configurations for (a) one, (b) four, and (c) nine piles

Table 4.5 shows the time spent to execute both bonding condition models in these configurations. In summary, for the one-, four-, and nine-pile grid problems, the fully-bonded condition has shown to be from 16 to 18 per cent more expensive than its relaxed condition counterpart.

Table 4.5: Computational cost of a pile group in seconds.

Pile group	Relaxed bonding	Full bonding
1	24	28
2	87	101
9	212	252

4.6 Strain simulation of the flexible structure

The physical consistency of the proposed coupling scheme can be evaluated by a strain simulation. In this section, the shear and volumetric strains of the flexible structure supported by the 2×2 pile group presented in Fig. 3.6 are investigated. In both analyses, the results are obtained for uniformly distributed vertical and horizontal loads of nondimensional frequencies $a_0 = 0.5$ and $a_0 = 1.0$.

4.6.1 Strain field due to vertical loads

For the pile groups shown in Figures 4.22 and 4.26, the structure is a block with sides $l_b = 5d_p$ and height $h_b = 0.5d_p$ composed by 1024 finite elements. The subscripts st and p represent the quantities associated with the structure and the piles, respectively. In these results, $\nu_{st}/\nu_p = 1$, $\rho_{st}/\rho_p = 1$ and $E_{st}/E_p = 1.78$. The nodes corresponding to pile heads are located at each inferior vertex of the structure. A distributed vertical load is applied at the superior face of this structure.

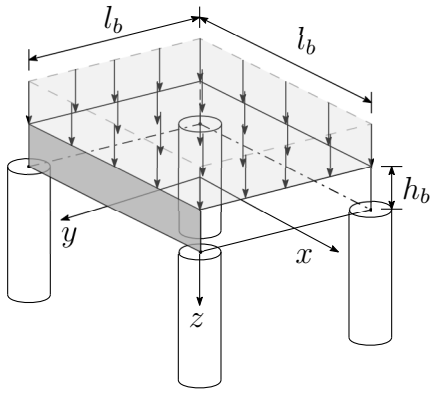

Figure 4.22: Frontal plane of a structure submitted to a vertical load

In order to verify the consistency of the deformation, the results of the piled structure are compared with the ones of the case shown in Fig. 4.23, which consists of a structure supported at the same nodes of pile heads in Fig. 4.22.

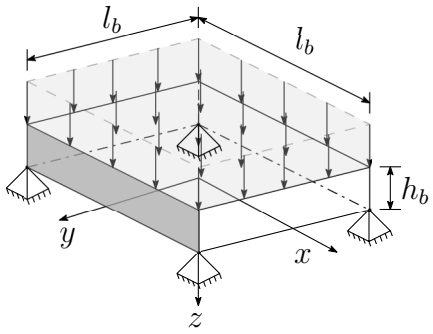

Figure 4.23: Frontal plane of a supported structure submitted to a vertical load

Figures 4.24 and 4.25 show the harmonic deformation of the structure. In Fig. 4.24, the color map represents the shear strain field over time, whereas in Fig. 4.25, one represents the volumetric strain field over time. The dashed grid represents the deformation of the frontal face of the supported structure. Notice the good agreement between the two models.

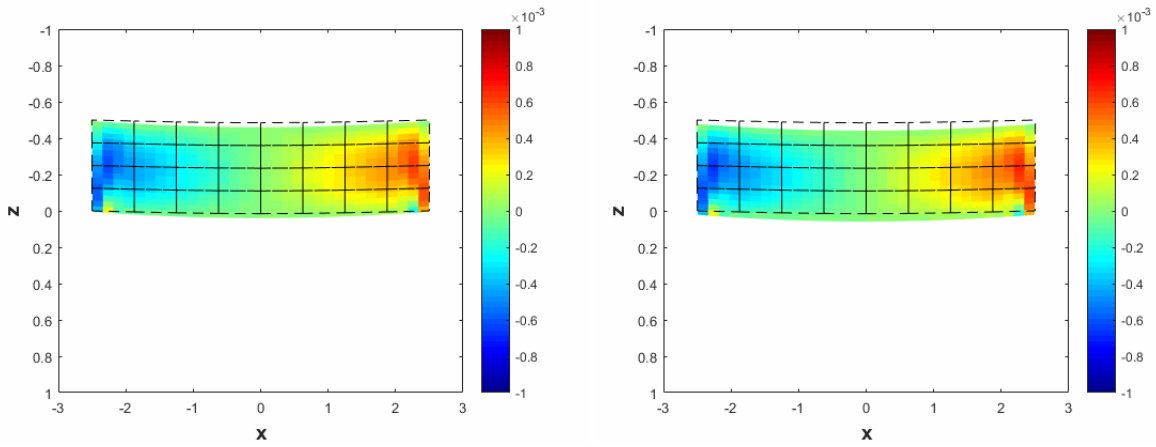

Figure 4.24: Shear strain at the frontal face due to a vertical load for nondimensional frequency $a_0 = 0.5$ and $a_0 = 1.0$

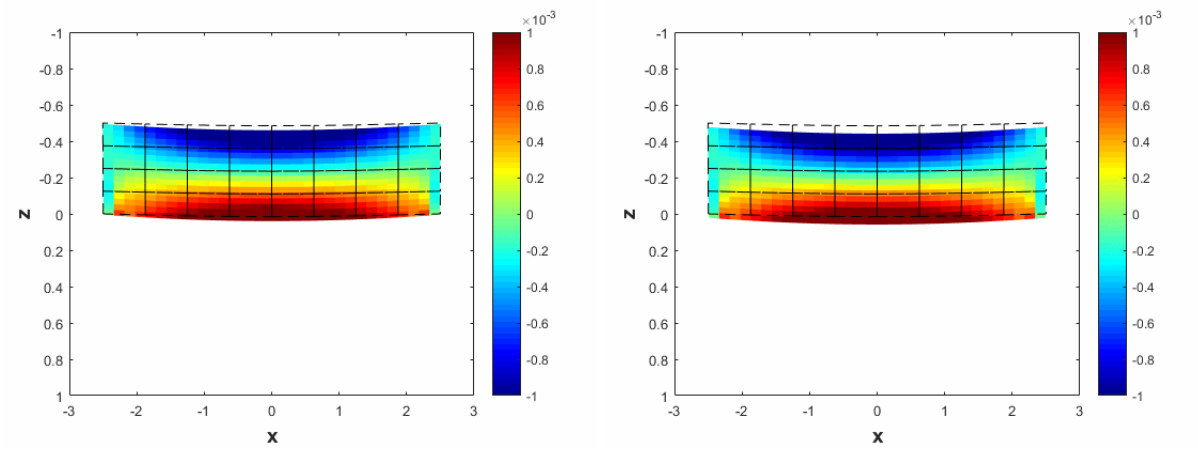

Figure 4.25: Volumetric strain at the frontal face due to a vertical load for nondimensional frequency $a_0 = 0.5$ and $a_0 = 1.0$

For the central face as shown in Figure 4.26, Fig. 4.27 and 4.28 present the color map of the shear and volumetric strains, respectively.

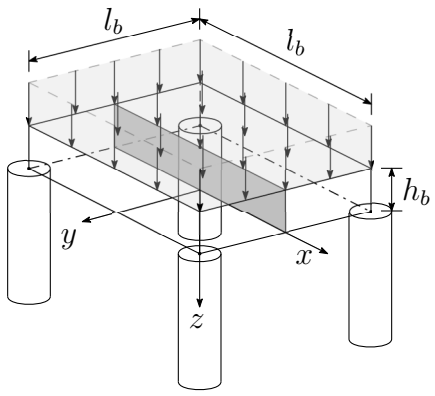

Figure 4.26: Central plane of a structure submitted to a vertical load

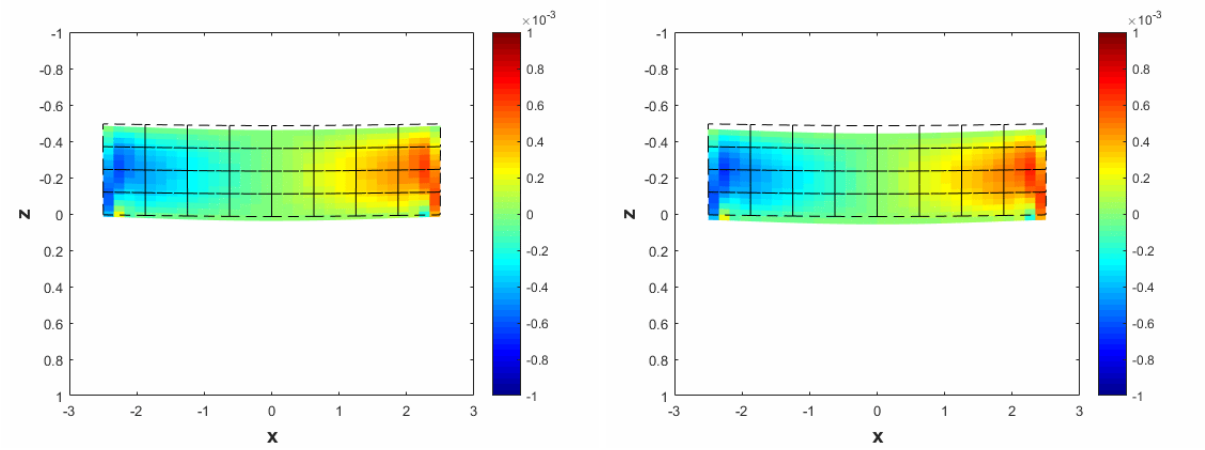

Figure 4.27: Shear strain at the central face due to a vertical load for nondimensional frequency $a_0 = 0.5$ and $a_0 = 1.0$

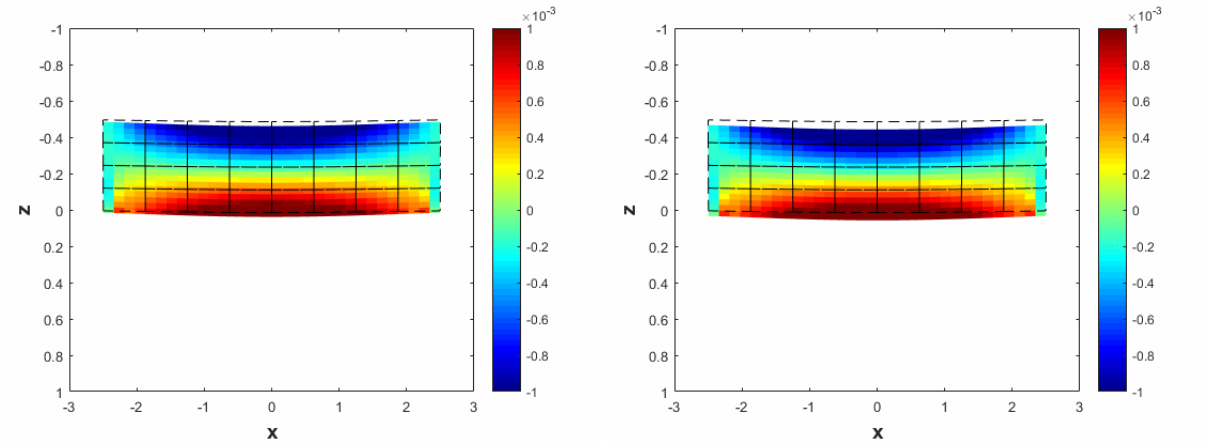

Figure 4.28: Volumetric strain at the central face due to a vertical load for nondimensional frequency $a_0 = 0.5$ and $a_0 = 1.0$

In these figures, the deformations at the central face of the piled structure (Fig. 4.26) and of the supported structure (Fig. 4.29) are also highlighted.

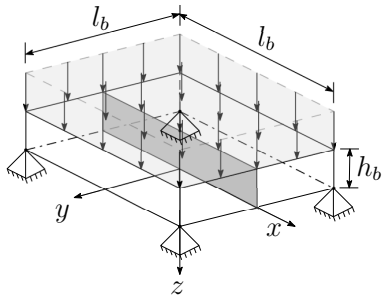

Figure 4.29: Central plane of a supported structure submitted to a vertical load

4.6.2 Strain field due to horizontal loads

For the pile groups shown in Figures 4.30 and 4.34, the features of the system are the same of previous analysis, except that the elastic modulus relation is $E_{st}/E_p = 0.178$. A distributed horizontal load is applied at the superior face of this structure.

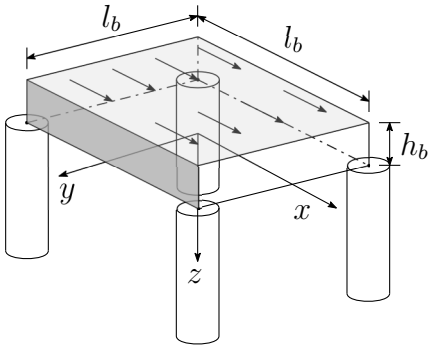

Figure 4.30: Frontal plane of a structure submitted by a horizontal load

Again, the deformation of the frontal face of such system is compared with the one of a supported structure (Fig. 4.31)

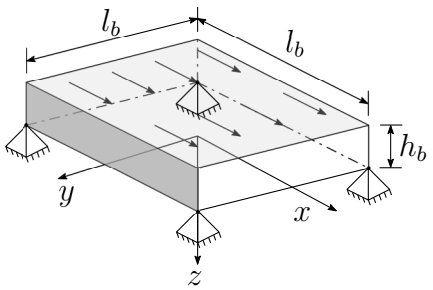

Figure 4.31: Frontal plane of a supported structure submitted by a horizontal load

Figures 4.32 and 4.33 show the harmonic deformation of the structure. In Fig. 4.32, the color map represents the shear strain field over time and in Fig. 4.33, one represents volumetric strains at the frontal face of the piled structure (Fig. 4.30).

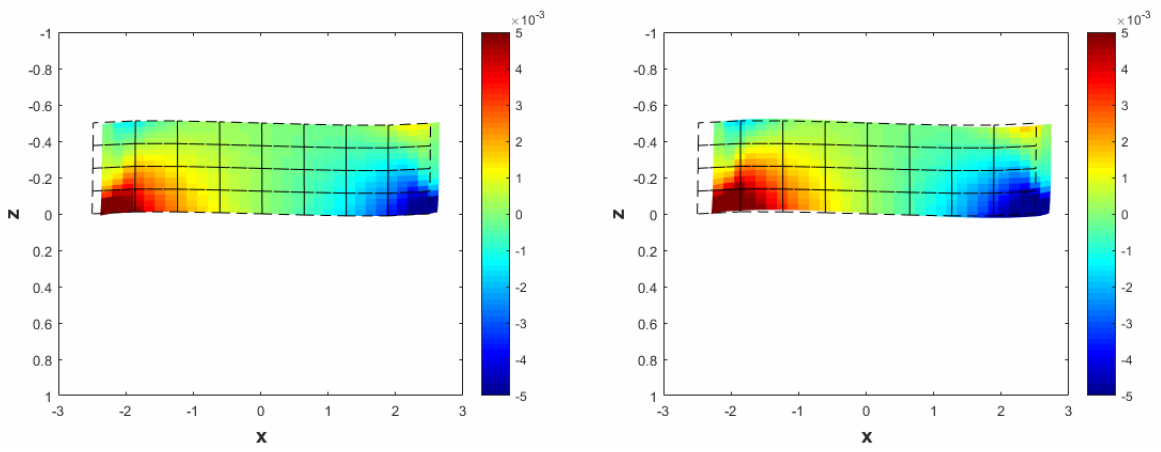

Figure 4.32: Shear strain at the frontal face due to a horizontal load for nondimensional frequency $a_0 = 0.5$ and $a_0 = 1.0$

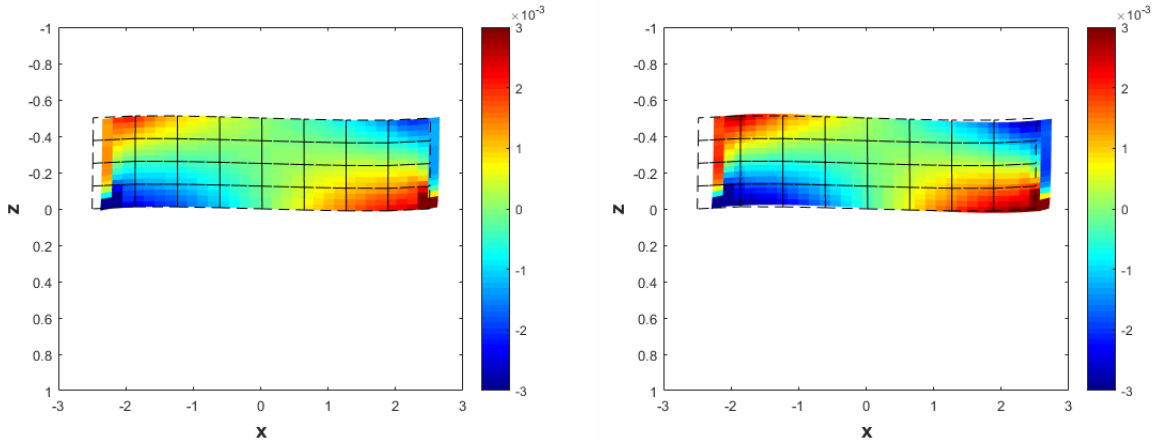

Figure 4.33: Volumetric strain at the frontal face due to a horizontal load for nondimensional frequency $a_0 = 0.5$ and $a_0 = 1.0$

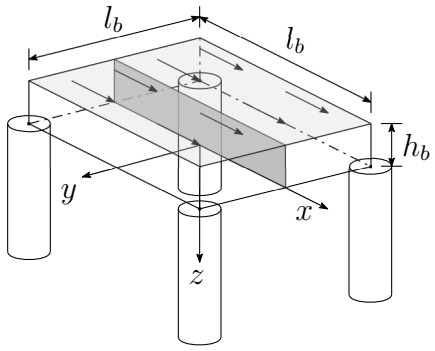

Figure 4.34: Central plane of a structure submitted by a horizontal load

For the central face, as shown in Figure 4.34, Fig. 4.35 and 4.36 present the color map of the shear and volumetric strains field, respectively.

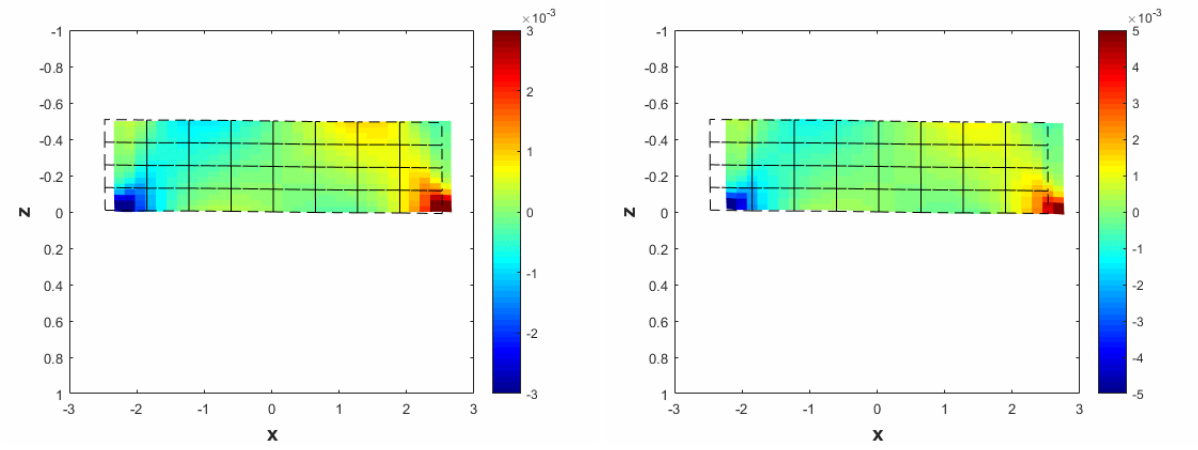

Figure 4.35: Shear strain at the central face due to a horizontal load for nondimensional frequency $a_0 = 0.5$ and $a_0 = 1.0$

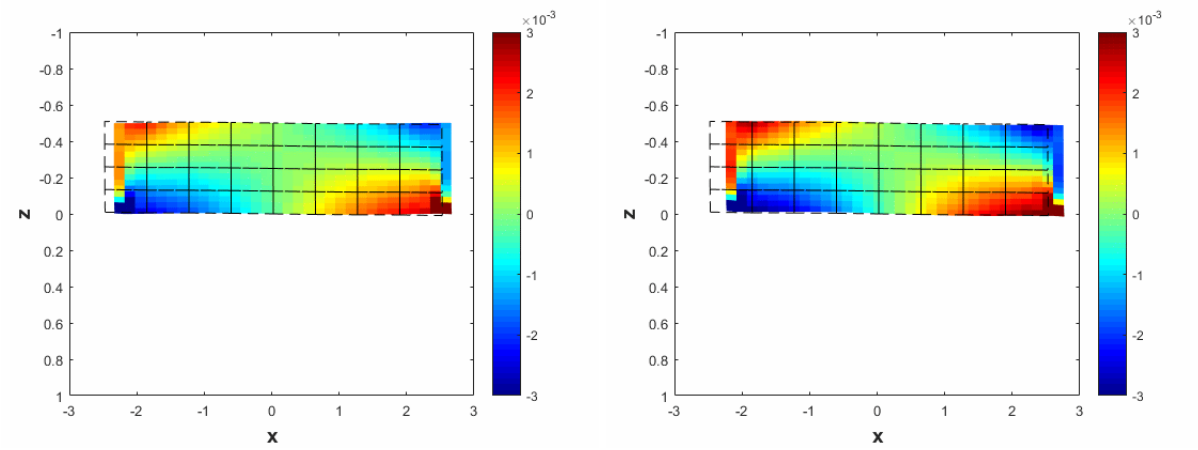

Figure 4.36: Volumetric strain at the central face due to a horizontal load for nondimensional frequency $a_0 = 0.5$ and $a_0 = 1.0$

In these figures, the deformations at the central face of the piled structure (Fig. 4.34) and of the supported structure (Fig. 4.37) are also highlighted.

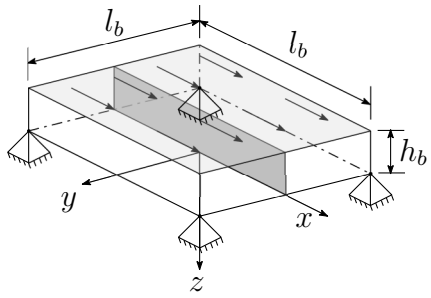

Figure 4.37: Central plane of a supported structure submitted by a horizontal load

5 Conclusions

This dissertation proposed a coupling scheme between a pile group and a flexible structure. For the representation of the pile group, a generalized and modern implementation of the impedance matrix model was presented. This implementation is capable of dealing with as many piles as the physical computing capacity of the computer hardware, which can be easily extended for large CPU clusters. In addition to arbitrary number of piles, the proposed implementation is capable of considering an arbitrary number of soil layers, which enables Gibson's soils and weathered crusts to be modeled. An arbitrary number of excitation frequencies can be considered as well, with which one may obtain accurate impulse responses of the embedded pile group directly through Fourier transforms of the frequency response of the model. The flexible structure was modeled by an 8-noded linear elastic finite element.The discretization of such structure is done in such a way that there is a node at the pile heads location. The coupling is obtained by kinematic compatibility and equilibrium equations at the nodes shared by both systems. In order to verify the physical consistency of the coupling scheme, two analyses are proposed: a validation of such scheme by increasing the stiffness of the structure and comparing with the literature results, and a strain-deformation field investigation. Both analyses showed that the present scheme is able to represent well the dynamic pile-soil-structure interaction. This scheme encompasses arbitrarily shaped structures, which allows a wide applicability in several branches of Engineering.

References

Adolph, M., Mesquita, E., and Romanini, E. (2001). A methodology to determine the transient response of the structures interacting with visco-elastic soils using the FFT algorithm. In *Proceedings of XXI Iberian-Latin-American Congress on Computational Methods in Engineering*, volume 1, pages 1–23.

Apsel, R. J. and Luco, J. E. (1976). Torsional response of rigid embedded foundation. *Journal of the Engineering Mechanics Division*, 102(6):957–970.

Arnold, R., Bycroft, G., and Warburton, G. B. (1955). Forced vibrations of a body on an infinite elastic solid. *ASME J. Appl. Mech*, 77:391–401.

Awojobi, A. and Grootenhuis, P. (1965). Vibration of rigid bodies on semi-infinite elastic media. *Proceedings of the Royal Society of London. Series A. Mathematical and Physical Sciences*, 287(1408):27–63.

Banerjee, P. K. (1978). Analysis of axially and laterally loaded pile groups. *Developments in Soil Mechanics*, 1:317–246.

Barros, P. L. A. (2006). Impedances of rigid cylindrical foundations embedded in transversely isotropic soils. *International Journal for Numerical and Analytical Methods in Geomechanics*, 30(7):683–702.

Barros, P. L. A., Labaki, J., and Mesquita, E. (2018). IBEM-FEM model of a piled plate within a transversely isotropic half-space. *Engineering Analysis with Boundary Elements*.

Butterfiel, R. and Banerjee, P. K. (1971). The elastic analysis of compressible piles and pile groups.

Géotechnique, 21(1):43–60.

Bycroft, G. N. (1956). Forced vibrations of a rigid circular plate on a semi-infinite elastic space and on an elastic stratum. *Philosophical Transactions of the Royal Society of London. Series A, Mathematical and Physical Sciences*, 248(948):327–368.

Cavalcante, I., Vasconcelos, A. C. A., and Labaki, J. (2017). A continuation algorithm-Longman's method scheme for the integration of transcendental functions. In *Proceedings of the Iberian Latin American Congress on Computational Methods in Engineering*.

Chadwick, P. and Trowbridge, E. A. (1967a). Oscillations of a rigid sphere embedded in an infinite elastic solid: I. torsional oscillations. In *Mathematical Proceedings of the Cambridge Philosophical Society*, volume 63, pages 1189–1205. Cambridge University Press.

Chadwick, P. and Trowbridge, E. A. (1967b). Oscillations of a rigid sphere embedded in an infinite elastic solid: II. rectilinear oscillations. In *Mathematical Proceedings of the Cambridge Philosophical Society*, volume 63, pages 1207–1227. Cambridge University Press.

Christensen, R. (2012). *Theory of viscoelasticity: an introduction*. Elsevier.

Cook, R. D. (2007). *Concepts and applications of finite element analysis*. John Wiley & Sons.

Desai, C. S. and Kuppusamy, T. (1980). Application of a numerical procedure for laterally loaded structures. In *Numerical methods in offshore piling*, pages 93–99. Thomas Telford Publishing.

Gladwell, G. M. L. (1968). Forced tangential and rotatory vibration of a rigid circular disc on a semi-infinite solid. *International Journal of Engineering Science*, 6(10):591–607.

Jin, J. M. (2014). Solutions for axisymmetric problems of layered generalized gibson subgrade. *Applied Mechanics and Materials*, 574:53–57.

Kausel, E. (2006). *Fundamental solutions in elastodynamics: a compendium*. Cambridge University Press.

Kausel, E. (2017). *Advanced structural dynamics*. Cambridge University Press.

Kausel, E. (2018). Generalized stiffness matrix method for layered soils. *Soil Dynamics and Earthquake Engineering*, 115:663–672.

Kausel, E. and Peek, R. (1982). Dynamic loads in the interior of a layered stratum: an explicit solution. *Bulletin of the Seismological Society of America*, 72(5):1459–1481.

Kausel, E. and Roësset, J. M. (1981). Stiffness matrices for layered soils. *Bulletin of the Seismological Society of America*, 71(6):1743–1761.

Kaynia, A. M. (1982). *Dynamic stiffness and seismic response of pile groups*. PhD thesis, Massachusetts Institute of technology.

Kaynia, A. M. and Kausel, E. (1991). Dynamic of piles and pile groups in layered soil media. *Soil Dynamics and Earthquake Engineering*, 10(8):386–401.

Kobori, T. and Thompson, W. (1963). Dynamical compliance of rectangular foundations on an elastic half-space. *Journal of Applied Mechanics, Transactions of the American Society of Mechanical Engineers*, 30:579–584.

Labaki, J., Damasceno, D. A., and Mesquita, E. (2013). Transient response of rigid foundations embedded in transversely isotropic media through an intertive dynamic coupling scheme. In *International Conference on Computational & Experimental Engineering and Sciences*.

Labaki, J., Ferreira, L. O. S., and Mesquita, E. (2011). Constant boundary elements on graphics hardware: a gpucpu complementary implementation. *Journal of the Brazilian Society of Mechanical Sciences and Engineering*, 33:475–482.

Labaki, J., Mesquita, E., and Rajapakse, R. K. N. D. (2014). Vertical vibrations of an elastic foundation with arbitrary embedment within a transversely isotropic, layered soil. *Computer Modeling in Engineering & Sciences*, 103(5):281–313.

Labaki, J., Rajapakse, R. K. N. D., and Mesquita, E. (2018). Dynamic response of a rigid circular foundation in layered anisotropic and gibson's soils. *Géotechnique*.

Lysmer, J. (1970). Lumped mass method for rayleigh waves. *Bulletin of the Seismological Society of America*, 60(1):89–104.

Lysmer, J. and Waas, G. (1972). Shear waves in plane infinite structures. *Journal of Engineering Mechanics*.

Matlock, H. (1970). Correlations for design of laterally loaded piles in soft clay. *Offshore technology in civil engineering's hall of fame papers from the early years*, pages 77–94.

Muki, R. (1960). Asymmetric problems of the theory of elasticity for a semi infinite solid and a thick plate. *Progress in solid mechanics*, pages 399–439.

Nogami, T. and Novák, M. (1976). Soil-pile interaction in vertical vibration. *Earthquake Engineering & Structural Dynamics*, 4(3):277–293.

Novak, M. (1974). Dynamic stiffness and damping of piles. *Canadian Geotechnical Journal*, 11(4):574–598.

Penzien, J. (1970). Soil-pile foundation interaction. *Earthquake engineering*, 11.

Piessens, R., de Doncker-Kapenga, E., Überhuber, C. W., and Kahaner, D. K. (2012). *Quadpack: a subroutine package for automatic integration*. Springer Science & Business Media.

Poulos, H. G. (1971). Behavior of laterally-loaded piles: II - pile groups. *Journal of the Soil*

Mechanics and Foundation Division, 97(SM5):733–751.

Poulos, H. G. and Aust, A. (1968). Analysis of the settlement of pile groups. *Géotechnique*, 18(4):449–471.

Poulos, H. G. and Mattes, N. S. (1971). Settlement and load distribution analysis of pile groups. *Australian Geomechanics Journal*, 1(1).

Prakash, S. and Chandrasekaran, V. (1973). Pile foundation under lateral dynamic loads. In *International Journal of Rock Mechanics and Mining Sciences & Geomechanics Abstracts*. Pergamon.

Quinlan, P. (1954). The elastic theory of soil dynamics. In *Symposium on Dynamic Testing of Soils*. ASTM International.

Reissner, E. (1936). Stationäre, axialsymmetrische, durch eine schüttelnde masse erregte schwingungen eines homogenen elastischen halbraumes. *Archive of Applied Mechanics*, 7(6):381–396.

Reissner, E. and Sagoci, H. (1944). Forced torsional oscillations of an elastic half-space. i. *Journal of Applied Physics*, 15(9):652–654.

Schenk, O. and Gartner, K. (2004). Solving unsymmetric sparse systems of linear equations with pardiso. *Future Generation Computer Systems*, 20(3):475–487.

Sen, R., Kausel, E., and Banerjee, P. K. (1985). Dynamic analysis of piles and pile groups embedded in non-homogeneous soils. *International Journal for Numerical and Analytical Methods in Geomechanic*, 9(6):507–524.

Sommerfeld, A. (1949). *Partial differential equations*. Academic Press.

Sung, T. (1954). Vibrations in semi-infinite solids due to periodic surface loading. In *Symposium on dynamic testing of soils*. ASTM International.

Vasconcelos, A. C. A., Cavalcante, I., and Labaki, J. (2017). On the accuracy of adaptive quadratures in the numerical integration of singular Green's functions for layered media. In *Proceedings of the Iberian Latin American Congress on Computational Methods in Engineering*.

Waas, G. and Hartmann, H. G. (1981). Impedance function of a group of vertical piles. In *Structural mechanics in reactor technology*, volume K.

Warburton, G. (1957). Forced vibration of a body on an elastic stratum. *ASME J. Appl. Mech*, 79:55–57.

Wolf, J. P. and von Arx, G. A. (1978). Impedance function of a group of vertical piles. In *Proceedings of the Specialty Conference on Soil Dynamics and Earthquake Engineering*, volume 2, pages 1024–1041. ASCE.